UNIVERSITY OF SOUTHAMPTON

FACULTY OF ENGINEERING, SCIENCE &
MATHEMATICS

SCHOOL OF PHYSICS AND ASTRONOMY

Semiconductor Seeded Fibre Amplified Sources of Ultra Short Pulses

Stephen Paul Elsmere

Submitted for the degree of Doctor of Philosophy

May 2009

UNIVERSITY OF SOUTHAMPTON

ABSTRACT

FACULTY OF ENGINEERING, SCIENCE & MATHEMATICS
SCHOOL OF PHYSICS AND ASTRONOMY

Doctor of Philosophy

Semiconductor Seeded Fibre Amplified Sources of Ultra Short Pulses

By Stephen Paul Elsmere

This thesis reports upon an experimental investigation of passively mode-locked optically pumped vertical-external-cavity surface-emitting semiconductor lasers (VECSEL). Mode-locked VECSELs are a compact source of ultra-short pulses at GHz repetition rates, with pulse lengths as short as 190 fs being generated directly from the laser. The VECSEL is a power scalable device offering spectral versatility through band gap engineering of semiconductor gain material.

Here, for the first time the technique of frequency resolved optical gating (FROG) has been used to record a second harmonic spectrogram of the VECSEL pulse train, from which the phase information of non-transform limited sub-picosecond pulses has been retrieved. I also report the characterisation of a single stage VECSEL seeded ytterbium-doped fibre amplifier, capable of increasing the average power of a VECSEL from 20 mW to over 1.5 W while maintaining the sub-picosecond duration of the pulse train. The amplifier is capable of operating at any repetition rate obtainable with a VECSEL, amplification is demonstrated here with 1 GHz and 6 GHz seeds.

Finally, the nonlinear evolution of VECSEL pulses inside a single stage fibre amplifier has been investigated. Computer modelling of the linear gain and nonlinear pulse propagation within a single fibre has been used to design an amplifier capable of producing pulses with a parabolic profile. The modelling reveals that a parabolic amplifier would produce spectrally broader linearly chirped pulses which could be compressed to below 100 fs, with average powers > 3 W. An experimental realisation of the parabolic amplifier will require a seed with average power greater than 100 mW, this could be achieved with a re-growth of an existing sample, QT1544.

List of Tables

2.1 Density of semiconductor states per unit volume for four different dimensionalities of semiconductor: quantum dot (0D), quantum wire (1D), quantum well (2D) and bulk. 26

3.1 Properties of the 1 and 6 GHz VECSELs relevant to a discussion of phase structure in the laser pulse train.*Peak power assumes a 60 μm spot upon the gain.**Peak power assumes a 10 μm spot upon the SESAM. 70

3.2 Comparison of the phase properties of a VECSEL gain chip operating at two different repetition rates. 78

List of Figures

1.1 (a) An examle of a VECSEL cavity and, (b) a generic gain structure. The cavity is 1 GHz z-cavity including a semiconductor saturable absorber mirror (SESAM) for passive mode-locking of a VECSEL 3

1.2 Configuration of the two stage VECSEL MOPA used in [49]: $(PM) - YDF$ (polarisation maintaing) ytterbium doped fibre, LD laser diode, $\lambda/2$ half wave plate, ps picosecond pulse pre compression, fs femtosecond pulse obtained after compression in a grating compressor. . . 10

2.1 Set up of a 1 GHz passively mode-locked VECSEL. An 830 nm fibre-coupled diode, delivering up to 1.3 W is used for pumping the gain chip. A pair of lenses (not shown) are used to form a 2:1 image of the output from the fibre, giving a 60 μm radius spot upon the gain chip. The properties of the external cavity will be discussed later in section 2.2.1. The inset layer structures are for the gain (QT1544) and the SESAM (QT1627) used in this thesis. 19

2.2 Bandgap energy and lattice constant for several III-V semiconductor materials at room temperature, taken from [2]. 20

2.3 a) Band structure of bulk GaAs, taken from [2]; b) parabolic band structure showing four time regimes for the decay of excited electrons from the conduction band into the valence band, taken from [4] 22

2.4 Distributed Bragg reflector structure enables constructive interference of the partial reflections from each quarter λ layer resulting in > 99 % reflectivity. Here λ is the wavelength of light within the material. . . . 24

2.5 Calculated reflectivity for the gain sample QT1627 used in this thesis (excluding absorption effects). 24

2.6 a) Diagram of a strain compensated quantum well showing material bandgap energy and the quantum well emission. b) The density of states for a quantum well, blue(step) and for bulk (red curve). SC = strain compensation layer, CB = conduction band, VB = valence band, and E_{gm} (E_{QW}) is the bandgap of the bulk (quantum well) material. . . 28
2.7 Top: active region of QT1544 showing the position of the six quantum wells along with the intensity distribution at the design wavelength. Bottom: Percentage of absorbed pump light available to create carriers at each quantum well. Taken from [2]. 29
2.8 (a) Calculated intensity distribution $|E|^2$ at the resonant design wavelength λ, within a resonant gain structure with overall thickness $9\lambda/2$, assuming an incoming wave amplitude of 1. (b) Reflectivity (top) and longitudinal confinement factor (bottom) as a function of wavelength for the resonant cavity. Taken from [6]. 31
2.9 (a) Calculated intensity distribution $|E|^2$ at the anti-resonant design wavelength λ, within an anti-resonant gain structure with overall thickness $19\lambda/4$, assuming an incoming wave amplitude of 1. (b) Reflectivity (top) and longitudinal confinement factor (bottom) as a function of wavelength for the resonant cavity.Taken from [6]. 32
2.10 Three regimes of passive modelocking: (a) fast saturable absorber opens a short window of net gain, (b) slow saturable absorber opens a long window of net gain, (c) slow saturable absorber combined with dynamic gain saturation opens a short time window of net gain. Taken from [4] 35
2.11 Calculated group delay dispersion (measured in $fs^(2)$) and electric field strength upon the quantum well (bottom) for the SESAM used in this thesis. The shaded regions are to indicate the wavelength range over which the VECSEL operates. 36
2.12 Stability curves for the 1 GHz z-cavity: (a) cavity mode at the surface of the gain chip, as a function of the separation D between the SESAM and 25 mm high reflector; (b) cavity waist upon SESAM as a function of D. The shaded areas correspond to the approximate stable operating range of the cavity. 38

2.13 Experimental arrangement used to perform the optical characterisation of QT1544, taken from [6].M, mirror; L, lens; D, doublet lens; MO, microscope objective; LP, long pass filter; PD, InGaAs photodiode; FT, flip-top component. 39
2.14 (a) Edge photoluminescence (PL) from QT1544, (b) top PL recorded at 3 different temperatures and pump powers as indicated in the figures. Taken from [6]. 41
2.15 Measured reflectivity spectrum recorded for gain wafer QT1544 (solid line); reflectivy spectrum obtained for QT1544 design, using a multilayer calculation (dotted line) taken from [6]. The multilayer calculation fails to acurately model the modulations in the measured spectrum. This can be attributed to the inacurate, specification of refractive index away from the design wavelength of the DBR. 43
2.16 a) CW spectra recorded at various temperatures, b) mode-locked spectra recorded at the temperatures recorded in the figuree, c) power transfer curve recorded for a CW VECSEL. 44

3.1 (a) Temporal profile of a chirped and un-chirped 50 fs pulse,(b) Fourier transform of the 50 fs chirped pulses in (a). 50
3.2 Block diagram of an experimental FROG measurement. 51
3.3 Experimental FROG configuration; output from the VECSEL characterized before and after FROG measurements by taking SHG autocorrelation and spectrum. Partial reflections from a glass wedge enabled the optical spectrum and RF spectrum (or fast scope trace) to be observed during a FROG measurement. FT = flip top mirror, L1 = 10 cm focal length lens; a 300 m thick BBO crystal cut for non-collinear SHG with a 15 degree full angle between incident beams was used to produce the FROG signal. 53
3.4 Experimentally recorded FROG traces of (a) 1 GHz VECSEL emitting a train of double pulses with average power 12.4 mW; (b) the same laser switching between different numbers of multiple pulses and CW operation, average power 19.55 mW. Number of steps were 512, step size was 13 fs, integration time was 80 ms. 59

3.5 Delay and frequency marginals (blue curves) overlapped with experimentally measured autocorrelations and spectral convolutions (red curves). Marginlas are calculated for data from figure 3.4, (a) stable double pulse, (b) switching between multiple pulsing and cw-operation. 61

3.6 Experimental FROG trace (a) and the corresponding trace retrieved by the FROG algorithm (b). The VECSEL emitted a train of double pulses with an average power of 13 mW, pulse length = 590 fs ($sech^2$) and the bandwidth was 3.27 nm centered at 1046.9 nm measured before recording the FROG trace; the average power changed to 11.8 mW, pulse length 570 fs ($sech^2$) and the bandwidth was 3.16 nm centered at 1046.9 nm all measured after recording the FROG trace. The calculated FROG error was 0.0073. Number of steps = 512, step size = 12 fs, integration time = 120 ms. 62

3.7 Retrieved spectrum (a) and square modulus of the E-field (b) corresponding to the 1 GHz VECSEL data of figure 3.6. The data has been normalized and is plotted along with the autocorrelation multiplied by 0.648 ($sech^2$) and measured spectrum. The modulations in the measured spectrum are caused by reflections from the substrate of the VECSEL chip and do not appear in the FROG data as the temporal sampling range was to low; the side pulses in the measured autocorrelation are caused by the same effect and are also absent from the retrieved data. 64

3.8 Instantaneous frequency and group delay retrieved by the algorithm for the 1 GHz VECSEL, data in figure 3.7. The instantaneous frequency (a) is plotted along with the square modulus of the retrieved E-field (blue curve), while the group delay (b) is plotted along with the retrieved spectrum (blue curve). A log plot of the spectrum is included showing artificial spikes in the group delay when the intensity of the spectrum reaches a minimum. The phase information in these plots only has a real meaning where it corresponds to a non-zero value of the spectrum/square modulus of the E-field. 65

3.9 Polynomial fit (red curves) to chirp and group delay (black curves) of data from figure 3.8; note that the phase information in the plots only has real meaning for non-zero values of the spectrum/square modulus of the E-field (green curves). The fitting parameters for these curves are given at the bottom of the plots. 67
3.10 Fast scope trace of the stable 1 GHz VECSEL, showing a train of double pulses. Individual pulses are separated by aproximately 160 ps. 69
3.11 Experimental FROG trace (a) and the trace retrieved by the algorithm (b). The laser was a 6 GHz VECSEL emitting a train of single pulses. The train had a centre wavelength of 1049.8 nm with a 2.45 nm bandwidth and average power of 14.6 mW measured before FROG; the pulse length was 730 fs assuming a sech^2 fit. After the FROG trace was recorded the average power remained at 14.6 mW, the bandwidth had slightly narrowed to 2.37 nm centered at 1049.8 nm while the pulse length had increased to 740 fs. The FROG error was 0.0051. 71
3.12 Normalized frequency (a) and delay marginals (b) of the experimental FROG trace of figure 3.11 (blue curves); plotted on the same axis are the experimentally measured autocorrelation and spectrum (red curves). 72
3.13 Retrieved spectrum (a) and square modulus of the E-field (b) (blue curves) plotted along with the measured autocorrelation multiplied by 0.648 (sech^2 fit) and spectrum. All the curves have been normalized. There is evidence of substrate reflections in both the measured spectrum and autocorrelation that has not been picked up by the FROG measurement. 74
3.14 Instantaneous frequency and square modulus of the retrieved E-field (a). Group delay and retrieved spectrum are plotted along with a log plot of the retrieved spectrum (b). There are two artificial spikes in the group delay corresponding to local minimum in the retrieved spectrum. 75
3.15 Parabolic fit (red curves) to chirp and group delay (black curves) of data from figure 3.14; the phase information in the plots only has real meaning for non zero values of the spectrum/square modulus of the E-field (green curves). The fit parameters for these curves are given at the bottom of the plots. 77

4.1 Side view of a double clad Yb-doped fibre. Two examples (right) of how the symmetry of the core/inner cladding may be broken to ensure maximum overlap of the cladding modes with the fibre core. 84
4.2 Absorption (solid) and emission (dotted) cross sections of Yb in germanosilicate glass a), taken from [5]. Energy level diagram showing the $^2F_{7/2}$ and $^2F_{5/2}$ manifolds along with the stark levels b). 86
4.3 Transparancy pump power versus signal wavelength for a number of pump wavelengths taken from [5]; the data was calculated for a single clad fibre. 87
4.4 SPM-broadend spectra for an unchirped Gaussian pulse taken fron [7]. Spectra are labeled, showing the maximum nonlinear phase shift ϕ_{max}. 95

5.1 A 6 GHz v-cavity. OC: 25 mm radius of curvature output coupler; X: is a variable separation between SESAM and gain chip. 103
5.2 Stability curves for the 6 GHz cavity. (a) Cavity mode upon the gain for a fixed cavity length 24.99 mm as a function of X, (b) cavity waist upon SESAM as a function of the total cavity length. 105
5.3 Arrangement of the fibre amplifier. DM: dichroic mirror, rflects at 915 nm and transmitting around 1040 nm; L1 and L3: focal length 4.5 mm lenses with 0.45 NA; L2: focal length 8 mm lens with 0.5 NA; LD: 5.5 W laser diode for pumping of the fibre at 915 nm. 106
5.4 Liekki modelling results of a 2.2 m long fibre amplifier with cw seed at 1042 nm. (a) constant pump of 4 W, (b) variable pump for three fixed seed powers of 0.2, 1 and 3 mW. All powers are those coupled into the fibre (not the incident power). 108
5.5 Laser spectra for 2.3 m of large core Yb-doped fibre for two different pump powers: 1.81 W (black curve) fibre lasing just above threshold, centre wavelength is 1037.5 nm; 1.76 W (red curve) showing only the ASE as the fibre is just below the laser threshold. 109

5.6 Amplifier results with a 1 GHz VECSEL seed: (a) seed spectrum; (b) autocorrelation of VECSEL seed including a sech^2 fit; (c) amplified spectrum; (d) autocorrelation of amplified pulse train; (e) log plot of amplified spectrum showing residual ASE. The modulations present in both the amplified and seed spectra are due to substrate reflections within the VECSEL. 111

5.7 Amplifier results with a 6 GHz VECSEL seed: (a) seed spectrum; (b) autocorrelation of VECSEL seed including a sech^2 fit; (c) amplified spectrum; (d) autocorrelation of amplified pulse train; (e) log plot of amplified spectrum showing residual ASE. The modulations present in both the amplified and seed spectra are due to substrate reflections within the VECSEL. 114

6.1 Modelling results for Liekki fibre with a 20 mW seed propagating in the same direction as a 920 nm pump: (a) gain in dBm for various incident pump powers, (b) fibre inversion percentage, (c) amplified signal strength (1040 nm) and residual pump vs fibre length; arrow indicates 10 W pump result. The data indicates that the peak gain occurs within the first 2 m of the fibre and that for pump powers that are < 5 W some reabsorption of the signal takes place in the final 3 m of the fibre. 124

6.2 Modelling results for a 20 mW seed propagating in the same direction as a 975 nm pump: (a) gain in dBm for various incident pump powers, (b) fibre inversion percentage, (c) amplified signal strength (1040 nm) and residual pump as a function of fibre length; result with 10 W pump is indicated by an arrow. Data shows a higher total gain and that the peak signal power is reached after a shorter length of fibre than when pumped by a 920 nm source. Some reabsorption still occurs in the last 3 m of fibre when pumped below 5 W. 125

6.3 Modelling results for Liekki fibre with a 20 mW seed propagating counter to a 920 nm pump: (a) gain in dBm for various incident pump powers, (b) fibre inversion percentage, (c) amplified signal strength (1040 nm) and residual pump as a function of fibre length with arrow indicating 10 W pumping. The accuracy of this modelling is reduced due to the increased complexity of modelling a counter propagating pump. The location of peak inversion and gain within the fibre is more dependent upon pump power with this scheme. The signal experiences initial loss, taking longer to reach maximum power than in the equivalent forward pumping schemes, making this pump configuration less useful for parabolic amplification. 126
6.4 Nonlinear propagation in the time and frequency domains of a 500 fs Gaussian seed pulse with repetition rate 1 GHz and average power of 20 mW. (a) Assumes a linear gain, (b) assumes a fit to the modelled output power as a function of length in figure 6.1 (c); with a 10 W 920 nm pump. 129
6.5 Colinear pump set up for the parabolic amplifier: a fiberised pump combiner is used to couple the seed/pump into the core/cladding of a 6 μm core Yb-doped fibre (Liekki1200-6Yb/125DC): DM is a dichroic mirror, L is a lens. 130
6.6 Spectra taken from the output end of the amplifier configuration of figure 6.5. The spectra were recorded with three different pump powers as indicated in the figure; in each case there was a 20 mW seed incident upon the amplifier. Lasing close to 1084 nm dominates the fibre output despite the pressence of seed pulses near 1040 nm. 132

UNIVERSITY OF SOUTHAMPTON

I, Stephen Paul Elsmere, declare that the thesis entitled 'Semiconductor Seeded Fibre Amplified Sources of Ultra Short Pulses' and the work presented in it are my own. I confirm that:

- this work was done wholly or mainly while in candidature for a research degree at this University;
- where any part of this thesis has previously been submitted for a degree or any other qualification at this University or any other institution, this has been clearly stated;
- where I have consulted the published work of others, this is always clearly attributed;
- where I have quoted from the work of others, the source is always given. With the exception of such quotations, this thesis is entirely my own work;
- I have acknowledged all main sources of help;
- where the thesis is based on work done by myself jointly with others, I have made clear exactly what was done by others and what I have contributed myself;
- parts of this work have been published as listed on the following page.

Signed:

Date: 25/5/2009

Acknowledgements

First and foremost, I would like to thank my supervisor Prof. Anne Tropper for introducing me to this field of research, for her continuous support and advice.

I would like to say a warm thank you to Dr. Kieth Wilcox for his endless enthusiasm and continuous inspiration "if it wasn't difficult everyone would be doing it". I thank Dr. Hanna Foreman and Dr. Pascal Dupriez for your tutorage during the early stages of this project. I would like to thank Dr. Jonathan Price and Dr. Fei He for many fruitful discussions and their help with fibre modelling. I also thank Dr. Jerry Prawiharjo for his help and advice with the FROG algorithm.

I am most grateful to the members of the VECSEL group, both past and present whom I have had the pleasure of working with. I would especially like to thank Zakaria Mihoubi and Adrian Quarterman for their continuous support during this project.

I would like to thank the members of the Quantum, Light & Matter group for sharing their research and ideas for my own work with me. I also thank the support staff and workshop people for all their help.

Finally I would like to thank my friends and family for their continuous support and love, without which none of this would have been possible. I am especially grateful to Danielle for putting up with me during this work: thank you so much.

To Danni

Chapter 1

Introduction

The vertical external cavity surface emitting laser (VECSEL) also known as the surface emitting semiconductor laser or semiconductor disc laser, is a power scalable device, offering spectral versatility through bandgap engineering of a semiconductor gain, while capable of delivering Watt level powers in a nearly diffraction limited TEM_{00} output beam. Optically pumped VECSELs act as brightness converters, changing the high power, poor beam quality of an edge emitting diode laser into a high power high quality output beam. The external cavity not only controls the quality of the output beam, but allows for added functionalities of the laser by inserting extra elements such as frequency doubling crystals into the cavity. Because of these added functionalities and the spectral versatility of semiconductors, the VECSEL is an alternative source to many solid state lasers as well as other semiconductor lasers.

VECSELs with tens of Watts output power have been demonstrated at wavelengths near 1 μm; such high power high brightness sources can be used in preference to edge emitting diodes, for material processing or optical pumping of other lasers, when a tightly foccussed TEM_{00} beam is required. Band gap engineering of the semiconductor gain enables VECSELs to operate over a wide range of wavelengths with potentially very high bandwidths, for example, a tuning range of 150 nm has been demonstrated near 2 μm [1]. The external cavity of the VECSEL increases the functionality of the device. By inserting additional elements into the cavity applications such as intracavity frequency doubling, passive mode locking and intracavity spectroscopy become possible.

The concept of the VECSEL was first demonstrated in 1997 [2] by Kuznetsov et al. The VECSEL architecture combines the desirable properties of two other semicon-

ductor lasers: the high power of an edge emitting diode with the high beam quality of a vertical cavity surface emitting laser (VCSEL); achieving multi Watt continuous-wave (CW) operation with a high beam quality. The laser demonstrated by Kuznetsov incorporated an optically pumped half VCSEL inside of an external cavity. The external cavity enforces a high beam quality characterized by a low M^2 TEM_{00} output beam. A larger mode area within the half VCSEL can be pumped optically than in the electrically pumped VCSEL, this enables for high output powers.

1.1 Vertical External Cavity Surface Emitting Lasers

An example of an optically pumped VECSEL cavity can be seen in figure 1.1 along with a generic gain structure. The gain structure is grown epitaxially upon a semiconductor substrate. There are two possible growth directions; a top up growth requires that the highly reflective distributed Bragg reflector (DBR) be grown first on top of the substrate. The active region is then grown on top of the DBR followed by a window layer and finally a capping layer. A micro cavity is formed between the air interface and the DBR resulting in a standing wave of the laser field within the gain chip. To ensure optimum gain, the thickness of the spacer layers, within the gain region, are chosen so that each quantum well is positioned upon a node of the microcavity standing wave. The window layer thickness is usually chosen so that the total micro cavity length is either resonant with the laser wavelength $(n\lambda/2)$ or anti resonant $\left(\left(n+\frac{1}{2}\right)\lambda/2\right)$ where n is an integer.

The capping layer can simply be a sliver of material to prevent oxidation of the underlying semiconductor materials, or as more often the case an antireflection coating. In the case of the top down growth the capping layer will be grown upon the substrate first, then followed by the other layers in reverse order so that the DBR is exposed to the air. Top down growth is performed when it is desired to remove the substrate of the gain chip post growth, this can be done by chemical etching in which case the capping layer will also incorporate an etch stop layer. The structural features and principals of operation of the VECSEL are discussed in more detail in the review articles by Tropper et al. [3].

The VECSEL enables high output powers with high beam quality, the device is power scalable and can be pumped by a variety of differnt schemes. The incorpo-

(a)

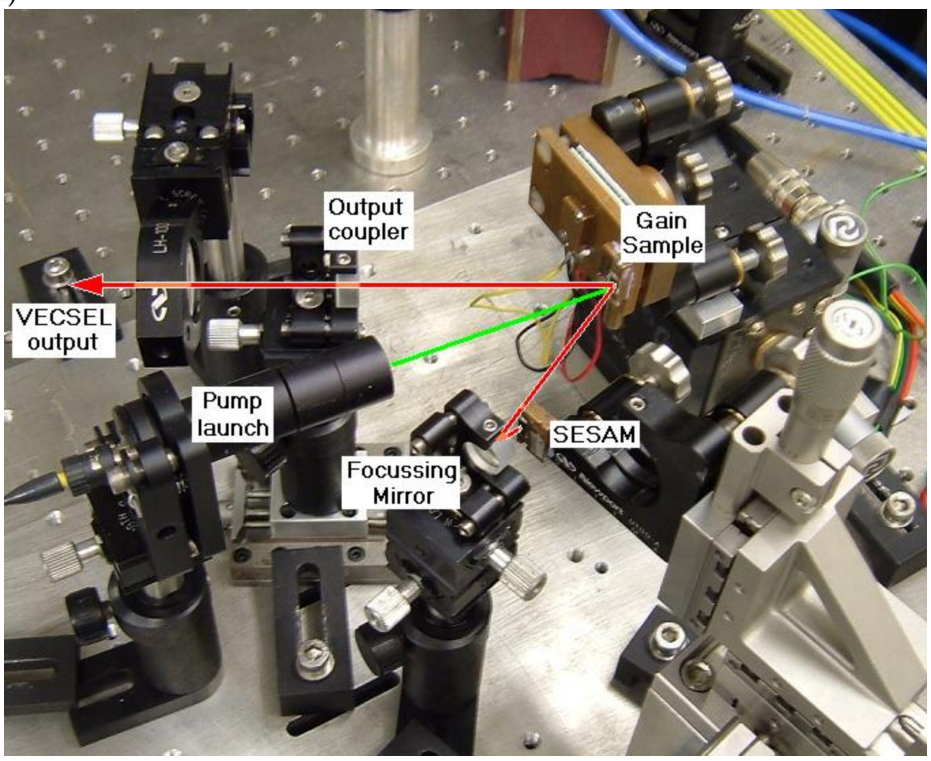

(b)

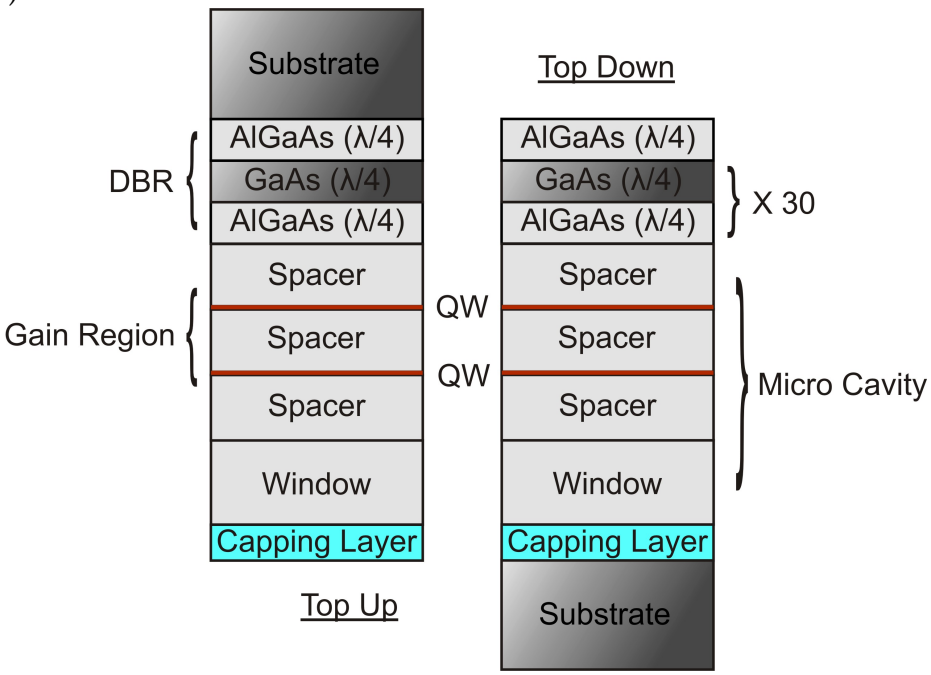

Figure 1.1: (a) An examle of a VECSEL cavity and, (b) a generic gain structure. The cavity is 1 GHz z-cavity including a semiconductor saturable absorber mirror (SESAM) for passive mode-locking of a VECSEL

ration of the external cavity not only makes the aformentiond possible, but enables increased functionality of the device by including aditional components within the cavity. In what follows each of these VECSEL features will be discussed in turn beginning with the possible pump arrangements, followed by the power scaling and spectral versatility; finaly the aplications enabled by the external cavity will be described.

There are a wide variety of sources available for pumping VECSELs. In the configuration of [2] the pump light was absorbed inside of the barrier material creating carriers which migrate into the quantum wells, this configuration is the simplest to implement, as the absorption is broad bandwidth the pump wavelength does not need to be stabilised. With barrier pumping there is a difference in energy between pump and laser wavelength due to the barrier height, this quantum defect results in heating of the VECSEL and reduces the efficiency of the device.

In-well pumping reduces the quantum defect and increases the efficiency of the device, however since absorption is only taking place inside of the quantum well, the total volume of absorber is greatly decreased. Up to 1.9 W output power has been reported for an in-well pumped VECSEL [4], which was pumped at 940 nm and lased at 980 nm; the slope efficiency was up to 35 % of the pump power where 70 % pump absorption was achieved. The pump efficiency can be increased still further by designing the DBR to reflect the pump light back through the sample, 80 % absorption has been reported with a 56 % slope conversion efficiency in a barrier pumping scheme [5]. A numerical study of the effect of pump reflections upon carrier generation has also been carried out [6].

In the schemes mentioned so far the pump is always introduced at an angle onto the front of the chip (intracavity), this geometry can be played with. By removing the substrate it is possible to pump the VECSEL at normal incidence through the DBR [7], this will reduce the asymmetry of the pumped region and allows for a more compact laser cavity. This technique is called end pumping, it requires a modification to the DBR to reduce the absorption of the pump and the incorporation of a heat spreader such as diamond; which is transparent to the pump light and can be capillary bonded to either side of the gain chip. This technique enables for pumping with a single edge emitting diode without the need for any additional optics [8].

Another pump scheme monolithically integrates the pump diode into the VEC-

SEL gain chip [9] achieving a CW output near 1000 nm of 0.65 W. Direct electrical pumping of VECSELs is possible, but requires a more complicated growth process and limits the output power; the highest CW power being reported to date is 10 mW [10].

The VECSEL is a power scalable device, meaning that for a particular gain chip it is possible to increase the output power simply by pumping a larger area of the gain chip with the same power density. However, if the pump spot is made too large, then the laser will favour a multimode output over TEM_{00}. The real limit to increased output power is down to pump induced heating of the gain. As the gain chip gets hotter processes such as auger recombination increase, this process in turn heats the sample eventually causing thermal runaway and the gain will be switched off.

There are a number of power scaling techniques available to the VECSEL all of which aim to reduce the thermal effects within the gain. Most of the heating arises from residual pump light being absorbed inside of the DBR and the substrate of the gain chip. As has been mentioned the DBR can be designed to reflect the pump light, greatly reducing pump heating. The second source of heat comes from the quantum defect of the particular material system; there are two techniques for removing this residual heat. The first is to remove the substrate and bond the DBR side of the sample onto a heat sink, this technique has been employed to achieve over 30 W CW [11] with an M^2 of 3 and 20 W with an M^2 of 1.1 [12]; the second source had a slope efficiency of 49 %.

The second technique is to capillary bond a diamond heat spreader onto the top of the gain chip (intracavity), for example 10 W has been achieved at 1060 nm [13]. An alternative power scaling technique is to incorporate more gain chips into the external cavity, this effectively reduces the thermal load upon each chip; up to 19 W has been demonstrated with two gain chips in the same cavity [14]. This technique has since been extended by Chilla et al. to over 70 W.

The highest power results, including all the aformentioned, have all been achieved close to 1 μm with InGaAs quantum wells. However, it should be noted that solid state and fibre lasers can perform equally well near 1 μm. For example 468 W has been obtained CW with an M^2 less than 1.5 by a Nd:YAG laser [15]. What the VECSEL architecture does offer over fibre lasers and most solid state lasers is wavelength versatility.

VECSELs have been demonstrated at wavelengths ranging from 338 nm [16] up to 2.36 μm [17]. A peak power of 1.7 W has been achieved at 2.35 μm where pulsed pumping of the gain chip was used as an aid to thermal managing the chip [18], and over 2 W at 2.35 μm with in-well pumping [19]. Watt level powers have also been achieved at fundamental wavelengths of 2 μm [20], 1.24 μm [21] and 675 nm [16]. This is not intended to be an exhaustive list of high power results; for a more detailed discussion of what is possible see [22].

Another interesting feature of the VECSEL is the ability to include different types of quantum wells grown at different wavelengths inside of a single gain chip; this can be used to enhance the gain bandwidth of the gain chip. Alternatively if the quantum wells are grown at two sufficiently different wavelengths, dual wavelength operation of the VECSEL can be achieved [23], making possible the generation of new wavelengths via sum frequency generation [6].

Quantum wells are not exclusively used as the VECSEL gain medium. Lasing near 5 μm has been achieved using bulk lead-chalcogenide as absorber and gain medium [24]. Lasing has also been achieved using layers of quantum dots as the gain medium [25], lasing at 1210 nm with an average power of 300 mW.

Most of the results at visible wavelengths have been achieved by frequency doubling of the VECSEL output. Because of the high beam quality and external cavity frequency, doubling can be achieved intra cavity yielding high conversion efficiencies and Watt level output. Frequency doubled VECSELs have a variety of applications such as projection displays [26], confocal microscopy [27] and forensics.

A variety of techniques become possible by incorporating other elements into the VECSEL cavity. Intracavity absorption spectroscopy is possible [28]. Heat spreaders [29] and etalons can be used as spectral filters, producing a narrow line width tunable source; a tuning range of 150 nm has been achieved from a single chip [1] near 2 μm. The multichip scheme can also be used to extend the gain bandwidth of the laser; a two chip VECSEL has been demonstrated with a tuning range of 33 nm [30] at a wavelength close to 1 μm, where the laser wavelength could be selected by an intra cavity birefringent filter.

1.1.1 Passive Mode-Locking

Mode-locking of a laser has the effect of compressing the intracavity energy in time and space, forming, in the case of fundamental mode-locking, a single optical pulse. This pulse will have a temporal duration that is inversely related to the frequency bandwidth of the pulse; that is to say that the number of optical modes simultaneously oscillating within the cavity determines the minimum temporal duration of the pulse. The laser output will be a train of identical pulses, each separated by the cavity round trip time. These pulses can be as short as a few femtoseconds at visible wavelengths with peak powers several orders of magnitude higher than in a CW laser.

The properties of mode-locked pulses are well known and there are many good books on the subject [31,32]. The application of ultra short pulses has been wide and varied including spectroscopy, material processing, generating attosecond pulses and in medical techniques such as optical coherence tomography.

The first CW pumped, passively mode-locked VECSEL was reported by Hoogland et al. in 2000 [33]. They achieved a train of 22 ps pulses at a repetition rate of 4.4 GHz with an average power of 21.6 mW. The gain chip contained 12 $In_{0.2}Ga_{0.8}As$ strain compensated quantum wells lasing at 1030 nm. A semiconductor saturable absorber mirror (SESAM) was used to obtain stable mode-locking. This type of mode-locking is a passive technique, requiring no active control of the mode-locking mechanism; it also has the advantage of being self starting unlike other passive techniques such as Kerr lens mode-locking. The technique of mode-locking a laser with a SESAM has been reviewed by U. Keller [34,35].

Sub-picosecond pulses have been reported in a number of publications including 290 fs pulses by P. Klopp et al. [36]. This result was achieved near 1036 nm with a graded index gain structure. A similar result has been achieved with a step index gain at a wavelength of 1035 nm. A train of 260 fs pulses was generated at a repetition rate of 1 GHZ by Wilcox et al. [37], the average power was 25 mW and the pulse train was 1.02 times transform limited. All the sub-picosecond results have been achieved using SESAMs that exploit the optical Stark effect as a pulse shaping mechanism as reported in [37].

The highest average power mode-locked results have also been achieved near 1 μm. A 4.7 ps pulse train has been reported [38] at a repetition rate of 4 GHz and

average power of 2.1 W. At other wavelengths a train of 18.7 ps pulses has been reported at a centre wavelength of 1.3 μm [39], the average power was 57 mW. A 2 GHz train of 20 ps pulses has been generated at a centre wavelength of 1550 nm with average power of 1 mW [40]. Intracavity frequency doubling has been employed with a mode-locked laser operating at a fundamental wavelength of 978 nm. To produce a train of 5.8 ps pulses at a centre wavelength of 489 nm with an average power of 6 mW [41].

Since the VECSEL architecture incorporates an external cavity, the repetition rate of such lasers can be varied by redesigning the cavity. Repetition rates longer than 1 GHz can be achieved and are desirable for certain biological imaging techniques where the dyes used have fairly long lifetimes. Due to the short carrier lifetime of the VECSEL the average power will eventually be limited with decreasing repetition rate. Secondly, at lower repetition rates VECSELs have a propensity to multiple pulse. However, mode-locking at longer repetition rates can be achieved by syncronously pumping the gain chip with a mode-locked source. For example, an 80 MHz VECSEL has been reported by synchronously pumping with a Ti:sapphire laser [42]. The pulses from this synchronously mode-locked VECSEL were highly chirped, and required external compression to reach sub-picosecond duration.

By decreasing the cavity length the repetition rate can be increased. There are a number of applications for high repetition rate lasers, such as optical sampling, which will be discussed in a later chapter of this thesis. The highest repetition rate sub picosecond result obtained to date is at 10 GHz [43]; a train of sub 500 fs pulses was obtained at a centre wavelength of 1034 nm with an average power of 30.3 mW. The highest repetition rate achieved to date has been 50 GHz with pulse duration of 3.1 ps [44]. This laser required a modified SESAM incorporating semiconductor quantum dots which have lower saturation fluence than quantum wells. The repetition rate was limited by the geometry of the z-cavity required for mode-locking. It could potentially be increased by using a linear cavity, which would require an output coupling SESAM [45] and intracavity focusing; this second requirement could be achieved by incorporating a micro lens into the gain chip as is done with micro cavity VECSELs operating CW [46]. Finally, the integration of both SESAM and gain into a single chip has been achieved [47], the device known as a mode-locked integrated external-cavity surface emitting laser (MIXSEL) generated a train of 35 ps pulses with

an average power of 40 mW at a repetition rate of 2.8 GHz.

1.2 VECSEL Seeded Ytterbium Doped Fibre Amplifiers

Ytterbium (Yb) doped lasers and amplifiers exhibit a broad gain bandwidth between approximately 975 and 1200 nm. In CW operation they can provide output powers of several kilowatts. The conversion efficiency of amplification can be very high, aproaching 80 %. When used as an amplifier, the nonlinear properties of the fibre can be exploited to alter the seed pulse both spectrally and temporally for example, fibre amplifiers have been used to compress cubically chirped pulses in time by compensating for both second and third order dispersion simultaneously in a technique known as cubicon amplification [48].

The shortest, sub-picosecond, pulses generated by VECSELs have been achieved at wavelengths, near 1μm using GaAs based gain material. These pulses have all had low average powers of less than 100 mW. The techniques for achieving multiwatt output powers with a VECSEL generally require post growth processing of the gain chip. Power scaling techniques also tend to reduce the gain bandwidth of the VECSEL, preventing sub-picosecond operation. The gain bandwidth of Ytterbium doped fibre coincides with that of the GaAs based VECSELs making it possible to amplify VECSEL pulses, at wavelengths near 1μm, in Ytterbium doped fibre amplifiers. Amplification of passively mode-locked VECSELs to multiwatt levels has been demonstrated by Dupriez et al. [49]. The combination of the two technologies has allowed for the scaling of the VECSEL average power to tens of Watts without the need for post growth processing of the semiconductor. A diagram of the master oscillator power amplifier (MOPA) used by Dupriez et al. can be seen in figure 1.2.

Two VECSEL MOPAs were demonstrated by Dupriez et al. both consisting of two stages. First the pulse train from a passively mode-locked VECSEL was amplified in a preamplifier to a couple of Watts, suitable to saturate the second stage of the MOPA. The second stage of the MOPAs were designed to amplify the pulse in one of two regimes. The first MOPA achieved over 200 W average power in an amplification regime dominated by self phase modulation (SPM), the resulting pulses were 4.6 ps in duration but exhibited a nonlinear chirp limiting the efficiency of pulse compression. The second amplifier was designed to achieve parabolic pulse amplification

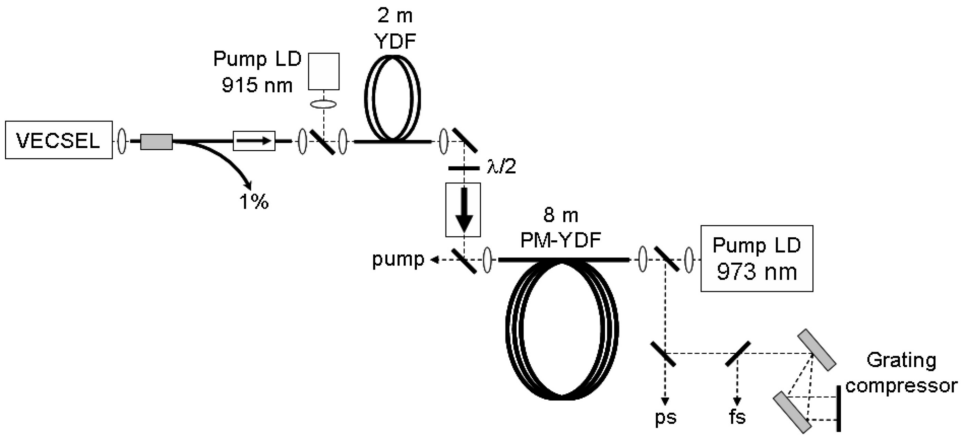

Figure 1.2: Configuration of the two stage VECSEL MOPA used in [49]: $(PM) - YDF$ (polarisation maintaing) ytterbium doped fibre, LD laser diode, $\lambda/2$ half wave plate, ps picosecond pulse pre compression, fs femtosecond pulse obtained after compression in a grating compressor.

and produced a linearly chirped pulse train with an average power of 53 W limited by the bandwidth of the fibre; these pulses were compressible down to 110 fs.

In conclusion, the VECSEL MOPA provides an alternative route to multiwatt operation of a VECSEL, with average powers exceeding those obtained by power scaling of CW-VECSELs. However, both the VECSEL MOPA and high power VECSELs [12,38] are complicated systems in comparison with the low power femtosecond VECSELs [33] which require no post growth processing. It will be shown later in this thesis that simpler, single stage amplifiers can be constructed with average powers exceeding 1.5 W.

1.2.1 Results Presented in this Thesis

The work reported in this thesis was motivated by a European funded collaboration called TeraSec, the aim of which was to develop sources of THz radiation for applications relating to homeland security. As part of this work the group here at Southampton has developed an all-semiconductor room-temperature terahertz time domain spectrometer [50]. In this work a pair of semiconductor antennas was used to generate and coherently detect THz radiation when illuminated by a 500 fs VECSEL pulse train with average power of a few milliwatts. To drive an array of antennas, as desirable for the TeraSec project, Watt level powers were needed with identical pulse

characteristics to the VECSEL used in [50]. To achieve this it was decided to employ Ytterbium-doped fibre to amplify the VECSEL pulse train.

The work in this thesis began with demonstrating amplification of VECSEL pulses to average powers exceeding 1.5 W using a single stage amplifier. This technique allows for preservation of the VECSEL pulse length and spectral characteristics. This result is an extension to the work previously reported upon a VECSEL-MOPA demonstrated by Pascal et al. Using single stage amplifiers allows for Watt level sources which are compact and robust, with the desirable characteristics of the shortest pulse VECSELs, without any need for post growth processing of the gain chip.

With average powers exceeding 1.5 W, the pulses from a VECSEL can experience sizeable nonlinear effects while propagating along a length of fibre. This fact can be exploited to spectrally broaden the pulse train. In chapter 6 the criteria for reaching the parabolic regime with a VECSEL seed are discussed. The design of a single stage amplifier is described along with modeling results to show the spectral and temporal profiles of the pulse train after propagating along the fibre. This amplifier was not realized experimentally, as the performance of the available VECSEL made it difficult to achieve any sizeable gain within the amplifier, at the wavelength of the VECSEL.

It was observed that the VECSELs used in this work tend to have a minimum pulse duration of around 500 fs that is not limited by the available bandwidth. Any particular 500 fs pulse train varies between transform limited and as much as two times transform limited, suggesting in some cases stable mode-locking with a sizeable intracavity dispersion. To asses the nature of this effect the phase structure of the chirped pulses has been measured for the first time to our knowledge using the technique of frequency resolved optical gating, results of these measurements are presented in section 3.

1.3 References

[1] Jonna Paajaste, Soile Suomalainen, Riku Koskinen, Antti Hrknen, Mircea Guina, and Markus Pessa. "High-power and broadly tunable GaSb-based optically pumped VECSELs emitting near 2 μm". *Journal of Crystal Growth*, In Press, Corrected Proof.

[2] M. Kuznetsov, F. Hakimi, R. Sprague, and A. Mooradian. "High-power (>0.5-W CW) diode-pumped vertical-external-cavity surface-emitting semiconductor lasers with circular TEM00 beams". *IEEE Photonics Technology Letters*, 9(8), 1997.

[3] A. C. Tropper and S. Hoogland. "Extended cavity surface-emitting semiconductor lasers". *Progress in Quantum Electronics*, 30(1):1–43, 2006.

[4] S. S. Beyertt, M. Zorn, T. Kubler, H. Wenzel, M. Weyers, A. Giesen, G. Trankle, and U. Brauch. "Optical in-well pumping of a semiconductor disk laser with high optical efficiency". *IEEE Journal of Quantum Electronics*, 41(12):1439–49, 2005.

[5] J. Y. Kim, S. Cho, S. M. Lee, G. B. Kim, J. Lee, J. Yoo, K. S. Kim, T. Kim, and Y. Park. "Highly efficient green VECSEL with intra-cavity diamond heat spreader". *Electronics Letters*, 43(2):105–7, 2007.

[6] Yu Morozov, T. Leinonen, M. Morozov, S. Ranta, M. Saarinen, V. Popov, and M. Pessa. "Effect of pump reflections in vertical external cavity surface-emitting lasers". *New Journal of Physics*, 10(6):063028 (10 pp.), 2008.

[7] Lee Jun Ho, Kim Jun Youn, Lee Sang Moon, Yoo Jae Ryung, Kim Ki Sung, Cho Soo Haeng, Lim Seong Jin, Kim Gi Bum, Hwang Sung Min, Kim Taek, and Park Yong Jo. "9.1-W High-Efficient Continuous-Wave End-Pumped Vertical-External-Cavity Surface-Emitting Semiconductor Laser". *Photonics Technology Letters, IEEE*, 18(20):2117–2119, 2006.

[8] Cho Soohaeng, Kim Gi Bum, Kim Jun-Youn, Kim Ki-Sung, Lee Sang-Moon, Yoo Jaeryung, Kim Taek, and Park Yongjo. "Compact and Efficient Green VECSEL Based on Novel Optical End-Pumping Scheme". *Photonics Technology Letters, IEEE*, 19(17):1325–1327, 2007.

[9] S. Illek, T. Albrecht, P. Brick, S. Lutgen, I. Pietzonka, M. Furitsch, W. Diehl, J. Luft, and K. Streubel. "Vertical-external-cavity surface-emitting laser with monolithically integrated pump lasers". *IEEE Photonics Technology Letters*, 19(24):1952–4, 2007.

[10] G. A. Keeler, D. K. Serkland, K. M. Geib, G. M. Peake, and A. Mar. "Single transverse mode operation of electrically pumped vertical-external-cavity surface-emitting lasers with micromirrors". *IEEE Photonics Technology Letters*, 17(3):522–4, 2005.

[11] Juan L. A. Chilla, Stuart D. Butterworth, Alexander Zeitschel, John P. Charles, Andrea L. Caprara, Murray K. Reed, and Luis Spinelli. "High-power optically pumped semiconductor lasers". In *Solid State Lasers XIII: Technology and Devices*, volume 5332, pages 143–150, San Jose, Ca, USA, 2004. SPIE.

[12] B. Rudin, A. Rutz, M. Hoffmann, D. J. H. Maas, A. R. Bellancourt, E. Gini, Su, uml, T. dmeyer, and U. Keller. "Highly efficient optically pumped vertical-emitting semiconductor laser with more than 20 W average output power in a fundamental transverse mode". *Optics Letters*, 33(22):2719–21, 2008.

[13] K. S. Kim, J. R. Yoo, S. H. Cho, S. M. Lee, S. J. Lim, J. Y. Kim, J. H. Lee, T. Kim, and Y. J. Park. "1060 nm vertical-external-cavity surface-emitting lasers with an optical-to-optical efficiency of 44 percent at room temperature". *Applied Physics Letters*, 88(9):91107–1, 2006.

[14] Fan Li, M. Fallahi, J. Hader, A. R. Zakharian, J. V. Moloney, J. T. Murray, R. Bedford, W. Stolz, and S. W. Koch. "Multichip vertical-external-cavity surface-emitting lasers: a coherent power scaling scheme". *Optics Letters*, 31(24):3612–14, 2006.

[15] J. Sabaghzadeh, F. Rahimzadeh, and I. Mashayekhe. "468-W CW operation of a diode-pumped Nd:YAG rod laser with high beam quality and highly efficient concentrator of pump light". *Optics and Laser Technology*, 40(5):748–55, 2008.

[16] Jennifer E. Hastie, Lynne G. Morton, Alan J. Kemp, Martin D. Dawson, Andrey B. Krysa, and John S. Roberts. "Tunable ultraviolet output from an intracavity frequency-doubled red vertical-external-cavity surface-emitting laser". *Applied Physics Letters*, 89(6):061114–3, 2006.

[17] A. Ouvrard, A. Garnache, L. Cerutti, F. Genty, and D. Romanini. "Single-frequency tunable Sb-based VCSELs emitting at 2.3 μm". *Photonics Technology Letters, IEEE*, 17(10):2020–2022, 2005.

[18] Nils Hempler, John-Mark Hopkins, Alan J. Kemp, Nico Schulz, Marcel Rattunde, Joachim Wagner, Martin D. Dawson, and David Burns. "Pulsed pumping of semiconductor disk lasers". *Opt. Express*, 15(6):3247–3256, 2007.

[19] N. Schulz, M. Rattunde, C. Ritzenthaler, B. Rosener, C. Manz, K. Kohler, and J. Wagner. "Effect of the cavity resonance-gain offset on the output power characteristics of GaSb-based VECSELs". *IEEE Photonics Technology Letters*, 19(21):1741–3, 2007.

[20] A. H*ä*rk*ö*nen, M. Guina, O. Okhotnikov, K. Rner, M. Hmmer, T. Lehnhardt, M. Mller, A. Forchel, and M. Fischer. "1-W antimonide-based vertical external cavity surface emitting laser operating at 2-m". *Opt. Express*, 14(14):6479–6484, 2006.

[21] J. Konttinen, A. Harkonen, P. Tuomisto, M. Guina, J. Rautiainen, M. Pessa, and O. Okhotnikov. "High-power (>1 W) dilute nitride semiconductor disk laser emitting at 1240 nm", 2007.

[22] N. Schulz, B. Rosener, R. Moser, M. Rattunde, C. Manz, Ko, uml, K. hler, and J. Wagner. "An improved active region concept for highly efficient GaSb-based optically in-well pumped vertical-external-cavity surface-emitting lasers". *Applied Physics Letters*, 93(18):181113 (3 pp.), 2008.

[23] T. Leinonen, Y. A. Morozov, A. Harkonen, and M. Pessa. "Vertical external-cavity surface-emitting laser for dual-wavelength generation". *IEEE Photonics Technology Letters*, 17(12):2508–10, 2005.

[24] M. Rahim, M. Arnold, F. Felder, K. Behfar, and H. Zogg. "Midinfrared lead-chalcogenide vertical external cavity surface emitting laser with 5 mu m wavelength". *Applied Physics Letters*, 91(15):151102–3, 2007.

[25] T. D. Germann, A. Strittmatter, J. Pohl, U. W. Pohl, D. Bimberg, J. Rautiainen, M. Guina, and O. G. Okhotnikov. "Temperature-stable operation of a quantum dot semiconductor disk laser". *Applied Physics Letters*, 93(5):051104–1, 2008.

[26] L. A. Chilla Juan, Zhou Hailong, Weiss Eli, L. Caprara Andrea, Shou Qi-Ze, V. Govorkov Sergei, K. Reed Murray, and Spinelli Luis. "Blue and green optically pumped semiconductor lasers for display", 2005.

[27] E. Esposito, S. Keatings, K. Gardner, J. Harris, E. Riis, and G. McConnell. "Confocal laser scanning microscopy using a frequency doubled vertical external cavity surface emitting laser". *Review of Scientific Instruments*, 79(8):083702–1, 2008.

[28] A. Campargue, Y. Ding, E. Bertseva, S. Tashkun, and V. I. Perevalov. "Highly sensitive absorption spectroscopy of carbon dioxide by ICLAS-VeCSEL between 8800 and 9530 cm-1". *Journal of Molecular Spectroscopy*, 231(2):117–23, 2005.

[29] H. Lindberg, M. Strassner, and A. Larsson. "Improved spectral properties of an optically pumped semiconductor disk laser using a thin diamond heat spreader as an intracavity filter". *IEEE Photonics Technology Letters*, 17(7):1363–5, 2005.

[30] Fan Li, M. Fallahi, A. R. Zakharian, J. Hader, J. V. Moloney, R. Bedford, J. T. Murray, W. Stolz, and S. W. Koch. "Extended tunability in a two-chip VECSEL". *IEEE Photonics Technology Letters*, 19(8):544–6, 2007.

[31] E. Siegman, A. *Lasers*. university Science Books, 1986.

[32] N. Trager, F. *Springer Handbook of Lasers and Optics*. Springer, 2007.

[33] S. Hoogland, S. Dhanjal, A. C. Tropper, J. S. Roberts, R. Haring, R. Paschotta, F. Morier-Genoud, and U. Keller. "Passively mode-locked diode-pumped surface-emitting semiconductor laser". *Photonics Technology Letters, IEEE*, 12(9):1135–1137, 2000.

[34] U. Keller, K. J. Weingarten, F. X. Kartner, D. Kopf, B. Braun, I. D. Jung, R. Fluck, C. Honninger, N. Matuschek, and J. Aus der Au. "Semiconductor saturable absorber mirrors (SESAM's) for femtosecond to nanosecond pulse generation in solid-state lasers". *Selected Topics in Quantum Electronics, IEEE Journal of*, 2(3):435–453, 1996.

[35] Ursula Keller and Anne C. Tropper. "Passively modelocked surface-emitting semiconductor lasers". *Physics Reports*, 429(2):67–120, 2006.

[36] P. Klopp, F. Saas, U. Griebner, M. Zorn, and M. Weyers. "Passively mode-locked semiconductor disk laser generating sub-300-fs pulses". 2008 Conference on Lasers and Electro-Optics (CLEO), page 2 pp., Piscataway, NJ, USA, 2008. IEEE.

[37] K. G. Wilcox, Z. Mihoubi, G. J. Daniell, S. Elsmere, A. Quarterman, I. Farrer, D. A. Ritchie, and A. Tropper. "Ultrafast optical Stark mode-locked semiconductor laser". *Optics Letters*, 33(23):2797–9, 2008.

[38] A. Aschwanden, D. Lorenser, H. J. Unold, R. Paschotta, E. Gini, and U. Keller. "2.1-W picosecond passively mode-locked external-cavity semiconductorlaser". *Opt. Lett.*, 30(3):272–274, 2005.

[39] A. Rutz, V. Liverini, E. Muller, S. Schon, and U. Keller. "All-GaInNAs ultrafast lasers: Material development for emitters and absorbers". *Journal of Crystal Growth*, 301-302:525–8, 2007.

[40] A. Khadour, S. Bouchoule, G. Aubin, J. P. Tourrenc, A. Miard, J. C. Harmand, J. Decobert, and J. L. Oudar. "Mode locked 1550 nm VECSEL using a two quantum wells GaInNAs saturable absorber". 2008 Conference on Lasers and Electro-Optics (CLEO), page 2 pp., Piscataway, NJ, USA, 2008. IEEE.

[41] O. Casel, D. Woll, M. A. Tremont, H. Fuchs, R. Wallenstein, E. Gerster, P. Unger, M. Zorn, and M. Weyers. "Blue 489-nm picosecond pulses generated by intracavity frequency doubling in a passively mode-locked optically pumped semiconductor disk laser". *Applied Physics B: Lasers and Optics*, 81(4):443–446, 2005.

[42] Wei Zhang, Thorsten Ackemann, Marc Schmid, Nigel Langford, and Allister Ferguson. "Femtosecond synchronously mode-locked vertical-external cavity surface-emitting laser". *Opt. Express*, 14(5):1810–1821, 2006.

[43] S. Hoogland, A. Garnache, I. Sagnes, J. S. Roberts, and A. C. Tropper. "10-GHz train of sub-500-fs optical soliton-like pulses from a surface-emitting semiconductor laser". *IEEE Photonics Technology Letters*, 17(2):267–9, 2005.

[44] D. Lorenser, D. J. H. C. Maas, H. J. Unold, A. R. Bellancourt, B. Rudin, E. Gini, Ebling Dirk, and U. Keller. "50-GHz passively mode-locked surface-emitting semiconductor laser with 100-mW average output power". *IEEE Journal of Quantum Electronics*, 42(8):838–47, 2006.

[45] G. J. Spühler, S. Reffert, M. Haiml, M. Moser, and U. Keller. "Output-coupling semiconductor saturable absorber mirror". *Applied Physics Letters*, 78(18):2733–2735, 2001.

[46] Si-Hyun Park and Heonsu Jeon. "Microchip-Type InGaN Vertical External-Cavity Surface-Emitting Laser". *Optical Review*, 13(1):20–23, 2006.

[47] B. Rudin, D. J. H. C. Maas, A. R. Bellancourt, M. Golling, T. Sudmeyer, and U. Keller. "Vertical integration of ultrafast semiconductor lasers". 2008 Quantum Electronics and Laser Science Conference (QELS), page 2 pp., Piscataway, NJ, USA, 2008. IEEE.

[48] Lawrence Shah, Zhenlin Liu, Ingmar Hartl, Gennady Imeshev, Gyu Cho, and Martin Fermann. "High energy femtosecond Yb cubicon fiber amplifier". *Opt. Express*, 13(12):4717–4722, 2005.

[49] P. Dupriez, C. Finot, A. Malinowski, J. K. Sahu, J. Nilsson, D. J. Richardson, K. G. Wilcox, H. D. Foreman, and A. C. Tropper. "High-power, high repetition rate picosecond and femtosecond sources based on Yb-doped fiber amplification of VECSELs". *Optics Express*, 14(21), 2006.

[50] Z. Mihoubi, K. G. Wilcox, S. Elsmere, A. Quarterman, R. Rungsawang, I. Farrer, H. E. Beere, D. A. Ritchie, A. Tropper, and V. Apostolopoulos. "All-semiconductor room-temperature terahertz time domain spectrometer". *Optics Letters*, 33(18):2125–7, 2008.

Chapter 2

Theory of Passively Mode-Locked VECSELs

The work presented in this thesis concerns the phase characterisation of a VECSEL pulse train and the amplification of such pulse trains in Yb-doped fibre. To interpret the results of these experiments, it is important to understand how the pulse train is formed within a VECSEL. The gain chips used in this work all came from the same semiconductor wafer, grown by metal-organic vapour-phase epitaxy (MOVPE) by Dr. John Roberts at the EPSRC III-V semiconductor growth facility in Sheffield; the SESAMs were all from a second wafer, again grown at Sheffield. A typical arrangement of a VECSEL is shown in figure 2.1 including the gain chip (QT1544) and SESAM (QT1627) structures used throughout this thesis.

The passively mode-locked VECSEL consists of three elements: an external cavity including pump source, a gain chip and a SESAM. A single design of z-cavity was used to produce pulse trains near 1 GHz. The gain chip grown on a GaAs substrate contained a distributed Bragg reflector (DBR) formed by 27.5 pairs of AlAs/GaAs layers. On top of this, a gain region is formed containing 6 quantum wells designed to emit at 1010 nm, at room temperature under low excitation. The whole structure including DBR was designed for a wavelength of λ_0= 1030 nm. The window layer of the structure was chosen to have an optical thickness of $d_{wl} = \lambda_0/4$ including an 8 nm capping layer. The active region was designed to have an optical thickness of $d_{ar} = 7\lambda_0/2$. Thus the sliver of material grown on top of the DBR has a total thickness $D = d_{wl} + d_{ar} = 15\lambda_0/4$, which forms a micro cavity that is anti resonant at 1030 nm, at room temperature under low excitation.

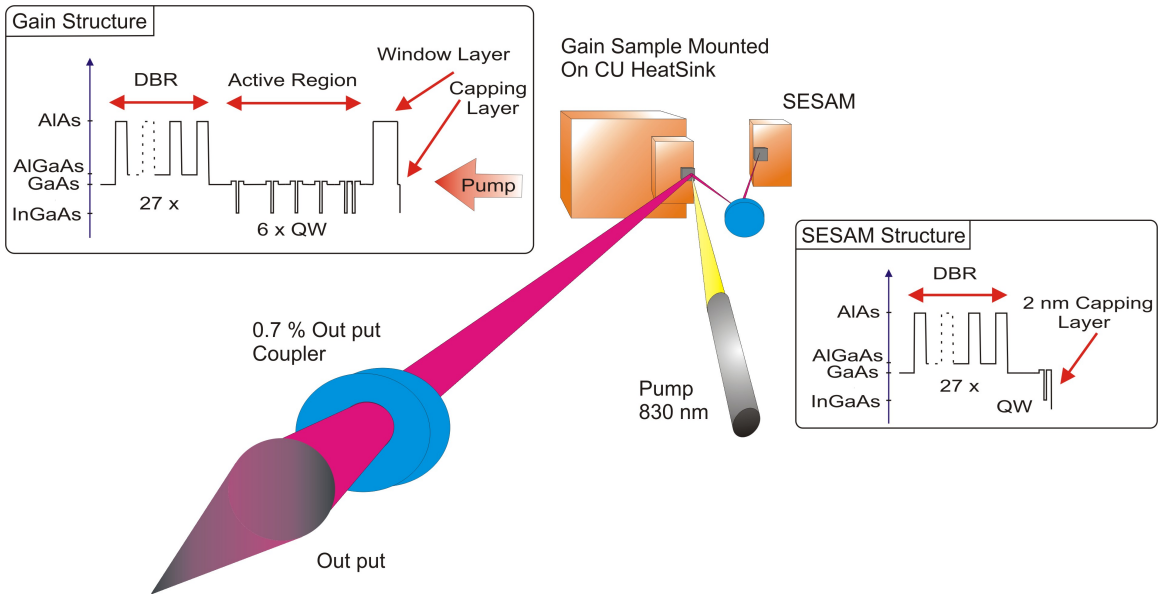

Figure 2.1: Set up of a 1 GHz passively mode-locked VECSEL. An 830 nm fibre-coupled diode, delivering up to 1.3 W is used for pumping the gain chip. A pair of lenses (not shown) are used to form a 2:1 image of the output from the fibre, giving a 60 μm radius spot upon the gain chip. The properties of the external cavity will be discussed later in section 2.2.1. The inset layer structures are for the gain (QT1544) and the SESAM (QT1627) used in this thesis.

The SESAM was designed to exploit the optical Stark effect [1]. It contained a 27.5 pair DBR with design wavelength of 1040 nm. A single quantum well designed at 1025 nm was grown 2 nm below the surface, allowing for fast recombination ($<$ 2 ps) of excited carriers by tunnelling between surface states. This quantum well was separated from the DBR by a $0.68\lambda_0/4$ spacer layer of GaAs.

It is the purpose of this chapter to describe the design of the three VECSEL elements used in passive mode-locking; the chapter is divided into the following sections. Firstly, in section 2.1 optical properties of the semiconductor materials used in both the gain chip and the SESAM will be described. Also, in section 2.1 the structural properties of the active mirror including the effect of the DBR, micro cavity and quantum confinement within the quantum wells will be described. In section 2.2 the technique of passive mode-locking with a SESAM will be introduced along with the design of the external cavity to facilitate stable mode-locking. Finally, in section 2.3 characterisation data will be presented to illustrate the operating regime of the VECSELs used in this work.

2.1 The VECSEL Gain Chip

2.1.1 Semiconductor Materials

Most semiconductor lasers exploit the optical properties of III-V semiconductors to achieve lasing. By changing the composition of the material being used, or altering the dimensionality of the structure, the semiconductor band gap can be altered giving access to different wavelength regimes. The possible combinations of semiconductor materials for VECSELs is, however, limited by the need to lattice match the material systems to each other and in particular to the semiconductor substrate upon which the gain chip will be grown. A plot of bandgap energy against lattice constant is shown in figure 2.2 for several III-V semiconductor alloys.

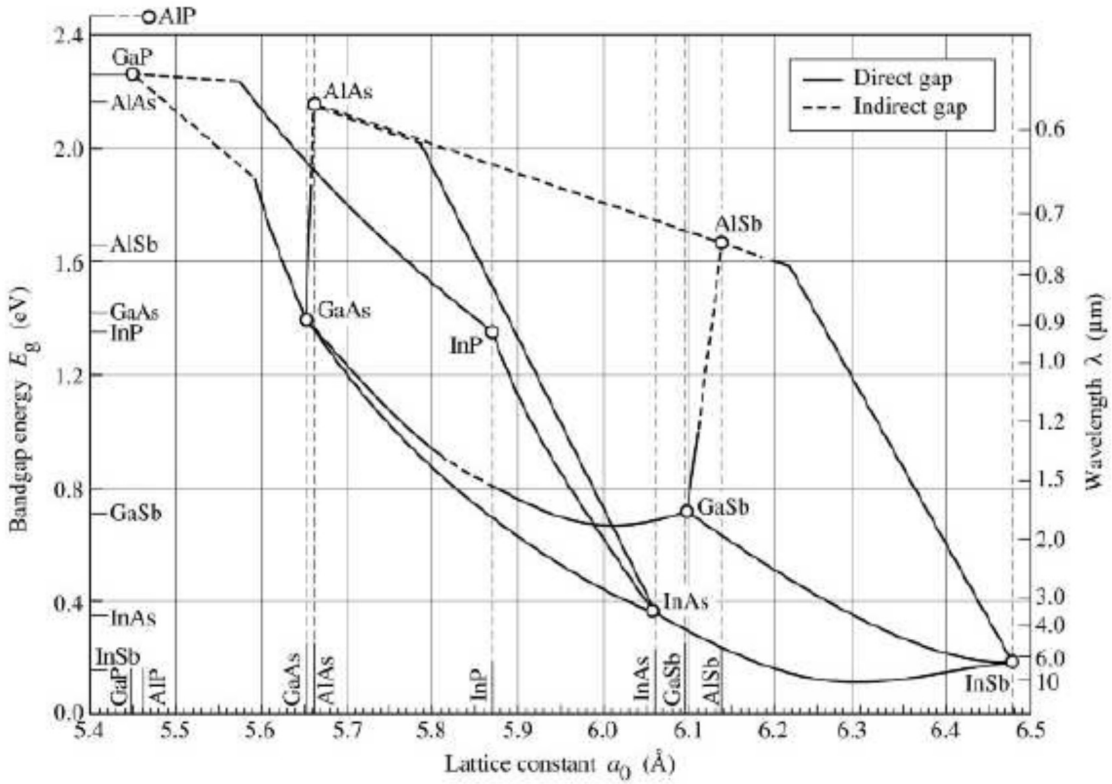

Figure 2.2: Bandgap energy and lattice constant for several III-V semiconductor materials at room temperature, taken from [2].

The VECSEL used in this work contains a GaAs/AlAs DBR grown on top of a GaAs substrate and employs 6 $GaAsP_{0.06}/In_{0.23}Ga_{0.77}As/GaAsP_{0.06}$ quantum wells as a gain medium. From figure 2.2 it can be seen that GaAs is very closely lattice

matched to AlAs. However, by incorporating In_y atoms into the Ga_xAs lattice to form the quantum wells the lattice constant of the material is increased. This increase in lattice constant introduces strain between the quantum well and the barrier material, which has a smaller lattice constant. The effect of strain can be beneficial; it will shift the bandgap energy while increasing the peak and differential gain. However, too much strain will reduce the lifetime of the structure or even prevent a successful growth. In some cases it is possible to compensate for strain by incorporating another element into the material between the quantum wells and the barriers; this has been done with the gain chip used in this thesis by introducing strain compensating $GaAsP_{0.06}$ layers around each quantum well.

The gain chip used in this thesis was designed to be optically pumped, with light being absorbed within the GaAs barrier/spacer layers surrounding each quantum well. The absorbed light creates free carriers within the semiconductor which become trapped within the thin quantum wells of the gain region; if enough carriers are trapped a population inversion is achieved and lasing will become possible. To understand how these processes come about an understanding of the band structure of a semiconductor is required. By solving Schrödinger's equation for a particle in a box with a periodic potential it is found that the electrons within a semiconductor can have only specific values of kinetic energy. In the case of a bulk semiconductor, by assuming that the energy bands are parabolic, these energy levels can be approximated by the relationships [3]

$$E_2(\mathbf{k}) = E_c + \frac{\hbar^2 k_2^2}{2m_c}, \quad E_1(\mathbf{k}) = E_v + \frac{\hbar^2 k_1^2}{2m_v} \tag{2.1}$$

Where $m_{c/v}$ is the effective mass of an electron/hole in the conduction/valence band. Bands of allowed energy states exist within the semiconductor, with the state of an electron being determined by the momentum and spin of each electron. In figure 2.3 a) the band structure of bulk GaAs is plotted; the shaded region indicates the extent of the semiconductor bandgap in GaAs. The accompanying plot (b) is a parabolic aproximation to this bandstructure, in which four characteristic time scales for the optical excitation of an electron into the conduction band are indicated. Since the minimum energy of the conduction band coincides in k-space with the maximum energy of the valence band, GaAs is termed a direct gap semiconductor; this will result in faster carrier recombination times than with indirect semiconductors.

Optical transitions between bands are allowed provided that the transition conserves both momentum and energy; thus it is necessary that incident photons have energy greater than the band gap of the semiconductor in order to promote an electron from the valence band to the conduction band. An electron excited into the conduction band will leave a positively charged hole in the valence band; these electrons will undergo a number of relaxation processes (indicated in figure 2.3 b) by the Roman numerals I-IV) before finally recombining with a hole in the valence band.

(a) (b)

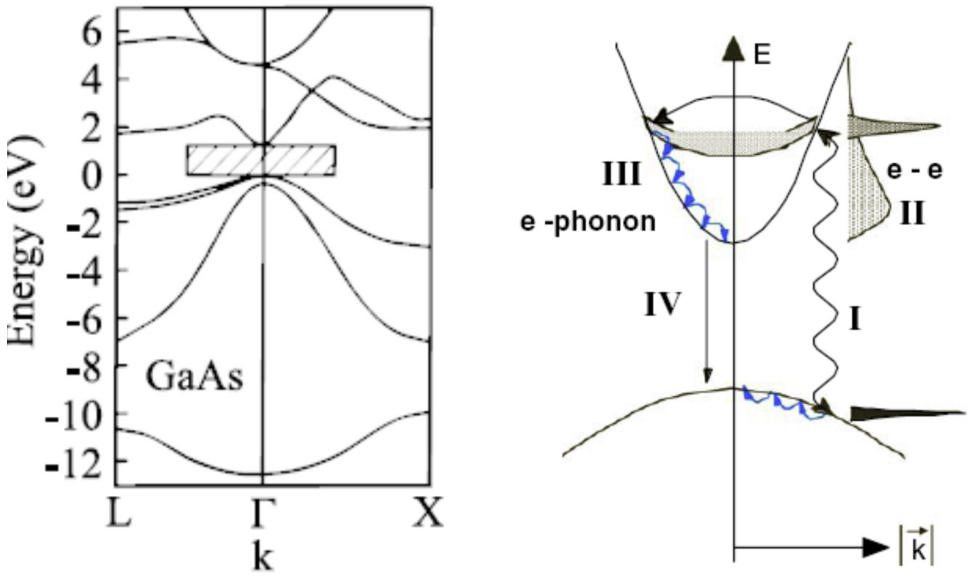

Figure 2.3: a) Band structure of bulk GaAs, taken from [2]; b) parabolic band structure showing four time regimes for the decay of excited electrons from the conduction band into the valence band, taken from [4]

The coherence of the electrons excited to the conduction band will disappear over a time scale of less than 100 fs due to scattering events, indicated in figure 2.3 b) by the Roman numeral (I). The initial electron population created by photon absorption will have a non thermal distribution. Over time (II) energy is redistributed amongst this population mostly by electron-electron scattering; after approximately 100 fs a quasi-thermal equilibrium state is reached. In general, the thermalised electron population will have a characteristic temperature greater than the lattice temperature and will occupy states higher up in the conduction band. The excited electrons will eventualy drop down to the bottom of the conduction band via phonon scattering (III), this process may take tens of picoseconds and results in lattice heating. The final relaxation

process (IV) takes the longest time. Electrons recombine with holes in the valence band by photon emission on a nanosecond time scale.

At higher energy densities Auger processes become important, energy maybe transfered between two electrons within the conduction band, enabling for the non-radiative recombination of one electron by transfering energy to a second electron within the conduction band. Electrons excited, via Auger recombination, to higher states within the conduction band will eventualy loose energy through phonon scattering; Auger processes reduce the optical efficiency of semiconductor lasers resulting in heating of the semiconductor lattice.

In thermal equilibrium, the probabliity that an electron will occupy a level with energy E is given by the Fermi-Dirac distribution

$$f(E) = \frac{1}{1 + e^{(E-E_F)/k_B T}}, \tag{2.2}$$

where E_F is the Fermi level and k_B the Boltzmann constant. The total carrier density can be determined by the Fermi level and the density of states [5] and is given by the following equation:

$$N_\alpha = \int_0^\infty \rho_\alpha(E_\alpha) f_\alpha(E_\alpha) dE_\alpha. \tag{2.3}$$

Where $\rho_\alpha(E_\alpha)$ is the energy density of states and $f_\alpha(E_\alpha)$ is the Fermi-Dirac distribution of the carriers (the subscript α is to indicate that the distribution could be of holes or electrons).

2.1.2 Distributed Bragg Reflector

The VECSEL architecture incorporates a distributed Bragg reflector (DBR) into the gain chip, which acts to reflect laser light at the design wavelength and attenuates any residual pump light. Such a DBR will contain layers of semiconductor with alternating high and low refractive index, each layer grown to have an optical thickness equal to one quarter of the design wavelength. In figure 2.4 the principal of a DBR is illustrated. It is possible to calculate the reflectivity of structures such as the DBR by means of a multilayer calculation implemented in previous work by this group [2,6]. The technique imposes boundary conditions at every material interface within a multilayer structure and is capable of calculating the E-field as a function of wavelength at any location within the sample. The calculated reflectivity of the gain structure used in this thesis is shown in figure 2.5.

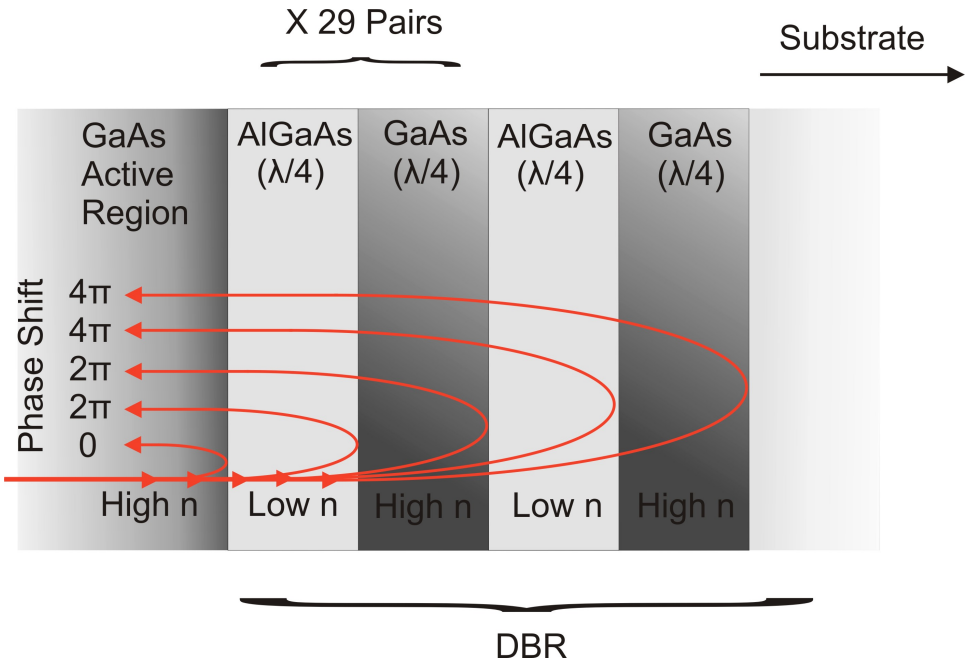

Figure 2.4: Distributed Bragg reflector structure enables constructive interference of the partial reflections from each quarter λ layer resulting in > 99 % reflectivity. Here λ is the wavelength of light within the material.

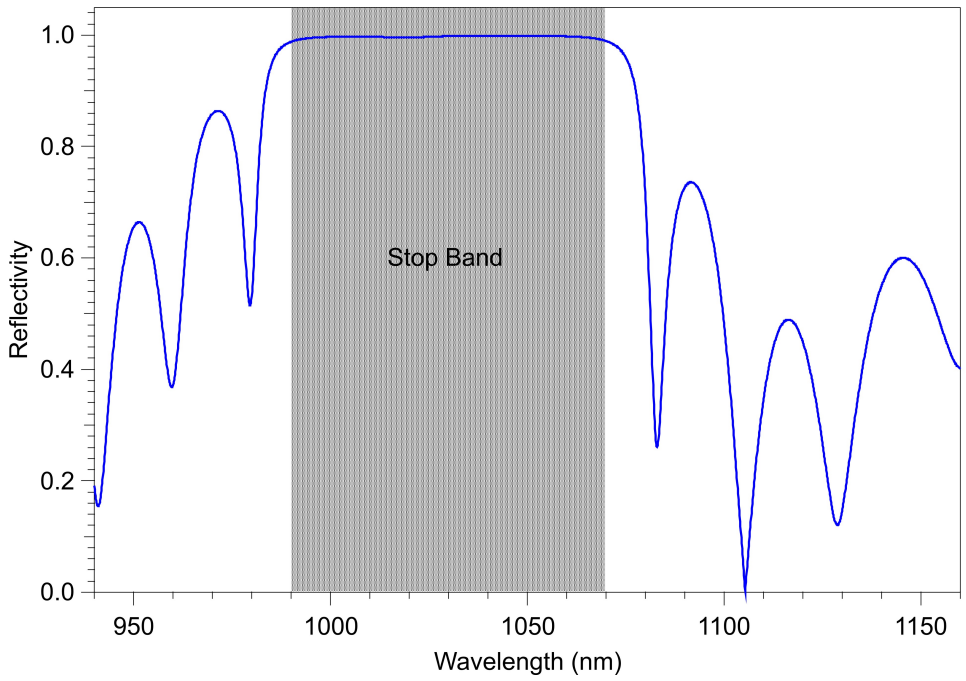

Figure 2.5: Calculated reflectivity for the gain sample QT1627 used in this thesis (excluding absorption effects).

Light incident upon the front surface of a DBR will see an alternating sequence of high and low index material, and at each boundary between high and low index this light will be partially reflected. When passing through the material, light will experience a phase change of $\frac{\pi}{2}$ between successive quarter-wave layers: in addition light undergoes a phase change of π when reflected from a high index layer into a low index layer, and zero phase change when reflected into a high index material. Because each layer is a quarter wavelength thick, the partial reflections from different depths inside of the DBR will interfere constructively resulting in > 99 % reflectivity for the material system as illustrated in figure 2.4.

The gain chip used in this thesis was grown with the DBR on top of the GaAs substrate; this is called a top up growth as has been illustrated in figure 1.1. The DBR contained 27.5 pairs of GaAs/AlAs layers with a design wavelength of 1030 nm. The theoretical reflectivity of this structure can be seen in figure 2.5. The DBR has an approximately 80-nm-broad stop band centred at 1030 nm, over which it has a > 99 % reflectivity. The width of this stop band is determined by the refractive index contrast between the layers in the DBR, while the overall reflectivity increases with increasing number of pairs of layers.

2.1.3 Quantum Well Gain Medium

The number of excited electrons required to reach transparency depends critically upon the density of states. The density of states can be altered by reducing one, or more, of the semiconductor dimensions to less than the Fermi wavelength; this length is typically of order 10 nm.

In table 2.1 the density of states of the four obtainable semiconductor dimensionalities is shown, for the: quantum dot (0D), quantum well (1D) wire and the bulk (3D) material. References provide examples of the use of such dimensionalities in a VECSEL architecture. As of yet a 2D confined structures has not been used with the VECSEL format, however the incorporation of carbon nanotubes into a mirror to form a SESAM [7] may prove useful to mode-locking a VECSEL due to the faster recovery time of the absorber.

An energy diagram of a strain-compensated quantum well is depicted in figure 2.6. Note that the axis are not to scale. The zero-point energy of an electron within the conduction band and a hole in the valence band of the quantum well will

Dimesionality	Density of States	Reference
3 D	$\mathrm{D(E)dE} = \frac{1}{2\pi^2}\left(\frac{2m}{\hbar^2}\right)^{\frac{3}{2}}\sqrt{E}dE$	[8]
2 D	$\mathrm{D(E)dE} = \frac{m}{\pi\hbar^2}dE$	[9]
1 D	$\mathrm{D(E)dE} = \frac{1}{\pi}\left(\frac{m}{\hbar^2}\right)^{\frac{1}{2}}\frac{1}{\sqrt{E}}dE$	
0 D	$\mathrm{D(E)dE} = 2\delta_E dE$	[10]

Table 2.1: Density of semiconductor states per unit volume for four different dimensionalities of semiconductor: quantum dot (0D), quantum wire (1D), quantum well (2D) and bulk.

be greater than that expected from the same bulk material alone. This energy can be found by solving Schrödinger's equation for a particle in a one dimensional box, where the potential barrier is equal to the difference in band edge energy between the strain compensating layers and the quantum well material. The absorption edge of the quantum well is given by the energy difference between the N = 1 state within the conduction band and the N = 1 state within the valence band and can be engineered by changing the concentration of indium within the quantum well or by altering the width of the quantum well.

The density of states for a quantum well has a step-like dependence upon energy due to the confinement along the z-direction as depicted in figure 2.6 b). Electrons which are optically excited into the conduction band of the barrier material will drop into the quantum well provided that the energy of the electron is greater than the 54 meV barrier of the strain compensating layer (approximately twice room temperature). The radiative transition rate, the probability of a transition per second per unit volume of the active material, from the N = 1 quantum well conduction band to the N = 1 valence band is given by equation 2.4 [11]:

$$R_\tau = \frac{1}{2}\frac{e_0^2\lambda}{e\epsilon_0 M_e^2 n^2} N_p \left|M_T\right|^2 \rho_J^{QW}\left(\hbar\omega\right), \tag{2.4}$$

where N_p is the number of photons per unit volume, ρ_j^{QW} is the density of states, M_e is the effective mass of the electron and $|M_T|^2$ is the transition matrix element.

The stimulated emission rate is given by the product of the transition probability with the probability of an electron being in the conduction band, with a particular k-vector and the corresponding valence band state being empty, and is given by

equation 2.5. Conversely the stimulated absorption rate is given by equation 2.6:

$$R_{se} = R_\tau f_c \left(1 - f_v\right), \tag{2.5}$$

and

$$R_{sa} = R_\tau f_v \left(1 - f_c\right); \tag{2.6}$$

where $f_{c/v}$ are the Fermi distributions of the condution/valence bands given by equation 2.2.

Each quantum well within the gain sample will contribute gain when the stimulated emission rate of the well exceeds the stimulated absorption rate. The material gain per unit length, defined as the net growth of the photon density as it propagates through a quantum well in the z direction is given by:

$$g = \frac{1}{2}\frac{e_0^2\lambda}{c^2\epsilon_0 m_e^2 n}\left|M_T\right|^2 \rho_J^{QW}\left(\hbar\omega\right)\left(f_c - f_v\right) \tag{2.7}$$

where n is the refractive index of the quantum well. The total gain of each quantum well within the VECSEL is given by the electric field intensity upon each well and the material gain g. The magnitude of the electric field E(λ, x) and thus the quantum well gain, depends both upon the location within the VECSEL microcavity (x) and the thickness of the microcavity. The structural dependence of gain from a VECSEL chip will be discussed in section 2.1.4. The relationship for the material gain given in equation 2.7 has a sharp cut-off toward the long wavelength side of the spectrum. There are a number of effects that have not been included in equation 2.7 which alter the spectrum leading to a broader cut-off. One such effect that is intra-band scattering, which should be included as a Lorenzian linewidth function. Equation 2.7 also does not include Coulomb effects and bandgap renormalisation, which will slightly alter the gain spectrum [12]. Equation 2.7 gives an estimate of the maximum gain per quantum well of 0.6 %, and a carrier density at transparency of 0.88×10^{18} cm^{-3}; while the total loss of the VECSEL cavity used in this work is around 2 %.

Electrons excited to the conduction band can recombine with holes in the valence band by radiative and non-radiative processes. The lifetime of the excited state within the conduction band is given by the following empirical relationship [11]:

$$\frac{N}{\tau_{level}} = A_d N + \frac{BN}{L_{QW}} + C_A\left(\frac{N}{L_{QW}}\right)^2, \tag{2.8}$$

where L_{QW} is the width of the quantum well and N is the number of excited carriers.

The density of defect sites within the quantum well is represented by the constant A_d; this number can be very low, around 10^{15}cm^{-3} under optimum growth conditions. However, as the growth temperature is lowerd below the optimum temperature, A_d will increase. B is the radiative recombination coefficient. C_A is the Auger coefficient representing the dominant source of non-radiative loss within the quantum well. The rate of Auger recombination has dependence upon N^2, it also increases with increasing temperature. The radiative recombination rate, given by the second term in equation 2.8 has a linear dependence upon carrier density. It is thus important to keep the carrier density low; since the Auger recombination rate will increase faster with increasing N than the radiative recombination rate affecting the efficiency of the device. The quantum efficiency of spontaneous emission from the quantum well can be expressed as the ratio of the radiative recombination lifetime to the total lifetime of recombination:

$$\eta_i = \frac{\tau_{level}}{L_{QW}/BN} = \frac{\tau_{level}}{\tau_{rad}}. \tag{2.9}$$

The quantum efficiency near transparency can be high, typically around 80 %. This figure will decrease with increasing carrier density and temperature, largely due to Auger recombination.

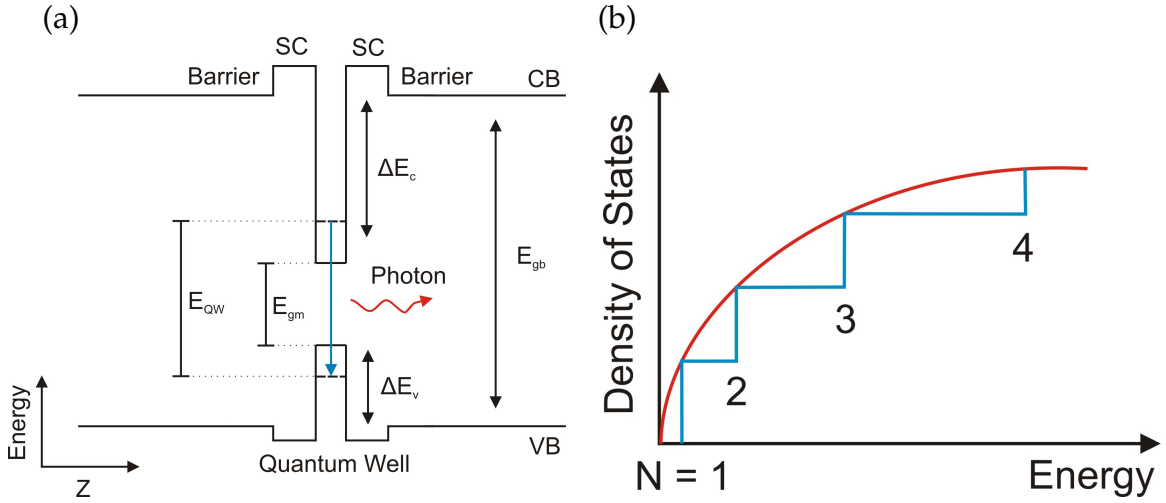

Figure 2.6: a) Diagram of a strain compensated quantum well showing material bandgap energy and the quantum well emission. b) The density of states for a quantum well, blue(step) and for bulk (red curve). SC = strain compensation layer, CB = conduction band, VB = valence band, and E_{gm} (E_{QW}) is the bandgap of the bulk (quantum well) material.

2.1.4 Microcavity Effects

The gain, emission wavelength and quantum efficiency depend upon the number of carriers inside each quantum well, and hence upon the number of carriers created by pump absorption within the barrier regions. In figure 2.7 the location of the quantum wells within the gain sample (QT1544) used in this thesis is shown, along with the percentage of absorbed pump at the location of each quantum well calculated from a Beers law absorption model. The quantum wells have been arranged to give a similar number of carriers per quantum well within the gain sample, ensuring maximum gain at the design wavelength.

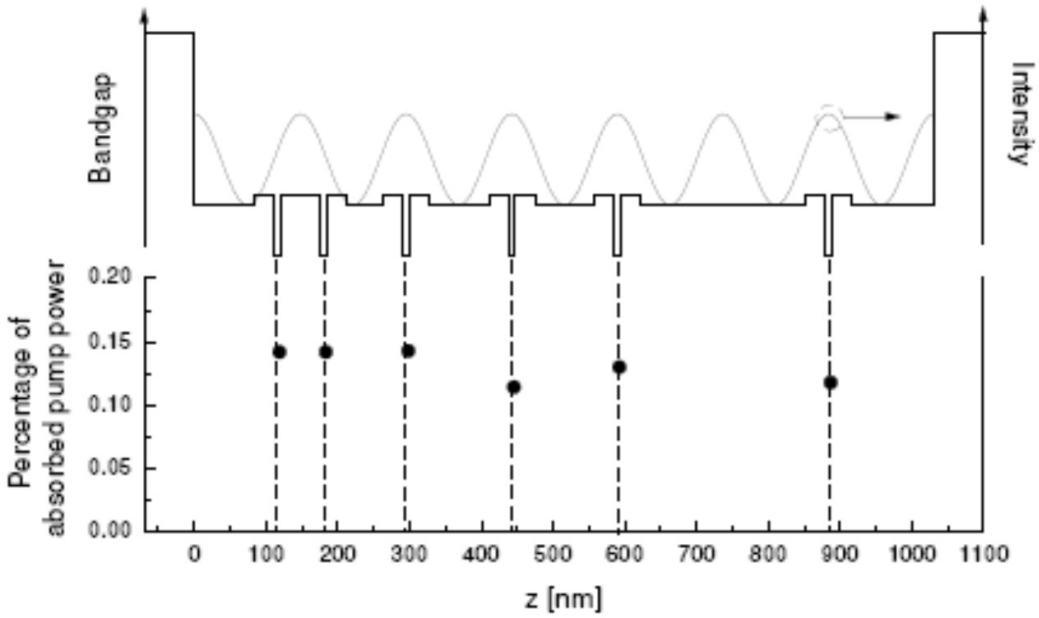

Figure 2.7: Top: active region of QT1544 showing the position of the six quantum wells along with the intensity distribution at the design wavelength. Bottom: Percentage of absorbed pump light available to create carriers at each quantum well. Taken from [2].

The gain at a particular wavelength has dependence upon the optical field at that wavelength local to each quantum well, as mentioned in section 2.1.3; for maximum gain the quantum wells need to be positioned at the anti nodes of the standing wave formed within the gain region of the chip. The VECSEL gain region forms an etalon between the top of the DBR and the surface of the chip; the thickness of the etalon

will greatly affect the size of the E-field within the gain region relative to the incident E-field. The total gain of the VECSEL is thus structure-dependent and is given by the material gain of the quantum wells multiplied by the microcavity enhancement factor, Gain $= g\Gamma_z$ [4], where

$$\Gamma_z = \frac{\sum_q \left|E\left(z_q\right)\right|^2}{\left|E_0\right|^2}. \tag{2.10}$$

The sum is over all quantum wells inside the gain region, $\left|E\left(z_q\right)\right|^2$ is the E-field upon the q_{th} quantum well and E_0 is the E-field at the surface of the gain chip (in air).

By varying the thickness of the window layer, the gain chip can be grown with an etalon that is somewhere between resonant $(n\lambda/2)$ and anti resonant at the design wavelength $\left(\left(n+\frac{1}{2}\right)\lambda/2\right)$. The E-field within the gain sample can be calculated using the same multilayer technique used to calculate the reflectivity of the DBR, results of this calculation are shown in figures 2.8 and 2.9. To achieve maximum gain, the sample should be resonant with the laser wavelength; in this case the E-field inside of the gain region will have the same magnitude as that incident upon the surface of the chip. However, as can be seen in figure 2.8, a resonant gain region will have a strong filtering effect upon the bandwidth of the laser, with gain decreasing sharply as the wavelength shifts away from the design wavelength λ_0.

In figure 2.9 the E-field has been calculated for an anti resonant gain region. It can be seen that the square modulus of the E-field within the gain region is reduced to nearly half of that incident upon the chip, however the variation of E-field with wavelength near the design wavelength is now much flatter than in the resonant gain region see figure 2.9 b; this will result in a much broader gain spectrum. Since the duration of a passively mode-locked pulse has an inverse dependence upon bandwidth it is important to design the gain chip to give gain over a broad spectral range. To achieve a broad gain spectrum the VECSEL chip used in this work was designed to be anti resonant at 1030 nm. The gain region was also kept short, incorporating only 6 quantum wells, since a short micro cavity has a broader free spectral range.

(a)

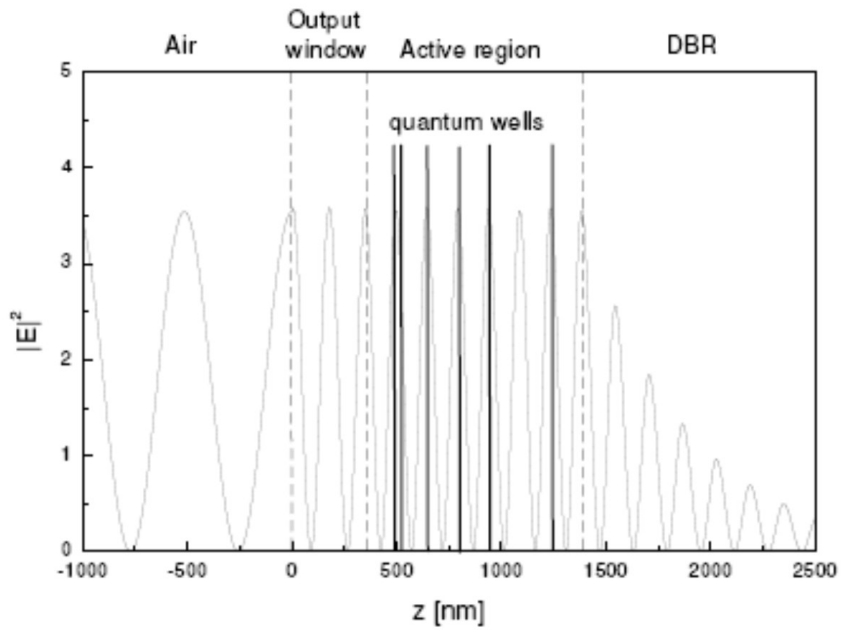

(b)

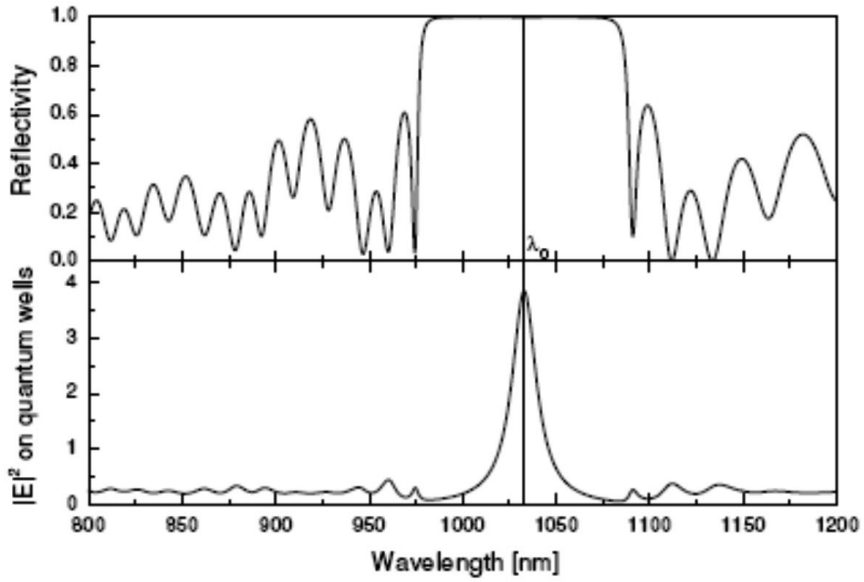

Figure 2.8: (a) Calculated intensity distribution $|E|^2$ at the resonant design wavelength λ, within a resonant gain structure with overall thickness $9\lambda/2$, assuming an incoming wave amplitude of 1. (b) Reflectivity (top) and longitudinal confinement factor (bottom) as a function of wavelength for the resonant cavity. Taken from [6].

(a)

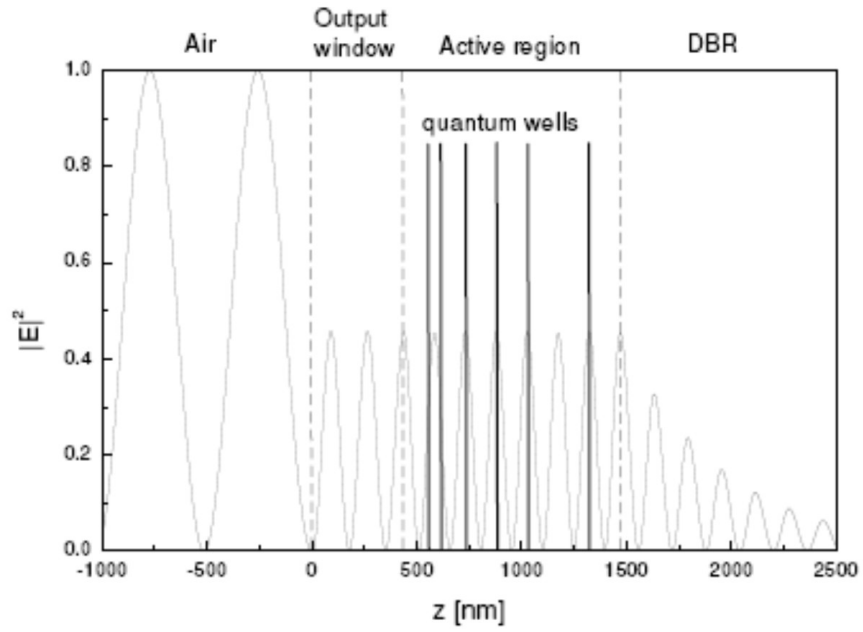

(b)

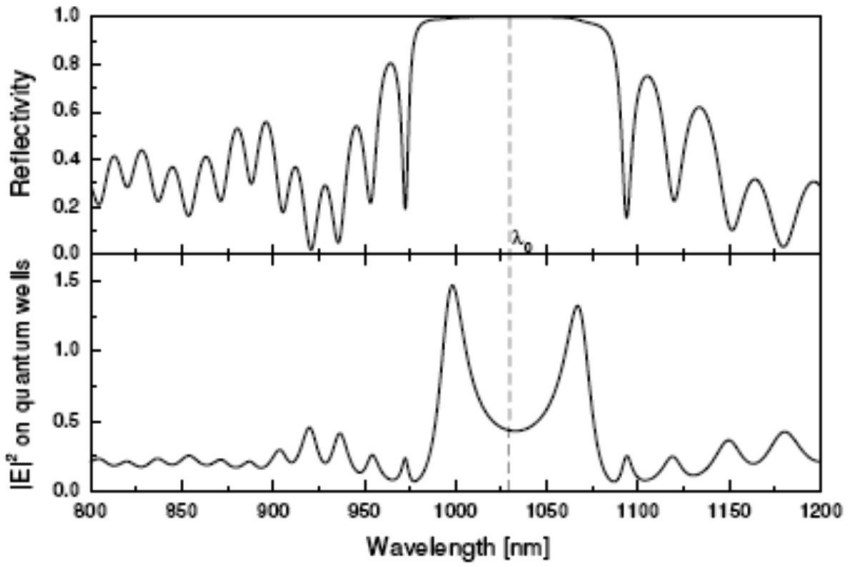

Figure 2.9: (a) Calculated intensity distribution $|E|^2$ at the anti-resonant design wavelength λ, within an anti-resonant gain structure with overall thickness $19\lambda/4$, assuming an incoming wave amplitude of 1. (b) Reflectivity (top) and longitudinal confinement factor (bottom) as a function of wavelength for the resonant cavity.Taken from [6].

2.2 Passive Mode-Locking

By inserting a loss modulator, such as an electro-optic cell into the cavity, it is possible to create a periodic loss inside of the cavity with period equal to the round trip time of the laser. This active mode-locking technique will have the effect of locking the axial modes of the laser in phase creating an ultra short pulse. Active mode-locking requires complicated electronics to modulate the loss at precisely the repetition rate of the cavity, and has the disadvantage that the rate $\mathrm{d}_{loss}/\mathrm{d}t$ tends to be too small to shape the pulse as effectively as other, passive techniques.

Passive mode-locking is an alternative technique that negates the need for electronics. A passive element such as a Kerr medium will introduce an intensity dependent saturable loss into the cavity. An example of a passively mode-locked laser is the Kerr lens mode-locked Ti:sapphire laser. Here a Kerr lens is created within the gain crystal of the laser due to the nonlinear dependence of the crystal refractive index. When an intense electric field is present within the crystal, such as in the case of an ultra short pulse, the Kerr lens will optimise the overlap of cavity mode with the pumped area of the crystal, increasing the gain of the laser over the case where a weaker CW field is incident within the crystal.

Creation of an ultra-short pulse within a passively mode-locked laser can be thought of in the following way. Initially the laser will be oscillating CW with a fixed loss in the cavity. The laser oscillates on more than one axial mode at once, so there will appear random intensity spikes inside of the cavity caused by the relative phase of the axial modes. Passive mode-locking introduces an element into the cavity with a saturable loss, so that a random intensity spike will have sufficient peak intensity to slightly reduce the loss of the cavity; thus any mode that is in phase with the spike will see more gain than the out of phase CW background. Over many cavity roundtrips all the intracavity power will be localised within modes that have a definite phase relation, resulting in an ultra short pulse. At this stage the pulse may still be evolving with its spectral and temporal profile being perturbed by the effects of loss, gain and dispersion from each element within the cavity. Theoretical models describing the steady state of a laser passively mode-locked with a saturable absorber have been developed by Haus [13].

When designing a SESAM for passive mode-locking there are four important parameters to consider. These are: the modulation depth of the SESAM, the saturation

fluence, the nonsaturable loss and the relaxation time of the device; for a review of SESAM designs and structures see [14]. A SESAM is not perfectly reflective, and will introduce two sources of loss into a laser cavity. The first, non saturable loss is caused by defects within the material, resulting in reflectivity $R_{ns} < 100$ %. The second source of loss is engineered by incorporating an absorbing material into the SESAM. In the presence of low fluence light, the absorber results in a SESAM reflectivity $R_{lin} < R_{ns}$. As the fluence of incident light is increased, the reflectivity of the SESAM will increase as the absorbing medium becomes saturated. The modulation depth ΔR of the SESAM is defined as the % change in reflectivity, caused by the saturation of the absorber; the maximum value of δR is given by $R_{ns} - R_{lin}$(unsaturated absorber) The saturation fluence $F_{sat,a}$ of the SESAM is defined as [14]:

$$F_{sat,a} = h\nu/\sigma_A, \tag{2.11}$$

where $h\nu$ is the photon energy and σ_A is the absorption cross section.

Mode-locking may take place in either a slow regime, where the recovery time of the absorber is long compared to the pulse length or in a fast regime, where the absorber recovers on a time comparable to or shorter than the pulse propagating within the laser. In addition to this, there may be a pulse shaping effect from the saturation of the gain. These different regimes of mode-locking are illustrated in figure 2.10.

To obtain short pulses with a SESAM mode-locked laser it is important that the SESAM absorption totally recovers in-between successive roundtrips of the pulse; clearly the shorter the recovery time, then the stronger the pulse shaping from the SESAM will be. The typical interband carrier recovery time of a quantum well structure is around 1 ns. By growing the absorber at a low temperature, defect sites can be introduced into the absorber [15] and the carrier recombination time will be reduced; alternatively defect sites can be created post growth by ion irradiation [16]. However, the nonsaturable loss of the device will rise with increasing number of defect sites making this approach unsuitable for VECSELs, where a low loss of less than 1 % is required.

The SESAM used in this thesis contains a single quantum well grown 2 nm below the surface. This enables tunnelling between surface states allowing for a fast recovery time of less than 21 ps, measured using a streak camera [17]. Since the defects are all located at the surface of the device, the structure can be grown under

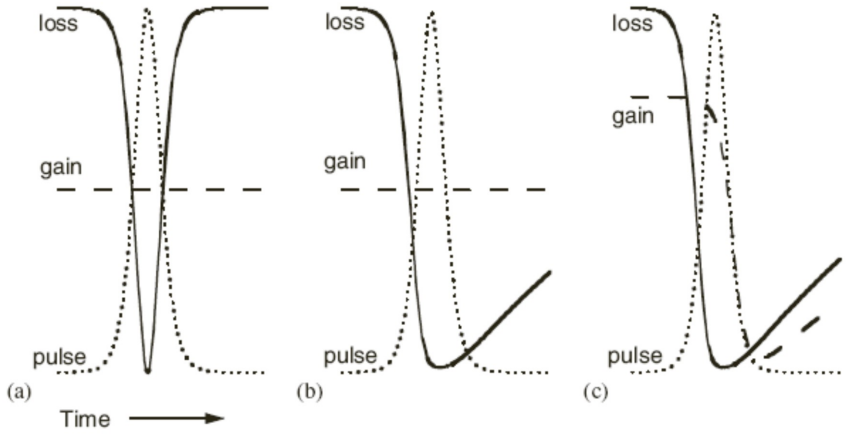

Figure 2.10: Three regimes of passive modelocking: (a) fast saturable absorber opens a short window of net gain, (b) slow saturable absorber opens a long window of net gain, (c) slow saturable absorber combined with dynamic gain saturation opens a short time window of net gain. Taken from [4]

optimal conditions minimising the number of defects and thus the nonsaturable loss; this SESAM will produce pulses with a few picosecond duration, shaped by the slow absorber and gain saturation (pulse regime (c) in figure 2.10).

The modulation depth of a quantum well SESAM depends upon the absorption of quantum wells as does the saturation fluence of the device. The structure of the SESAM is used to control the optical field local to any absorber within the SESAM, enabling for control of the modulation depth of the device. The electric field local to any absorber within the SESAM can be modelled in the same way as has been done with the gain chip used in this thesis [2,6]. It is also possible to calculate the dispersive effect of the multilayer structures; this will be used in a discussion of the measured phase structure of VECSEL pulses, presented in chapter 3. The calculated E-field upon the quantum well of the SESAM used in this work can be seen in figure 2.11, the effect of linear dispersion is also shown by plotting the group delay dispersion of the device (GDD):

$$GDD = \frac{d^2\phi(\omega)}{d\omega^2}. \tag{2.12}$$

where $\phi(\omega)$ is the spectral phase of the pulse and ω is the angular frequency of the pulse.

From figure 2.11 it is estimated that the modulation depth of the SESAM is around 0.3 % and the saturation fluence is $100\ \mu J/cm^2$.

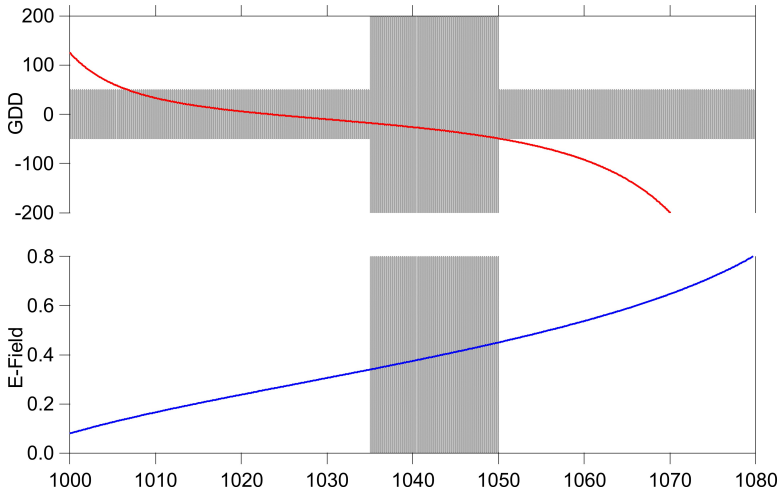

Figure 2.11: Calculated group delay dispersion (measured in $fs^(2)$) and electric field strength upon the quantum well (bottom) for the SESAM used in this thesis. The shaded regions are to indicate the wavelength range over which the VECSEL operates.

For stable mode-locking of a VECSEL the inequality given by equation 2.13 must be satisfied meaning that for a net window of gain to exist the SESAM should saturate before the gain [18]:

$$\frac{E_{sat,a}}{E_{sat,g}} = \frac{F_{sat,a}A_a}{F_{sat,g}A_g} << 1. \tag{2.13}$$

Here, the saturation energy $E_{sat,a/g}$ is given by the saturation fluence of the absorber/gain, multiplied by the cavity mode area $A_{a/g}$ upon the surface of the SESAM/gain chip. Since the absorbing element in both the gain chip and the SESAM is quantum well based it follows that both elements have similar saturation fluences $F_{sat,a} \approx F_{sat,g}$. In order to satisfy the inequality 2.13 it is necessary to design the cavity mode to have a larger area A_g at the surface of the gain chip, than at the surface of the SESAM A_a. Mode-locking is usually achieved with an area ratio A_g/A_a of between 10 and 30. The VECSELs used in this thesis are capable of producing trains of picosecond pulses centred near 1035 nm. However, when sufficient fluence is reached upon the SESAM it is found that the laser will shift to longer wavelengths near 1040 nm, and the pulse duration will drop to around 500 fs. It has been sugested that above a certain fluence the optical Stark effect acts as an aditional pulse shaping mechanism resulting in the observed sub-picosecond pulses [19].

The optical, or ac Stark effect is usualy asociated with atomic systems where an optical field induces a shift in the resonance frequency of the atoms. The strength

of the ac Stark effect depends both upon the detuning of the optical field from the atomic resonance and upon the intensity of the optical field. In semiconductor quantum wells, the ac Stark effect has been observed to cause a blue shift in the absorption frequency of excitons [20]. The ac Stark effect will cause an aditional loss modulation within the VECSEL, provided that the lasers wavelength is on the low energy side of the exciton peak in the SESAMs absorption spectrum. The optical Stark effect responds on a time scale much faster than the duration of the pulses within a VECSEL. This effectively instantaneous response allows for fast SESAM mode-locking and has produced pulses as short as 260 fs [1]. With this design of SESAM, the E-filed at the surface of the device increases with increasing modulation, eventualy leading to damage of the device. A modulation depth of 0.6 % was required to produce the 260 fs pulses.

Since the demonstration of the optical Stark mode-locking mechanism in the surface embedded quantum well [17] it has become possible to create SESAMs with burried quantum wells that have quite fast recovery times [21]; while maintaing a low non-saturable loss. These techniques allow for an increased modulation depth which helps to improve the mode-locking in VECSELs, while keeping the E-field at the surface as low as possible. In [21] fast recovery times were obtained in two different ways, firstly by introducing a strained layer of material between the DBR and the quantum well region; the lattice mismatch gave a recovery time of 4.5 ps. Alternatively intraband scattering into deep quantum wells placed near the shalow quantum wells (absorbing at the laser wavelength) was used to achieve a recovery time of 24 ps. It should also be possible to demonstrate optical Stark mode-locking of a VECSEL with such SESAMs.

2.2.1 Designing the External Cavity

To ensure stable mode-locking the external cavity is designed to satisfy the inequality given in equation 2.13. In addition to this condition, the cavity mode upon the gain chip should be approximately the same area as spot size of the pump source. The standard cavity used in this work is a 1 GHz repetition rate z-cavity, as illustrated in figure 2.1. A 0.7 % output coupler with radius of curvature equal to 50 mm is positioned 48 mm from the gain chip, which acts as a turning mirror. A 25 mm radius of curvature high-reflector is positiond 82 mm away from the gain chip and focuses

the cavity mode onto the SESAM which acts as an end mirror. The cavity has two waists: one is located near to the gain chip and the other is upon the SESAM.

In figure 2.12 the two cavity waists of the standard z-cavity have been plotted as a function of the variable length D, which is simply the separation of the SESAM from the 25 mm high reflector; controllable by a translation stage upon which the SESAM was mounted. By increasing the separation D it is possible to reduce the size of the waist upon the SESAM. Increasing the separation D, will also reduce the size of the waist upon the gain chip affecting the overlap with the pump spot. If the mode area at the surface of the gain chip is changed by more than a few % from that of the pump spot, then the VECSEL will stop lasing; the maximum change is observed to be around 1 %. There is thus a small range of D over which the cavity will be able to lase, indicated by the shaded regions in figure 2.12. This cavity allows for a minimum waist upon the SESAM of aproximately 10 μm.

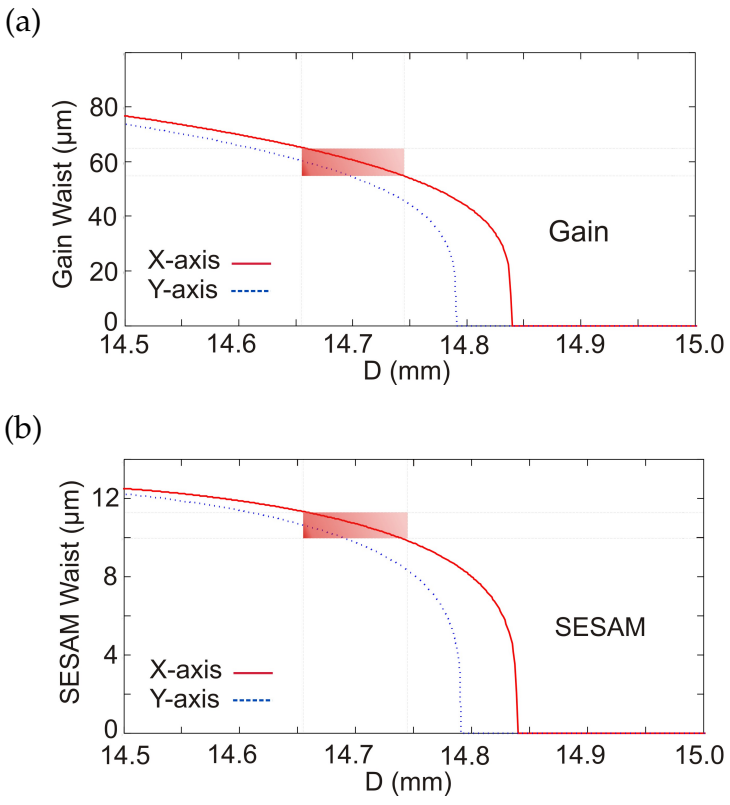

Figure 2.12: Stability curves for the 1 GHz z-cavity: (a) cavity mode at the surface of the gain chip, as a function of the separation D between the SESAM and 25 mm high reflector; (b) cavity waist upon SESAM as a function of D. The shaded areas correspond to the approximate stable operating range of the cavity.

2.3 Sample Characterisation

In this section, results of the optical characterisation of gain sample QT1544 will be presented. The experimental arrangement used to optically characterising a VECSEL gain chip is shown in figure 2.13; this technique has previously been reported by Tropper et al. [6]. In this technique, the photoluminescence (PL) spectrum emitted from the surface (top PL) and from the edge (edge PL) of the gain chip is recorded. The spectrally integrated photoluminescence power can also be recorded for the purpose, of calculating quantum efficiency of the gain chip as reported in [6]; this calculation was not carried out for the lasers used in this thesis and will not be discussed any further.

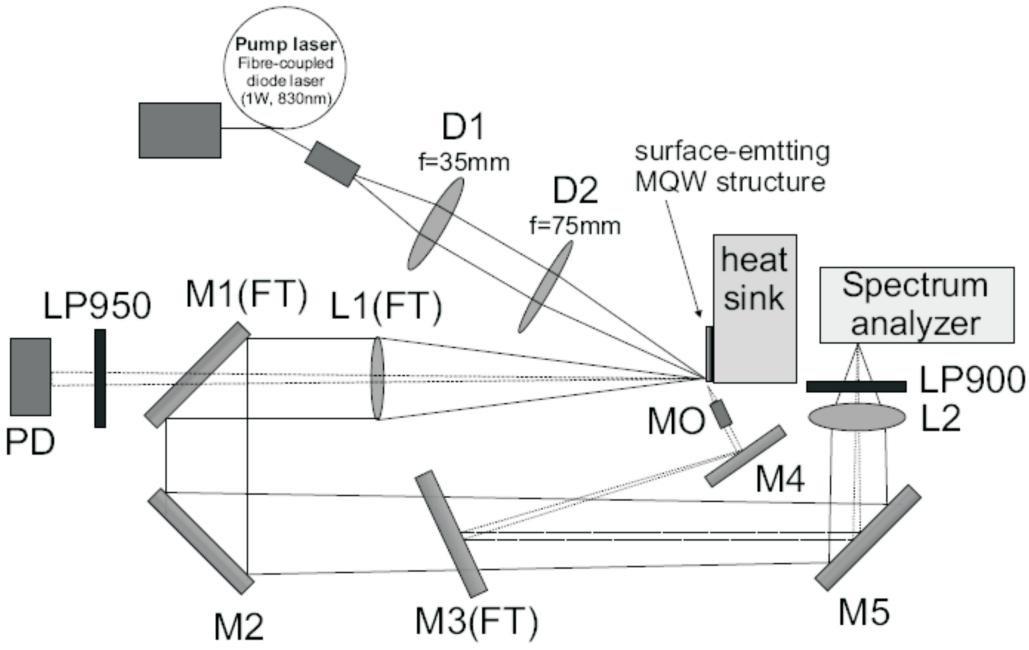

Figure 2.13: Experimental arrangement used to perform the optical characterisation of QT1544, taken from [6].M, mirror; L, lens; D, doublet lens; MO, microscope objective; LP, long pass filter; PD, InGaAs photodiode; FT, flip-top component.

The arrangement of figure 2.13 allowed for the spectrally integrated PL power, top and edge PL to be recorded in quick succession, all from the same location upon the gain chip. The optically pumped quantum wells emit radiation into a solid angle of 4π steradians. The lens, L1 and the microscope objective (MO) sample small portions of the top and edge PL, respectively; the flip top mirror (M3) allowed for the input to a grating spectrometer to be switched between the top and edge PL. To take these

measurements, the wafer was first cleaved into small chips of approximately 5 mm by 5 mm. The chip was bonded to a copper heat-sink; the heat sink was temperature controlled by a Peltier. PL measurements were carried out by optically pumping the chip with an 830 nm laser diode emitting up to 1 W in a 60 μm radius spot upon the gain chip.

A selection of top and edge PL are shown in figure 2.14. The PL spectra were recorded at different pump powers and heat sink temperatures, as indicated in figure 2.14; all the PL spectra were recorded from the same location on the gain chip. To ensure that the edge PL only show the intrinsic spectral emission from the quantum wells, it was necessary to rotate the MO through small angles (about 10°) behind the plane of the gain chip, and off axis from any emission that was wave-guided by the VECSEL micro cavity. The edge PL (figure 2.14 a) show a strong photoluminescence peak centred at about 1030 nm. This peak corresponds to the radiative recombination of electrons in the conduction band with holes in the valence band. A small emission peak around 985 nm indicates radiative recombination of carriers within the GaAs barriers, the peak height is approximately 5% of the 1030 nm (quantum well) emission peak. Finally there is a peak centred around 830 nm which is caused by scattered pump light.

As the pump power is increased, the integrated PL power increases, the spectral bandwidth increases as the band states fill and the quantum well emission peak (close to 1030 nm) moves towards longer wavelengths. At a given pump power the increasing heat sink temperature causes, the integrated PL power to fall, the spectral width becomes broader and the peak at 1030 nm shifts towards longer wavelengths. This shift towards longer wavelength can be attributed to the thermal expansion of the lattice and to a reduction in the strength of interaction that causes the bandgap [6].

The photoluminescence spectra, from the top surface of the gain chip are shown in figure 2.14. These spectra are strongly modulated by the interference within the multilayer. There is a broad intensity peak near 1010 nm caused by electron hole recombination in the well; this peak is strongly filtered by the etalon effect of the gain structure. At shorter wavelengths ($\lambda < 980$ nm) a series of peaks appear in the spectrum. These peaks are caused by side lobes in the reflectivity of the DBR spectrum outside the stop-band, see figure 2.5. There is again a peak close to 830 nm which is caused by scattered pump light.

(a)

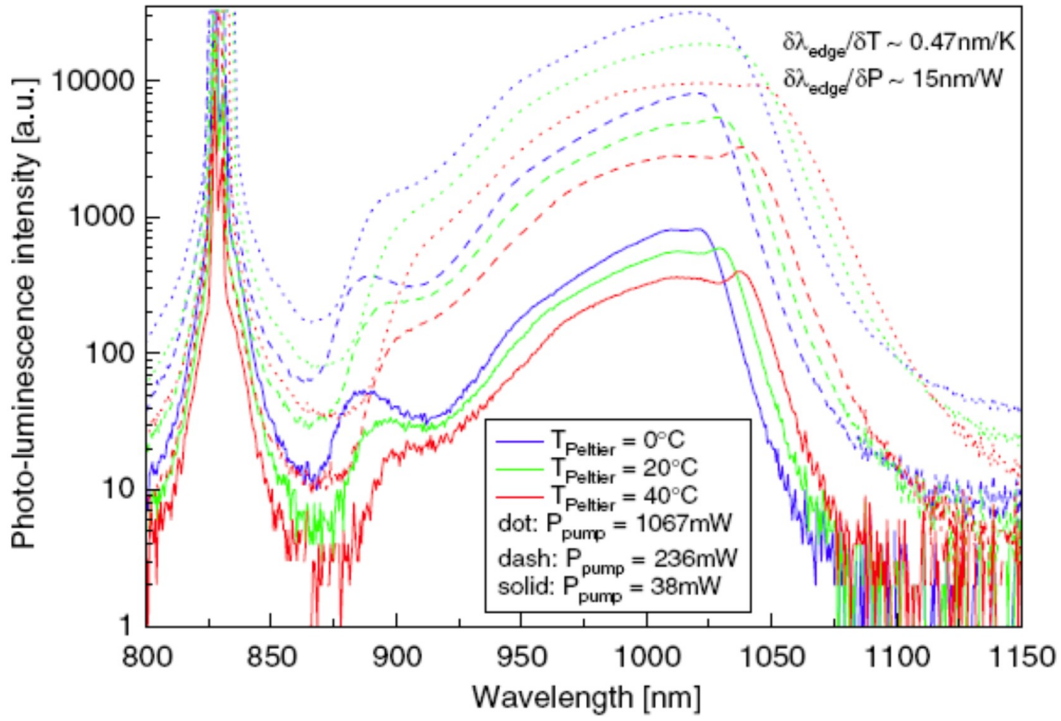

(b)

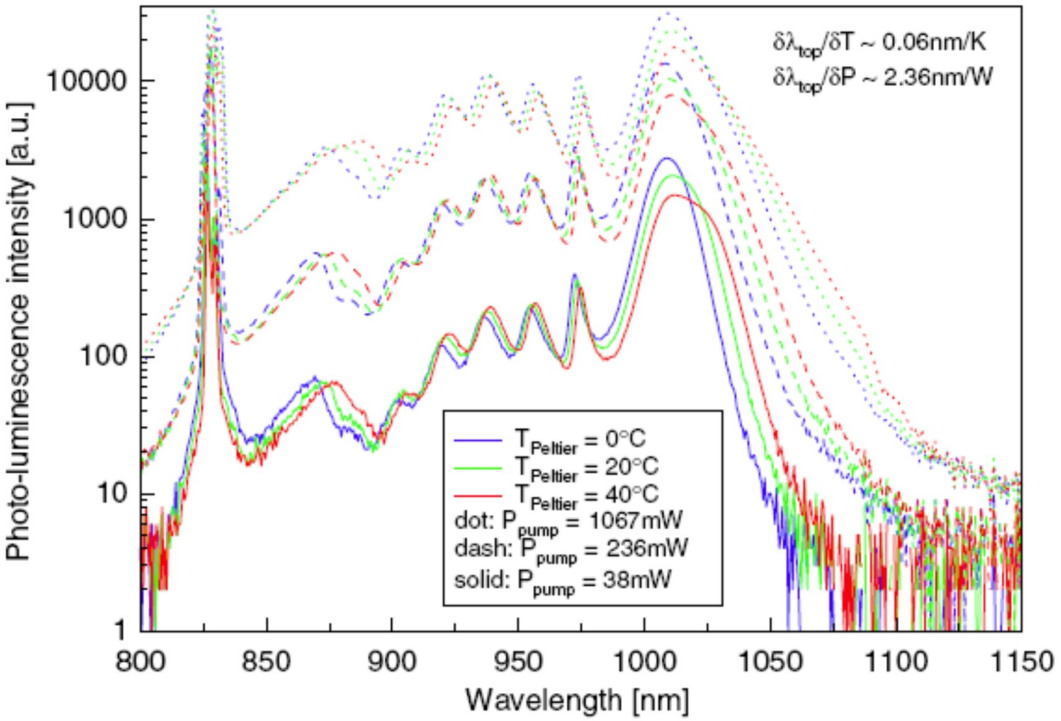

Figure 2.14: (a) Edge photoluminescence (PL) from QT1544, (b) top PL recorded at 3 different temperatures and pump powers as indicated in the figures. Taken from [6].

From these measurements the change in wavelength, of both the edge and the top PL, can be calculated with respect to a change, in either the pump power or heat sink temperature. These spectral shifts with increasing temperature (pump power) have been calculated for the data presented in figure 2.14 and are listed below [6]:

$$\frac{d\lambda_{edge}}{dT} = 0.47\ nmK^{-1}, \qquad \frac{d\lambda_{edge}}{dP} = 15\ nmW^{-1}, \tag{2.14}$$

$$\frac{d\lambda_{top}}{dT} = 0.06\ nmK^{-1}, \qquad \frac{d\lambda_{edge}}{dP} = 2.36\ nmW^{-1}. \tag{2.15}$$

The important thing to note is that the edge PL changes more rapidly with increasing temperature and power than the top PL. To achieve maximum efficiency the different rates of change should be taken into account when designing the sample, so that the peak in the edge PL spectra coincides with that of the edge PL at the operating temperature expected under intense pumping (1 - 1.5 W for QT1544).

In addition to the photoluminescence measurements, the reflectivity of the gain chip may also be recorded. When a newly grown gain sample is first being tested, it is useful to compare the measured reflectivity spectrum with the reflectivity obtained from a multilayer calculation. For comparison the measured (solid line) and calculated (dotted line) reflectivity for waffer QT1544 is plotted in figure 2.15. Each spectrum shows, an approximately 100 nm stop band centred near the design wavelength of 1030 nm; this indicates that the DBR and micro cavity thickness have been grown as specified. The dip in the measured spectrum, near 1020 nm, is caused by absorption in the quantum wells.

Finaly the gain chip is placed into an external cavity to form a laser. Many of the results reported in this thesis were taken using VECSELs operating at 1 GHz repetition rates, figure 2.1. The construction of such a laser has been described in section 2.2.1, where, to achieve CW lasing it is necessary to replace the SESAM with a flat high reflector. In such a z-cavity, and with 0.7 % output coupling, the gain chips used in this thesis had a laser threshold of around 200 mW. When pumped with 1.3 W, focussed to a 60 μm radius spot, the average CW power of the VECSEL was around 140 mW with centre wavelength near 1035 nm. Typically, the centre wavelength of the VECSEL could be temperature tuned over the range 1020 nm - 1050 nm. A selection of CW and modelocked spectra are presented in figure 2.16 along with a typical power transfer curve. The mdoe-locked characteristics of the VECSEL will be described in more detail throughout the later chapters of this thesis,

for now it shall be noted that the modelocked VECSELs presented within this thesis typicaly produced pulses of duration 1 ps - 450 fs with avearge powers in the range 10 - 40 mW.

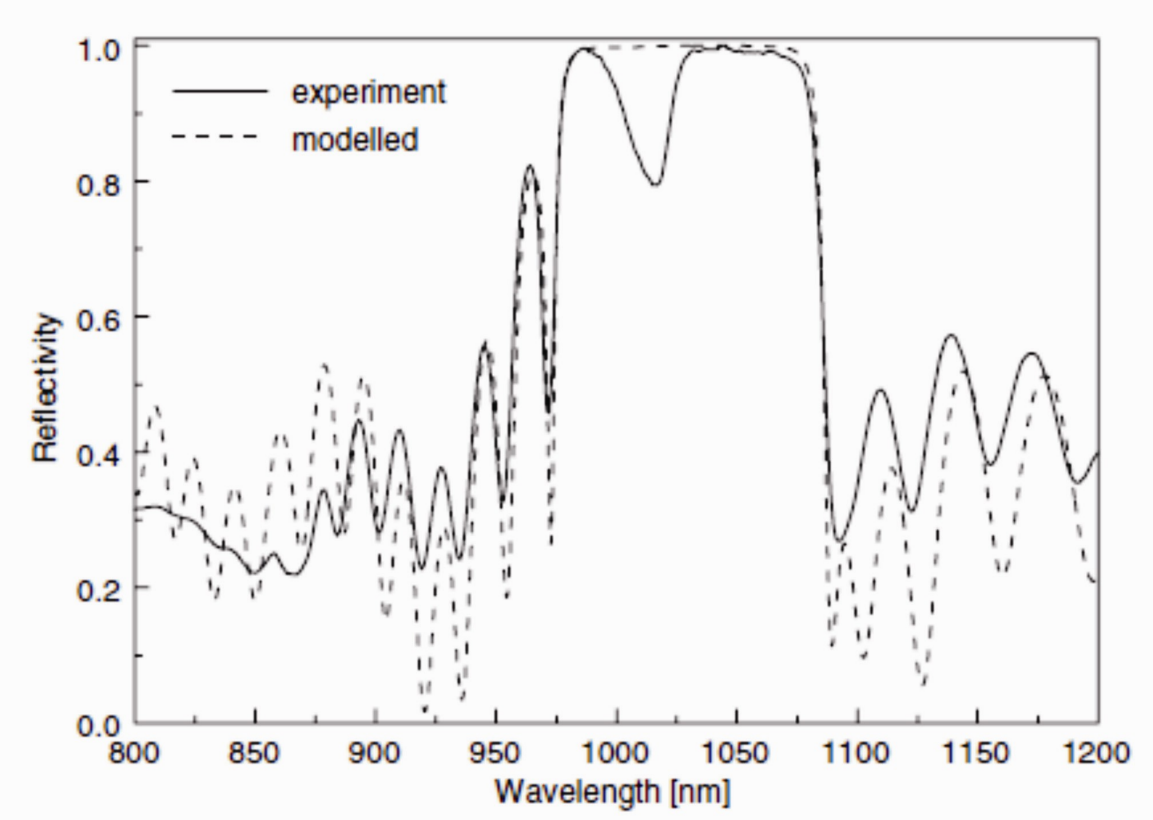

Figure 2.15: Measured reflectivity spectrum recorded for gain wafer QT1544 (solid line); reflectivy spectrum obtained for QT1544 design, using a multilayer calculation (dotted line) taken from [6]. The multilayer calculation fails to acurately model the modulations in the measured spectrum. This can be attributed to the inacurate, specification of refractive index away from the design wavelength of the DBR.

When a newly grown gain waffer is first tested, the characterisation techniques presented in section 2.3 are used to infer the reliability of the epitaxial growth. It should be noted that even when the reflectivity and PL measurements indicate a succesful growth, there may still be differences between the design, of the structure, and the real device. For example, the location of the quantum wells within the gain chip remains an unknown after these characterisation techniques. To achieve mode locking with the Stark SESAMs used in this thesis, it was observed that the VECSEL should, in CW operation, be temperature tunable over the range 1030 nm - 1045 nm, with an average power of at least 100 mW.

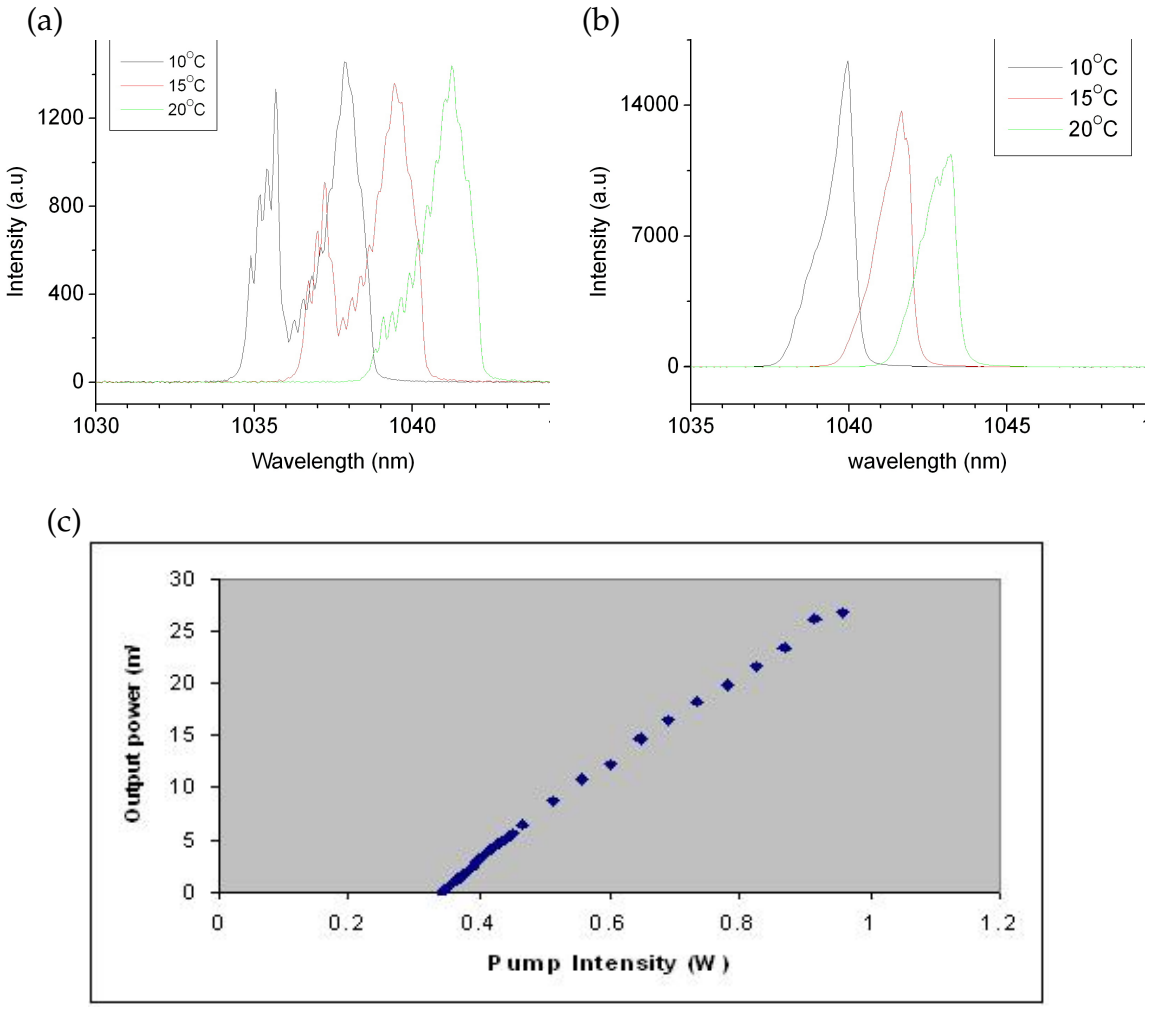

Figure 2.16: a) CW spectra recorded at various temperatures, b) mode-locked spectra recorded at the temperatures recorded in the figuree, c) power transfer curve recorded for a CW VECSEL.

2.4 References

[1] K. G. Wilcox, Z. Mihoubi, G. J. Daniell, S. Elsmere, A. Quarterman, I. Farrer, D. A. Ritchie, and A. Tropper. "Ultrafast optical Stark mode-locked semiconductor laser". *Optics Letters*, 33(23):2797–9, 2008.

[2] S. Hoogland. *Optically Pumped Vertical-External-Cavity Surface-Emitting Semiconductor Lasers*. PhD thesis, University of Southampton, 2003.

[3] S. Elliott. *The Physics and Chemistry of Solids*. Wiley, 2002.

[4] Ursula Keller and Anne C. Tropper. "Passively modelocked surface-emitting semiconductor lasers". *Physics Reports*, 429(2):67–120, 2006.

[5] W Chow, W and W. Koch, S. *Semiconductor Laser Fundamentals*. Springer, 2000.

[6] A. C. Tropper and S. Hoogland. "Extended cavity surface-emitting semiconductor lasers". *Progress in Quantum Electronics*, 30(1):1–43, 2006.

[7] T. Schibli, K. Minoshima, H. Kataura, E. Itoga, N. Minami, S. Kazaoui, K. Miyashita, M. Tokumoto, and Y. Sakakibara. "Ultrashort pulse-generation by saturable absorber mirrors based on polymer-embedded carbon nanotubes". *Opt. Express*, 13(20):8025–8031, 2005.

[8] M. Rahim, M. Arnold, F. Felder, K. Behfar, and H. Zogg. "Midinfrared lead-chalcogenide vertical external cavity surface emitting laser with 5 mu m wavelength". *Applied Physics Letters*, 91(15):151102–3, 2007.

[9] S. Hoogland, S. Dhanjal, A. C. Tropper, J. S. Roberts, R. Haring, R. Paschotta, F. Morier-Genoud, and U. Keller. "Passively mode-locked diode-pumped surface-emitting semiconductor laser". *Photonics Technology Letters, IEEE*, 12(9):1135–1137, 2000.

[10] M. Hoffmann, Y. Barbarin, D. Maas, M. Golling, I. Krestnikov, S. Mikhrin, A. Kovsh, T. Sdmeyer, and U. Keller. "Modelocked quantum dot vertical external cavity surface emitting laser". *Applied Physics B: Lasers and Optics*, 93(4):733–736, 2008.

[11] L. A. Coldren and S. W. Corzine. *Diode Lasers and Photonic Integrated Circuits*.

[12] L. A. Coldren and S. W. Corzine. *Diode Lasers and Photonic Integrated Circuits*. Wiley, 1995.

[13] H. A. Haus. "Mode-locking of lasers". *IEEE Journal of Selected Topics in Quantum Electronics*, 6(6):1173–85, 2000.

[14] U. Keller, K. J. Weingarten, F. X. Kartner, D. Kopf, B. Braun, I. D. Jung, R. Fluck, C. Honninger, N. Matuschek, and J. Aus der Au. "Semiconductor saturable absorber mirrors (SESAM's) for femtosecond to nanosecond pulse generation in solid-state lasers". *Selected Topics in Quantum Electronics, IEEE Journal of*, 2(3):435–453, 1996.

[15] S. Gupta, J. F. Whitaker, and G. A. Mourou. "Ultrafast carrier dynamics in III-V semiconductors grown by molecular-beam epitaxy at very low substrate temperatures". *IEEE Journal of Quantum Electronics*, 28(10):2464–72, 1992.

[16] E. Lugagne Delpon, J. L. Oudar, N. Bouche, R. Raj, A. Shen, N. Stelmakh, and J. M. Lourtioz. "Ultrafast excitonic saturable absorption in ion-implanted InGaAs/InAlAs multiple quantum wells". *Applied Physics Letters*, 72(7):759–761, 1998.

[17] A. Garnache, S. Hoogland, A. C. Tropper, I. Sagnes, G. Saint-Girons, and J. S. Roberts. "Sub-500-fs soliton-like pulse in a passively mode-locked broadband surface-emitting laser with 100 mW average power". *Applied Physics Letters*, 80(21):3892–3894, 2002.

[18] D. Lorenser, H. J. Unold, D. J. H. C. Maas, A. Aschwanden, R. Grange, R. Paschotta, D. Ebling, E. Gini, and U. Keller. "Towards wafer-scale integration of high repetition rate passively mode-locked surface-emitting semiconductor lasers". *Applied Physics B: Lasers and Optics*, 79(8):927–932, 2004.

[19] G. J. Daniell, Z. Mihoubi, K. G. Wilcox, and A. C. Tropper. "Numerical model of the optical stark effect as a mode-locking mechanism for femtosecond vertical-external-cavity surface-emitting semiconductor lasers". 2008 Conference on Lasers and Electro-Optics (CLEO), page 2 pp., Piscataway, NJ, USA, 2008. IEEE.

[20] A. Mysyrowicz, D. Hulin, A. Antonetti, A. Migus, W. T. Masselink, and H. Morko. "Dressed Excitons in a Multiple-Quantum-Well Structure: Evidence

for an Optical Stark Effect with Femtosecond Response Time". *Physical Review Letters*, 56(25):2748, 1986.

[21] S. Suomalainen, M. Guina, T. Hakulinen, R. Koskinen, J. Paajaste, M. Karjalainen, M. Saarinen, S. Marcinkevicius, and O. G. Okhotnikov. "Semiconductor saturable absorbers with recovery time controlled by lattice mismatch and band-gap engineering". *Materials Science and amp; Engineering: B (Advanced Functional Solid-State Materials)*, 147(2-3):156–60, 2008.

Chapter 3

Measuring the Phase Structure of VECSEL Pulses Using Frequency Resolved Optical Gating

It was observed that the VECSELs used in this thesis, capable of producing 500 fs transform limited pulses, would also produce chirped pulses which could be greater than 1.5 times transform limited and still be close to 500 fs in duration. It is the purpose of this chapter to investigate the underlying phase structure responsible for these non-transform limited pulses.

3.1 The Time-Bandwidth Product of VECSEL Pulses

The output from a mode-locked VECSEL is typically characterised by two measurements, an intensity autocorrelation and an optical spectrum of the pulse train. From these measurements the temporal duration and the bandwidth of the pulse can be determined. The complex electric field of an ultra-short pulse is a linear superposition of monochromatic waves that can be expressed in the time domain as:

$$E(t) = \frac{1}{2}A(t)e^{i(\phi_0+\omega_0 t+\phi_a(t))}. \tag{3.1}$$

The electric field may also be expressed in the frequency domain as:

$$\tilde{E}(\omega) = \sqrt{\frac{\pi}{\epsilon_0 cn}I(\omega)}e^{-i\phi(\omega)}, \tag{3.2}$$

where the time and frequency domains are related by the Fourier transforms:

$$E(t) = \frac{1}{2\pi} \int \tilde{E}(\omega) e^{i\omega t} d\omega, \tag{3.3}$$

$$\tilde{E}(\omega) = \int E(t) e^{-i\omega t} dt. \tag{3.4}$$

The term I(ω) in equation 3.2 is the spectral intensity, it is proportional to the power spectrum density the quantity measured by a spectrometer. The intensity autocorrelation will give a measure proportional to A^2(t). The spectrum and autocorrelation combined can be used to indicate the existence of a non-zero phase term in the complex electric field of the pulse by calculating the time-bandwidth product

$$\Delta\tau\Delta\nu. \tag{3.5}$$

Fourier theory states that the time-bandwidth product of a pulsed signal is constrained by the uncertainty principle, see Siegman page 334 [1]. This quantity will have a minimum value depending upon pulse shape and how $\Delta\tau$ and $\Delta\nu$ are defined. If $\Delta\tau$ is the FWHM pulse length measured in seconds and $\Delta\nu$ is the FWHM bandwidth of the pulse measured in Hz then the time-bandwidth product will be 0.441 for a Gaussian pulse and 0.315 for a $sech^2$. This minimum value is only achievable when there is no significant phase structure to the pulse, that is to say that ϕ_a(t) depends only linearly upon time.

In fig 3.1 the square modulus of the E-field is plotted for a Gaussian pulse in the time and frequency domains. These quantities are proportional to the autocorrelation and spectrum of an ultra short pulse, (a) is a transform limited pulse; (b) the same pulse length as in (a) with a quadratic variation in ϕ_a(t) known as a linear chirp.

The presence of the linear frequency chirp is indicated by an increase in the bandwidth of the pulse compared to that of the transform limited pulse of the same temporal duration.

A typical VECSEL/SESAM combination will be able to produce pulses of some minimum temporal duration, namely around 500 fs for QT1544/QT1627. It is possible to maintain this minimum pulse length for a variety of bandwidths with the time-bandwidth product being as much as two times the transform limit. There is not enough information in the spectrum and autocorrelation to know the nature of the underlying phase structure; the chirp could be linear or of higher order. If the

(a)

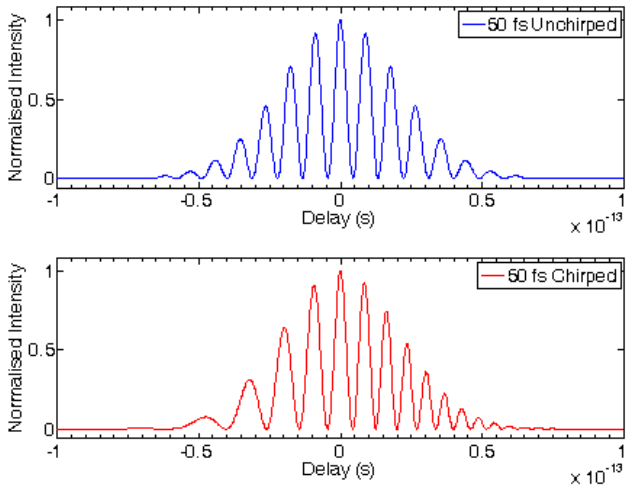

(b)

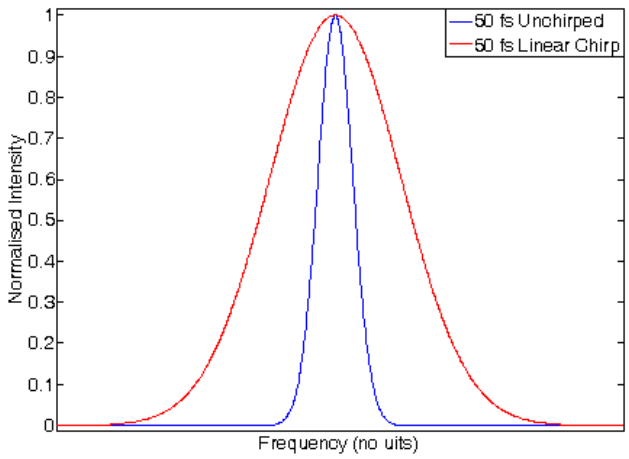

Figure 3.1: (a) Temporal profile of a chirped and un-chirped 50 fs pulse,(b) Fourier transform of the 50 fs chirped pulses in (a).

nature of the phase structure is known, then it becomes possible to compress the pulse in time by passing the pulse through a material system that applies a chirp of opposite sign to that of the pulse. A 500 fs pulse that is 2 times transform limited with a linear frequency chirp could be compressed down to 250 fs, for example by using a grating compressor or photonic crystal fibre [2]. However, for more complicated phase structures there is no easy way of compensating for the chirp. It is the aim of this chapter to describe an existing technique for measuring the phase structure of ultra-short pulses. The first results of measurements of the phase structure of VECSEL pulses are presented; they show the chirp to vary quadratically with time.

3.2 Frequency Resolved Optical Gating

The technique of frequency resolved optical gating (FROG), introduced by D. J. Kane and R. Trebino, overcomes many of the limitations of the intensity autocorrelation [3–5]. FROG enables the complete retrieval of the pulse intensity and phase from an experimentally recorded trace. In figure 3.2 a block diagram of a FROG experiment is shown.

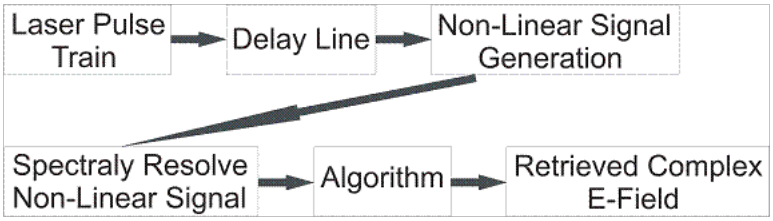

Figure 3.2: Block diagram of an experimental FROG measurement.

The FROG trace is an autocorrelation type measurement. The beam to be characterised is first split into two components. Then after a variable delay, the two beam components are overlapped inside an instantaneously responding nonlinear medium such as a BBO crystal. The resulting nonlinear signal is then spectrally resolved and recorded as a function of delay, producing a spectrogram, from which the complex electric field of the pulse can be retrieved. If second harmonic generation is used then the non-linear signal will be of the form [6]:

$$E_{sig}(t,\tau) = E(t)E(t-\tau), \tag{3.6}$$

where τ is the delay between the two components of a single pulse. The resulting FROG trace is a spectrogram or 2D plot of the form [6]

$$I_{FROG}(\omega,\tau) = \left| \int_{-\infty}^{+\infty} dt E_{sig}(t,\tau) exp\left(i\omega/t\right) \right|^2. \tag{3.7}$$

The complex electric field is retrieved from the spectrogram using an iterative phase retrieval algorithm [6]. The algorithm employs a technique known as generalized projection to select a signal field $E_{sig}(t,\tau)$ that satisfies two constraints given by equation 3.6 and equation 3.7. The first constraint, states that the signal field retrieved by the FROG algorithm must match the result of inputting the real E-field into equation 3.6 end. The second constraint, is that the result of inputting the retrieved

signal field into equation 3.7 must accurately recreate the measured spectrogram of the pulse.

FROG is able to completely retrieve the complex electric field of an ultra short pulse except for a few minor ambiguities which will be discussed below. Two quantities of interest when describing the phase structure of an ultra short pulse are the instantaneous frequency:

$$\omega(t) = \omega_0 + \frac{d\phi_a(t)}{dt}, \tag{3.8}$$

and group delay

$$T_g(\omega) = \frac{d\phi(\omega)}{d\omega}. \tag{3.9}$$

In equation 3.8 the instantaneous frequency is given by the derivative of the temporal phase and is expressed as the sum of the carrier frequency ω_0 and the derivative of phase with time, referred to as the chirp. A linear increase of frequency with time is called a linear up-chirp and a decrease of frequency with time is called a down-chirp. The group delay describes the relative delay of a spectral component. The spectral phase can often be approximated by a parabolic function and $\phi(\omega)$ may then be expanded into a Taylor series [7]:

$$\phi(\omega_0) + \phi'(\omega_0)(\omega - \omega_0) + \frac{1}{2}\phi''(\omega_0)(\omega - \omega_0)^2 + \frac{1}{6}\phi'''(\omega_0)(\omega - \omega_0)^3 \ldots \tag{3.10}$$

Where ω_0 is the centre or carrier frequency of the pulse. The zeroth order term $\phi(\omega_0)$ is called the absolute phase (or carrier envelope phase) of the pulse, corresponding to the difference in phase between carrier wave and envelope of the pulse. The first order component describes a translation in time of the whole pulse with respect to the rest of the pulse train. The FROG technique is insensitive to both zeroth and first order effects. The higher order terms in equation 3.10 are responsible for changes in the real electric field of the pulse with time, and are measured by FROG. For example, the second order term relates to a linear chirp of the pulse, while the third order term gives the third order dispersion (TOD).

As the SHG FROG trace is symmetrical about the time axis, there exists a temporal ambiguity in the retrieved pulse. This means that it is impossible to know the sign of any phase distortion that is an even function of time, so the linear chirp will have an ambiguous sign. It is also impossible to know the sign of any distortion in the frequency domain. In addition to this ambiguity, FROG is unable to measure the carrier envelope phase of the pulse.

3.3 Experimental Considerations

The FROG arrangement used to measure the pulses from a VECSEL is shown in figure 3.3. As the pulse energy from a VECSEL is very low, typically around 5 nJ, second harmonic generation (SHG) in a BBO crystal was chosen to generate the nonlinear signal; this technique is referred to as SHG-FROG [6]. SHG-FROG is more sensitive to low energy pulses, of the type typically generated by a VECSEL, providing a greater signal than any other nonlinearity used by the FROG technique.

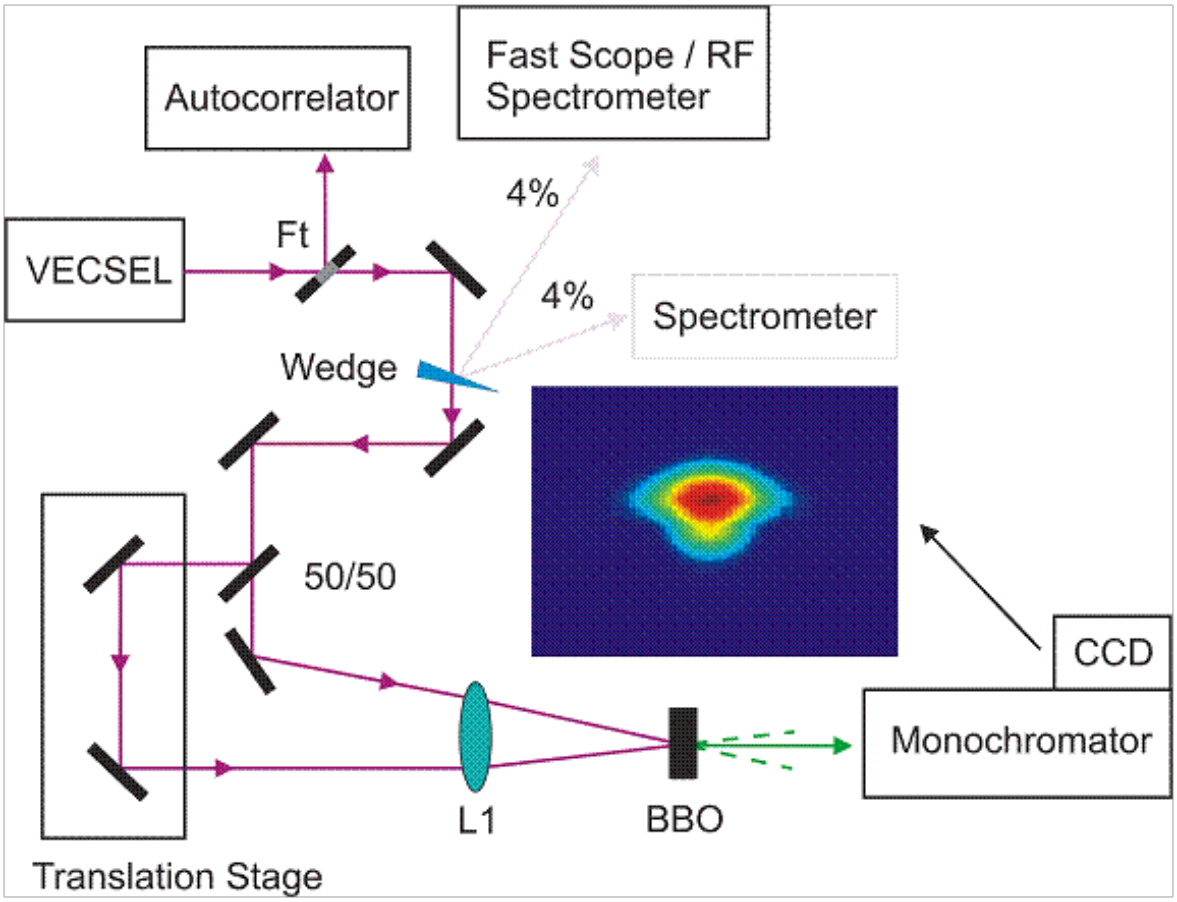

Figure 3.3: Experimental FROG configuration; output from the VECSEL characterized before and after FROG measurements by taking SHG autocorrelation and spectrum. Partial reflections from a glass wedge enabled the optical spectrum and RF spectrum (or fast scope trace) to be observed during a FROG measurement. FT = flip top mirror, L1 = 10 cm focal length lens; a 300 m thick BBO crystal cut for non-collinear SHG with a 15 degree full angle between incident beams was used to produce the FROG signal.

Two beam paths of approximately the same length were defined by splitting the output from the VECSEL into two using a 50/50 beam splitter. One of the beam paths contained two mirrors mounted upon a computer controlled translation stage; this provided a variable delay between pulses in each of the beam paths. After the variable delay was applied the two halves of the VECSEL output were brought to a focus and recombined non-co-linearly inside of a BBO crystal; the full angle between the two beams was less than 15 degrees. A 300 μm crystal was used for the FROG set up since one was made available by canobolising a homemade autocorelator. It should be noted that a slightly thicker crystal could have been used providing that the nonlinear conversion efficeincy did not exceed about 3 % [6] and the phase matching condition could still be maintained [8]. The second harmonic signal from the crossed beams was collimated and focused into a home made spectrometer consisting of a monochromator and CCD camera.

Light from the BBO crystal enters the monochromator through a micrometer controlled entrance slit. This light is reflected from a mirror, positioned approximately 1 m away from the entrance slit. The reflected light is brought incident upon a diffraction grating, positioned to the left of the entrance slit, 1 m away from the first mirror. The diffraction grating has a total of 1.2×10^5 lines across it's 10 cm surface (12000/mm). Light reflected from the diffraction grating obeys the grating equation [9]

$$a\ \sin(\theta_m - \theta_i) = m\lambda \tag{3.11}$$

Where: a is the grating period ($1/12\times10^6$), λ is the wavelength of the light, m is the diffraction order and $\theta_{m/i}$ is the reflection/incident angle with respect to a line drawn normal to the surface of the grating; the subscript m relates to the order of the diffracted light. Light is reflected from the diffraction grating towards a second mirror. This mirror is positioned on the left hand side of the first mirror, and guides the incident light towards the exit slit of the monochromator. The wavelength of light that reaches the exit slit is controlled by the angle $\theta_m - \theta_i$. The diffraction grating is mounted, on a, motor controlled, rotation stage. This enables for control of the angle $\theta_m - \theta_i$ and thus the wavelength of light that reaches the exit slit.

To convert the monochromator into a spectrometer, the exit slit was removed and replaced with a linear CCD array. The CCD had 3000 pixels, aligned in the horizontal plane, so that the entire second harmonic spectrum would be incident upon some

part of the array after reflection from the diffraction grating. The resolving power of a spectrometer is given by the equation [9]

$$\text{Resolving power} = \frac{\Delta\lambda}{\Delta\lambda_{min}} = mN. \tag{3.12}$$

In the previous equation λ is the average wavelength, m is the diffraction order (equal to 1 for this spectrometer), N is the total number of lines on the grating and $\Delta\lambda_{min}$ is the minimum separation after which two separate wavelengths become irresolvable. To obtain the maximum resolution from the spectrometer, the light diverging from the entrance slit, must fill the diffraction grating in the horizontal plane. The resolution of the spectrometer was calculated using equation 3.3 to be 0.004 nm over an 18 nm window. The centre wavelength of this window could be set to any wavelength, in the visible, by rotating the diffraction grating within the horizontal plane.

In practice the density of pixels upon the CCD was found to limit the spectrometer resolution. The 18 nm spectral window of the spectrometer made it possible to simultaneously observe certain pairs of spectral lines, such as the 514.5 nm and 528.7 nm, generated by an argon ion laser. From these observations of the argon ion spectrum it was deduced that the CCD pixel spacing corresponded to a 0.006 nm wavelength separation.

In order to record the FROG trace, the delay stage was first manually adjusted to find zero delay between the two beam paths (maximum second harmonic signal), then the stage was translated past zero delay until the second harmonic signal had disappeared. The stage was then translated back through zero delay by the computer in a number of steps (64, 128, 256 etc), the step size being adjusted so that the stage would go completely through zero delay and to a region where the two pulses no longer overlapped (no second harmonic signal). In-between each step the computer would record a spectrum of the second harmonic signal.

There are many things that can reduce the accuracy of the pulse retrieved by the algorithm. Delong et al. have described a set of conditions for maximising the accuracy of SHG FROG [6], the basic requirement being to maintain the relationship that the signal is linear with the square of the input field:

$$E_{sig}(t,\tau) = E(t)E(t-\tau). \tag{3.13}$$

If the electric field is too high upon the nonlinear crystal then there will be a situation

where the SHG process is efficient enough to deplete the pump, and the SHG signal will no longer be linear with square of the input field. To maintain the relationship of equation 3.13 to within one percent it is necessary to limit the peak intensity conversion efficiency of SHG to a maximum of 3 %. Due to the low average power of the VECSELs used in these experiments this condition is always met.

There is a mismatch between the group velocities of the fundamental v_g^{fund} and second-harmonic v_g^{SHG} beams within the doubling crystal. This mismatch acts as a frequency dependent filter of the form [6]

$$F(\omega) = \left[\frac{sin\left(\frac{t_\omega \omega}{2}\right)}{\left(\frac{t_\omega \omega}{2}\right)}\right]^2, \tag{3.14}$$

$$\text{where} \qquad t_\omega = \left(\frac{1}{v_g^{SHG}} - \frac{1}{v_g^{fund}}\right) L. \tag{3.15}$$

The filter multiplies the generated SHG signal spectrum reducing the bandwidth of the pulse retrieved by the algorithm. This effect can also distort the phase of the retrieved pulse. The group velocity mismatch becomes more critical as the bandwidth of the pulse increases. To reduce this effect to less than a 10 % reduction in the retrieved spectral bandwidth, Delong et al. require that the half-width at half-maximum of the spectral filter F(ω) be larger that 1.4 times the half-width at half-maximum of the SHG signal. For a 300 μm thick BBO crystal this condition is always met with the pulses typically produced by a VECSEL.

The next potential source of error is associated with recording the set of second harmonic spectra that make up the FROG trace. An ultra short pulse is considered properly sampled when all the data points with intensity greater than 10^{-4} of the peak intensity of the pulse appear within the FROG trace surrounded by points of zero intensity/noise. A data set thus sampled will contain full phase and intensity information of the pulse [9]. To achieve this, the correct step size must be chosen for each measurement; this will vary depending upon pulse length and total number of data points recorded.

The temporal step size must be large enough to fully sample the pulse in the time domain, that is

$$N\delta_t \geq \Delta\tau_s. \tag{3.16}$$

The parameter N in equation 3.16 is the total number of steps (16, 32, 64...etc) and

$\Delta\tau_s$ is the full width of the pulse at 10^{-4} of peak intensity. The FROG alogorithm requires that the number of steps in the time domain be equal to the number of steps in the frequency domain, taht is the spectrogram must be a N×N matrix of points. Since the temporal width and spectral bandwidth of the pulse are inversely related it is possible to choose a temporal step $\Delta\tau_s$ that is so large as to cause a cropping of the pulse in the frequency domain, that is the spectral width $N\Delta\lambda$ will be smaller that the full width of the real spectrum. To avoid cropping in the frequency domain, for a Gaussian pulse measured with polarizsation gating FROG, DeLong et al. require that [10]

$$\delta_t \leq \frac{1}{6.3 f_p}, \tag{3.17}$$

where f_p is the FWHM of the spectrum in Hz; this number will vary slightly depending upon pulse length and FROG technique.

The algorithm requires that the wavelength and temporal increment be accurately specified, since inaccuracy in either of the two increments will lead to an error in the properties of the retrieved pulse ($\tau, \Delta\omega, \phi$ etc). The percentage error in retrieved pulse property varies from pulse to pulse but is estimated in [6] to be of the same order as the size of the percentage error in either the wavelength or time increment.

Additional features can be formed in the spectrogram of a VECSEL pulse train in the form of random spikes in intensity at various delays. These spikes are caused by the VECSEL becoming unstable during lasing and switching between single pulse, cw-operation and various multi-pulse regimes. The consequence of these effects upon the pulse retrieved by the algorithm will be discussed later.

3.4 Phase Retrieval with a 1 GHz VECSEL

The VECSEL used for this measurement produced a train of double pulses with an average power of 13 mw and FWHM pulse length of 590 fs (sech^2 fit). The spectrum had a bandwidth of 3.27 nm centred at 1046.9 nm; the pulse train was 1.68-times transform-limited. During the measurement the heat sink upon which the gain chip was mounted was held at a constant temperature of 22°C. The FROG measurement recorded spectra at 512 different delays using a step size of 12 fs and an integration time of 80 ms, the total measurement took just over 2 min. After the FROG trace

was taken, a second autocorrelation and spectrum were recorded and the power was measured. The pulse length had dropped to 570 fs and the bandwidth had narrowed to 3.16 nm, meaning that the pulse train was 1.57-times transform-limited after the FROG measurement; the average power was now 11.8 mW.

The validity of the experimentally recorded spectrogram can be checked before using the algorithm by comparison with the recorded autocorrelation and spectrum. This is achieved by calculating the delay and frequency marginals of the spectrogram. The delay marginal is the integral of the FROG trace along the frequency axis, and should reproduce the intensity autocorrelation of the pulse. The frequency marginal is the integral of the FROG trace along the delay axis. For SHG FROG the frequency marginal has the form ([11] page 205):

$$M_{\omega}^{SHG}(\omega - 2\omega_0) = S(\omega - 2\omega_0)^* S(\omega - 2\omega_0), \tag{3.18}$$

where S($\omega - 2\omega_0$) is the measured spectrum and $*$ indicates convolution.

To check the stability of the VECSEL, the spectrum and fast scope trace of the pulse train were continuously observed during the FROG measurement. In figure 3.4 two spectrograms are shown, one for a stable VECSEL producing a train of double pulses; the second spectrogram is distorted as the VECSEL was switching in-between cw-lasing and different multiple pulse regimes during the measurement. In figure 3.5 the marginals calculated from the FROG trace (blue curves) have been overlapped with the corresponding experimental data (red curves). The data on the left corresponds to the stable VECSEL producing double pulses continuously throughout the FROG measurement, and the data on the right is from the less stable VECSEL that was shifting between different multiple pulse regimes.

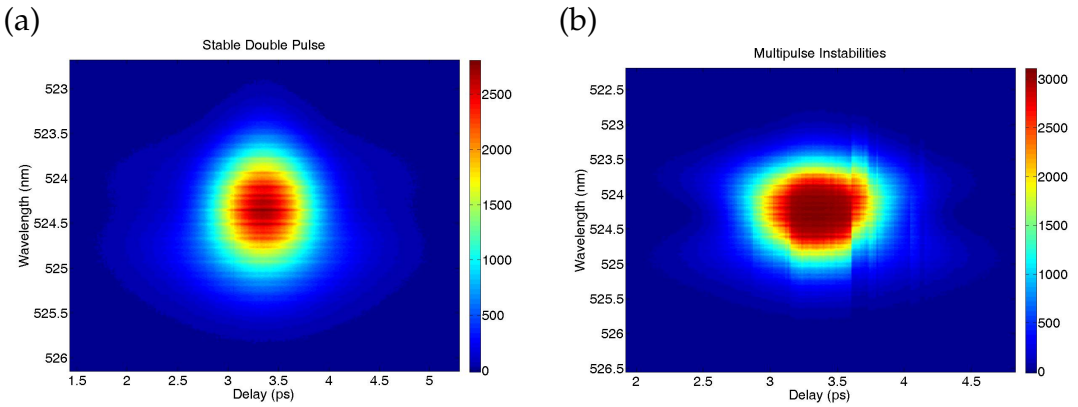

Figure 3.4: Experimentally recorded FROG traces of (a) 1 GHz VECSEL emitting a train of double pulses with average power 12.4 mW; (b) the same laser switching between different numbers of multiple pulses and CW operation, average power 19.55 mW. Number of steps were 512, step size was 13 fs, integration time was 80 ms.

It is evident that the instability in the second VECSEL produces errors between the retrieved marginals and measured data; such a FROG trace will not reliably recreate the complex field of the VECSEL. The marginals (3.5) for the FROG traces in figure 3.4 are in agreement with the measured data for the stable VECSEL, indicating an acurately recorded spectrogram; the slight discrepancy can be attributed to the reduction in chirp and average power of the VECSEL over the course of the FROG measurement. The marginals for the unstable VECSEL, figure 3.5 b), have a greater discrepency with the measured data, indicating that correct phase information about the pulse train can not be reliably retrieved from this FROG trace.

It is difficult to assess how the slight changes in pulse train properties during the measurements will affect the validity of the E-field retrieved by the algorithm. The discrepancy between marginals and experimental data depends upon noise in the experiment and not on the changing pulse properties. The effect upon the retrieved E-field of experimental errors can be assumed to be small as these discrepancies are greatest in the wings of the curves where the intensity and thus signal to noise ratio are lowest. A check of this statement can be made by comparing the experimental FROG trace to the trace generated by inputting the retrieved E-field into equation 3.7; the two traces are plotted alongside each other in figure 3.6.

Firstly, it should be noted that the experimental FROG trace is symmetrical about the delay axis; this suggests that the slow evolution of the pulse properties has had only a small effect upon the measurement. Visually, the two traces are very similar,

indicating that the algorithm was able to reliably recreate the E-field of the pulse. A more quantitative comparison is possible by calculating the FROG error [6]

$$G = \left[\frac{1}{N^2}\sum(I_{FROG}(\omega,\tau) - \left|E_{sig}(\omega,\tau)\right|^2)^2\right]^{\frac{1}{2}}, \tag{3.19}$$

defined as the RMS deviation between the experimental and retrieved FROG traces. This provides a statistical comparison of the measured spectrogram with the trace retrieved by the algorithm. For the 1 GHz data above G = 0.0073. The FROG error for accurate retrieval of low-noise data is expected to be less than 0.005 for a step size of N = 128 as reported in [5]; for N = 512 this falls to 0.0025 as the error scales as $N^{-\frac{1}{2}}$. However, these numbers are based on the performance of lasers operating at much lower repetition rates to the VECSELs described in this work.

(a)

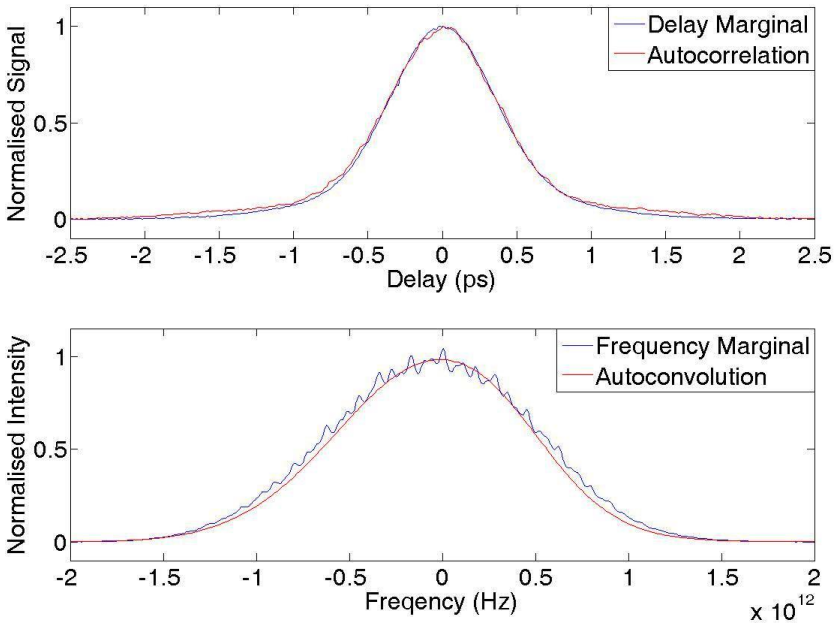

(b)

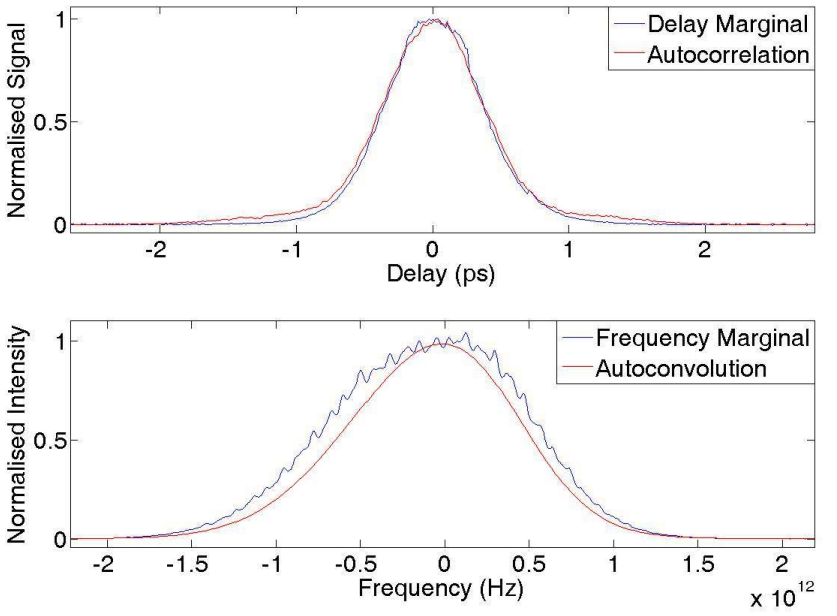

Figure 3.5: Delay and frequency marginals (blue curves) overlapped with experimentally measured autocorrelations and spectral convolutions (red curves). Marginlas are calculated for data from figure 3.4, (a) stable double pulse, (b) switching between multiple pulsing and cw-operation.

(a)

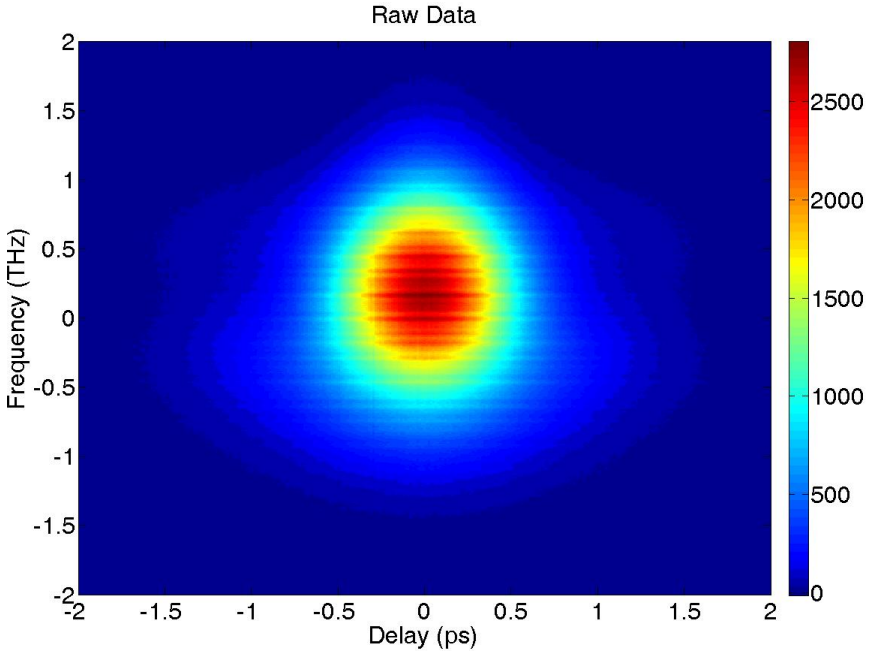

(b)

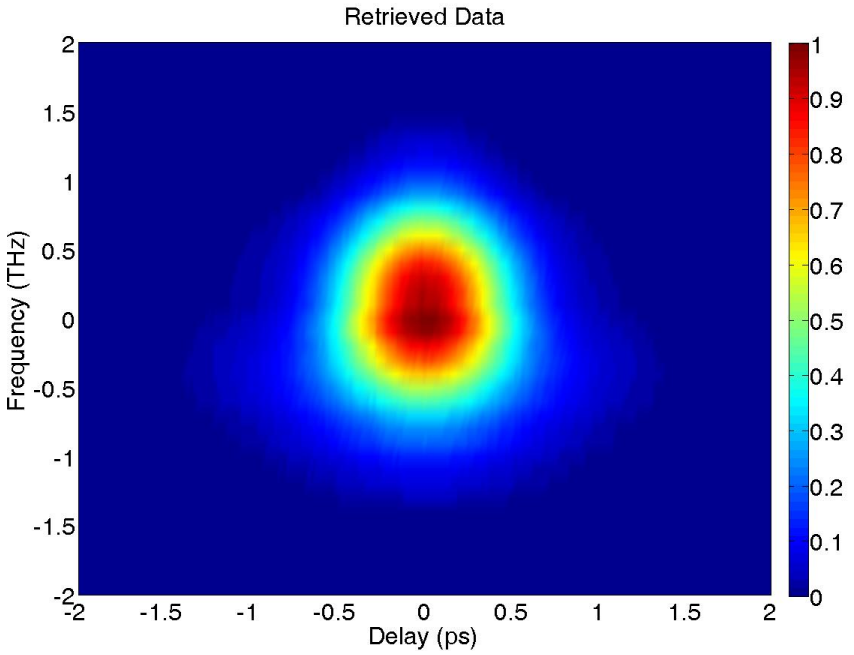

Figure 3.6: Experimental FROG trace (a) and the corresponding trace retrieved by the FROG algorithm (b). The VECSEL emitted a train of double pulses with an average power of 13 mW, pulse length = 590 fs (sech^2) and the bandwidth was 3.27 nm centered at 1046.9 nm measured before recording the FROG trace; the average power changed to 11.8 mW, pulse length 570 fs (sech^2) and the bandwidth was 3.16 nm centered at 1046.9 nm all measured after recording the FROG trace. The calculated FROG error was 0.0073. Number of steps = 512, step size = 12 fs, integration time = 120 ms.

The validity of the pulse retrieved by the algorithm can be checked by comparison with the measured autocorrelation and optical spectrum. To this end, the measured spectrum and autocorrelation are plotted in figure 3.7 along with the equivalent quantities generated from the retrieved E-field. The excellent agreement between the two sets of data indicates that the algorithm has retrieved the pulse accurately.

The measured spectrum has been converted to frequency and both the measured and retrieved spectra have been centred about a particular value of frequency determined by the algorithm, where negative frequency corresponds to longer wavelengths. The retrieved spectrum has approximately the same asymmetric shape as the measured spectrum but lacks the modulations caused by the substrate reflections within the VECSEL. The retrieved spectrum is slightly narrower, deviating from the shape of the measured spectrum more strongly in the low intensity edges of the trace.

A sech^2 fit has been assumed for the measured autocorrelation. The normalised plot has been multiplied by 0.648, and overlaps very well with the square modulus of the retrieved E-field; the only disagreement occurs in the low intensity edges. There are also peaks in the measured autocorrelation at $\pm$ 4 ps; these are caused by substrate reflections within the VECSEL and are estimated to have less than 5 % of the pulse energy. Figure 3.7 indicates that the algorithm has reliably recreated the electric field of the pulse with some disagreement with the experimental data in low intensity edges of the pulse; this can be attributed to noise in the FROG trace. The additional features of modulation in the spectrum and the additional peaks in the autocorrelation are absent from the retrieved data as the sampled time window was not long enough to capture this information; the additional features in the autocorrelation are separated by about 10 ps while the total delay of the FROG trace was just over 6 ps.

The imaginary part of the retrieved electric field contains nearly complete information about the phase of the measured pulse train. FROG is insensitive to the absolute phase and to translations of the whole pulse in time. In order to present this information in the time and frequency domains, the instantaneous frequency and group delay (equations 3.8-3.9) are plotted in figure 3.8.

(a)

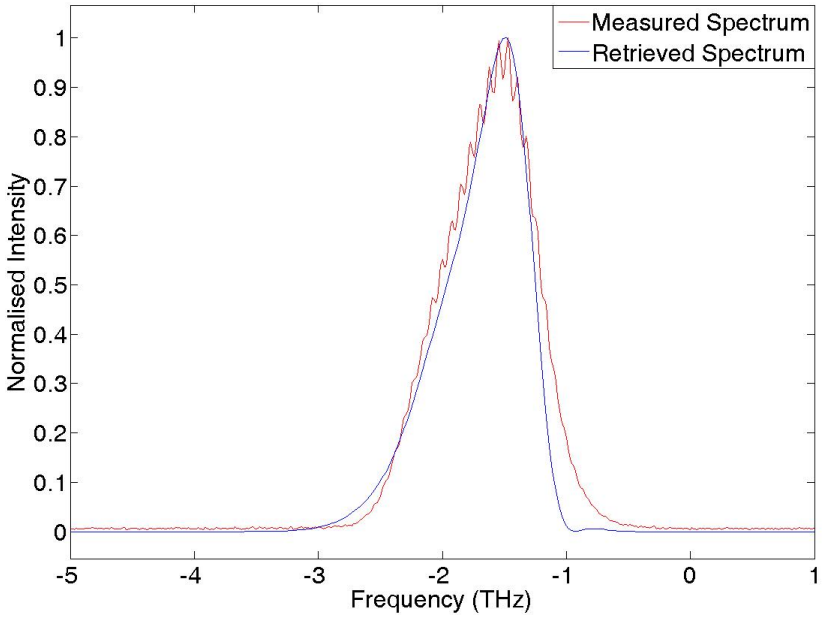

(b)

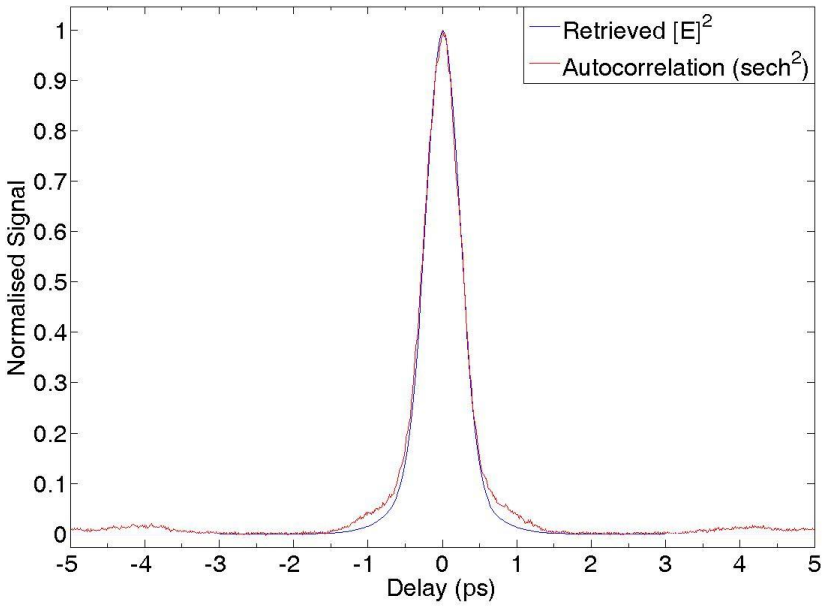

Figure 3.7: Retrieved spectrum (a) and square modulus of the E-field (b) corresponding to the 1 GHz VECSEL data of figure 3.6. The data has been normalized and is plotted along with the autocorrelation multiplied by 0.648 ($sech^2$) and measured spectrum. The modulations in the measured spectrum are caused by reflections from the substrate of the VECSEL chip and do not appear in the FROG data as the temporal sampling range was to low; the side pulses in the measured autocorrelation are caused by the same effect and are also absent from the retrieved data.

(a)

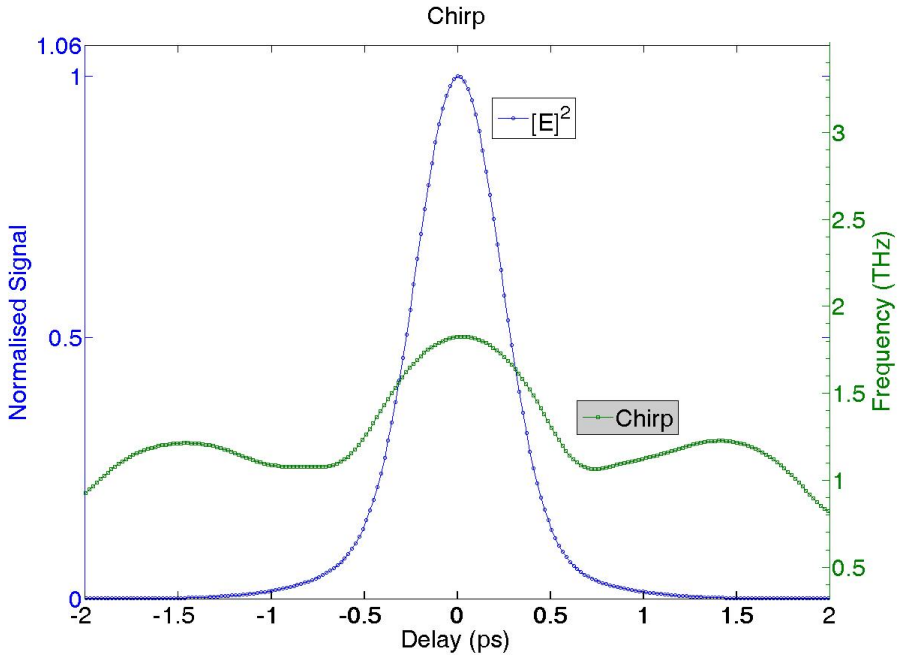

(b)

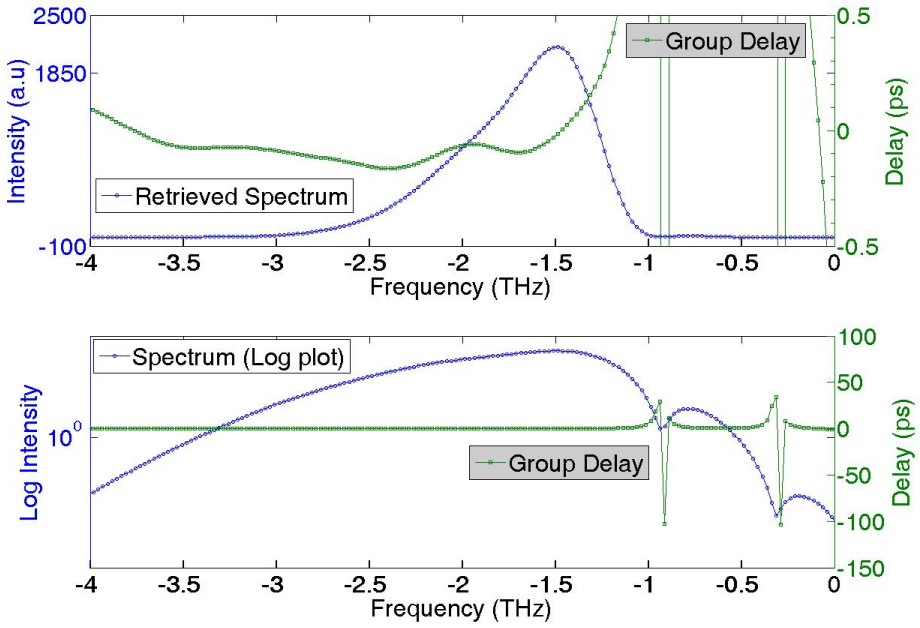

Figure 3.8: Instantaneous frequency and group delay retrieved by the algorithm for the 1 GHz VECSEL, data in figure 3.7. The instantaneous frequency (a) is plotted along with the square modulus of the retrieved E-field (blue curve), while the group delay (b) is plotted along with the retrieved spectrum (blue curve). A log plot of the spectrum is included showing artificial spikes in the group delay when the intensity of the spectrum reaches a minimum. The phase information in these plots only has a real meaning where it corresponds to a non-zero value of the spectrum/square modulus of the E-field.

The instantaneous frequency only has a real meaning for non-zero values of the square modulus of the E-field (blue curve, a). Figure 3.8 a) shows that the instantaneous frequency varies parabolically across the pulse, rising from a minimum of 1.075 THz at a delay of - 0.78 ps, up to a maximum of 1.82 THz near zero delay, then falling to another minimum of 1.065 THz at 0.72 ps. Due to the symmetry inherent in FROG the delay axis in this plot is reversible in time.

The group delay only has a real meaning for non-zero values of the spectral intensity (blue curve, b). The group delay varies parabolically across the pulse. It has two local minima that coincide with the pulse, one near the centre and the other towards the edge on the long frequency side (0.165 ps). The group delay rises to a much higher value as the pulse goes towards shorter wavelengths (0.421 ps corresponding to a similar spectral intensity as the first minimum). Due to the symmetry in FROG, the group delay is reversible about the zero point in the delay axis.

To quantify the nonlinear phase structure of the retrieved pulse, the group delay and instantaneous frequency plots have been fitted with polynomial curves. In figure 3.9 a), a second order polynomial has been fitted to the instantaneous frequency curve.

From the parameters of the fitted curve it is estimated that the instantaneous frequency (defined in equation 3.8) be given by

$$\omega(t) = \omega_0 + At - Bt^2, \tag{3.20}$$

where A = 0.1, B = 2.185 and t is measured in picoseconds. No value for the carrier envelope phase ω_0 is quated since the FROG technique is insensitve to this order of phase. By integrating equation 3.20 with respect to t we obtain the temporal phase of the pulse

$$\phi(t) = \phi_0 + \omega_0 t + \frac{1}{2}At^2 - \frac{1}{3}Bt^3. \tag{3.21}$$

In figure 3.9 b) a third order polynomial has been fitted to the group delay curve. From the parameters of the fit it is shown that the group delay

$$T_g(\omega) = A + B(\omega - \omega_0) + C(\omega - \omega_0)^2 + D(\omega - \omega_0)^3, \tag{3.22}$$

where B = 19.506, C = 10.651, D = 1.929 and ω is the angular frequency measured in rad/sec. The constant term A corresponds to a translation of the pulse envelope in time which FROG is not sensitive to.

(a)

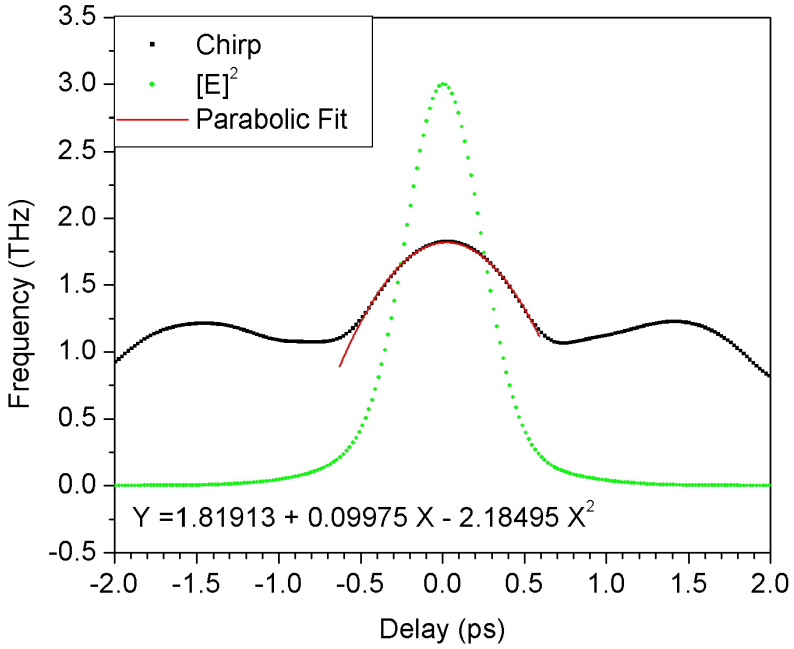

(b)

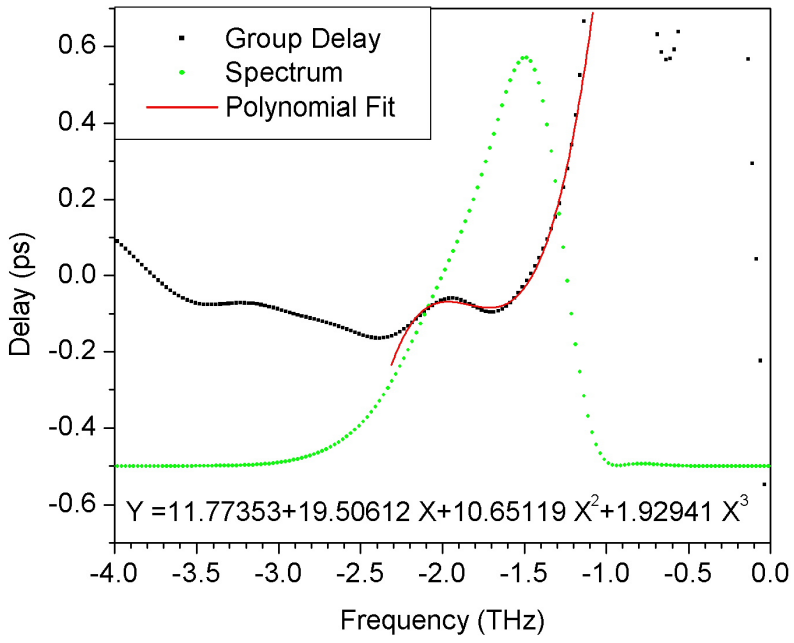

Figure 3.9: Polynomial fit (red curves) to chirp and group delay (black curves) of data from figure 3.8; note that the phase information in the plots only has real meaning for non-zero values of the spectrum/square modulus of the E-field (green curves). The fitting parameters for these curves are given at the bottom of the plots.

The group delay dispersion of the pulse is obtained by differentiating equation 3.22, giving a value of 3.104 ps^2. By taking the second and third derivatives of equation 3.22 we obtain a value for the third order dispersion on 0.540 ps^3 and 0.047 fs^4 for the fourth order dispersion.

It should be noted that the above result was obtained for a laser that supported two optical pulses within the cavity. It will be shown in the preceding subsection that the VECSELs propensity to multi-pulse will not affect the reliability of the retrieved FROG trace and phase information, provided that each of the pulses within the VECSEL cavity are identical. To investigate the effect of multiple pulsing further, the phase structure of a fundamentaly mode-locked VECSEL was measured; the results of which are presented in section 3.5. It proved experimentaly difficult to suppress the multiple pulsing of the VECSEL at 1 GHz, so it was necessary to build a cavity with a higher repetition rate; at 6 GHz it was found that the intra-cavity pulse energy had dropped sufficiently to sustain fundamental mode-locking. However, the drop in pulse energy seriously reduces the second harmonic signal obtained from BBO crystal; at 6 GHz we are thus very close to the limit in sensitivity of the FROG setup used in this work.

3.4.1 Validity of the Multi-Pulse Measurement

Multiple pulsing is a symptom of the laser operating in a regime of lowest intracavity loss. In VECSELs, this arises whenever the peak power of the pulse exceeds some maximum value characteristic of the laser. It is observed that the average power of a VECSEL, at a particular repetition rate, increases with pulse number in a step like manner; with a double pulsed VECSEL having approximately twice the average power of a fundamentally mode-locked VECSEL.

If we assume that each pulse within the cavity of a multipulsing VECSEL has the same energy, then each pulse will experience similar pulse shaping effects per round trip, provided that their spacing allows for recovery of all saturable effects between adjacent pulses. In such a case the pulses will be nearly identical.

The fast scope trace of the double pulse train observed during the FROG measurement is displayed in figure 3.10. The trace shows a train of double pulses separated by the cavity round trip time of 1 ns. The spacing between each pulse in the cavity (Δt) is equal to 160 ps. This time is sufficient for both the gain of the VECSEL and the

absorption of the SESAM to recover between pulses.

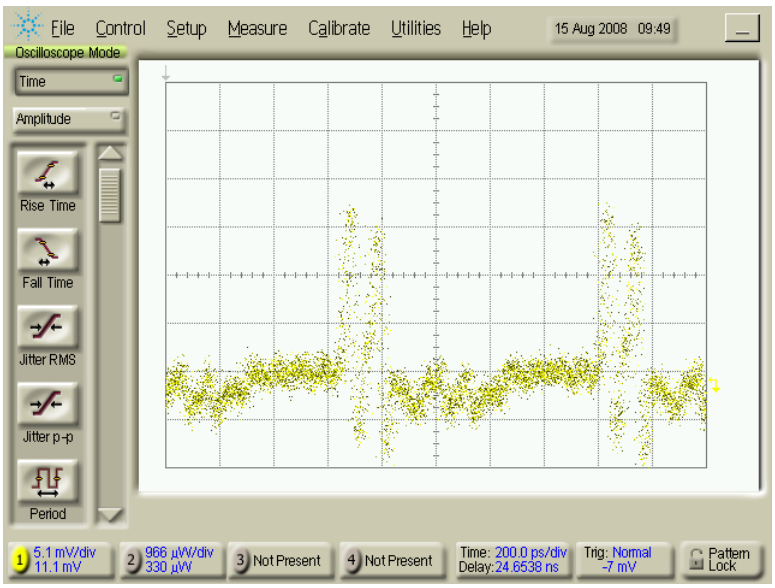

Figure 3.10: Fast scope trace of the stable 1 GHz VECSEL, showing a train of double pulses. Individual pulses are separated by aproximately 160 ps.

Without making any assumptions about the form of the double pulse train, other than to say that the pulse spacing remains constant during the FROG measurement, the signal field generated by a double pulse train will have the form

$$E_{sig} = (E_1(t) + E_2(t))\,[E_1(t-\tau) + E_2(t-\tau)]\,. \tag{3.23}$$

Equation 3.23 can be expanded to give

$$E_{sig} = E_1(t)E_1(t-\tau) + E_2(t)E_2(t-\tau) + E_1(t)E_2(t-\tau) + E_2(t)E_1(t-\tau), \tag{3.24}$$

where $E_1(t)$ and $E_2(t)$ are the electric fields of each of the pairs of the pulses in the pulse train. The spacing between the two pulses, Δt, is far greater than the total delay of the FROG scan so that each pulse will only overlap with itself inside the BBO crystal; this means that the last two terms in equation 3.24 equate to zero. It follows that the recorded spectrogram will be of the form

$$I_{FROG}(\omega,\tau) = \left|\int dt E_1(t)E_1(t-\tau)exp(i\omega_t) + \int dt E_2(t)E_2(t-\tau)exp(i\omega_t)\right|^2. \tag{3.25}$$

In the case where $E_1 = E_2$

$$I_{FROG}(\omega,\tau) = \left|2\int dt E(t)E(t-\tau)exp(i\omega_t)\right|^2. \tag{3.26}$$

Clearly any difference between the two pulses will change the form of the spectrogram and thus the retrieved phase information.

3.5 Phase Retrieval with a 6 GHz VECSEL

The FROG data presented so far has been for a 1 GHz VECSEL operating in a multi-pulse regime with two pulses in the cavity. It proved difficult to operate this gain sample in a stable single pulse regime for long enough to acquire a reliable FROG trace of its phase structure; so it was decided to create a VECSEL with the same gain material operating at a 6 GHz repetition rate. The advantage of the higher repetition rate is to decrease the peak power of the VECSEL pulses while keeping the average power essentially the same as in the 1 GHz case; this effectively ensures stable single pulse operation of the laser. The disadvantage of this approach is that the signal to noise ratio of the FROG measurement will decrease as the intensity of second harmonic light generated depends strongly upon the pulse energy.

There are a number of differences between the two lasers that may affect the underlying phase structure of the pulse trains. These differences are listed below in table 3.1.

Laser Property	**1 GHz**	**6 GHz**
Average Power Before FROG	13.8 mW	14.6 mW
Average Power After FROG	11.8 mW	14.6 mW
Pulse Length Before FROG	590 fs $\pm$ 10 fs	730 fs $\pm$ 10 fs
Pulse Length After FROG	570 fs $\pm$ 10 fs	740 fs $\pm$ 10 fs
Average Pulse Energy	0.886 nJ	0.348 nJ
Peak Power on the Gain*	11.9 MW/cm^2	3.7 MW/cm^2
Peak Power on the SESAM**	427.9 MW/cm^2	132.6 MW/cm^2
Gain Heat Sink Temperature	22°C	27.6°C
Centre Wavelength	1046.9 nm	1049.8 nm
Bandwidth Before FROG	3.27 nm	2.45 nm
Bandwidth After FROG	3.16 nm	2.37 nm
Calculated Cavity GDD	366.39 fs^2	224.76 fs^2
Calculated Cavity TOD	32000 fs^3	25572 fs^3

Table 3.1: Properties of the 1 and 6 GHz VECSELs relevant to a discussion of phase structure in the laser pulse train.*Peak power assumes a 60 μm spot upon the gain.**Peak power assumes a 10 μm spot upon the SESAM.

The angle between the cavity mode and the gain chip is greater in the 6 GHz VECSEL resulting in an effective increase in the optical thickness of the gain with respect to the 1 GHz laser; all the differences in the table above can be attributed to this increase in optical thickness. The GDD $d^2\phi(\omega)/d\omega^2$ and TOD $d^3\phi(\omega)/d\omega^3$ of the cavity are quoted as the sum of GDD(TOD) from a single pass upon both the SESAM and gain chip, the value depends upon the centre wavelength of the pulse and the structure of the SESAM/gain chip; the technique for calculating these values has been described in section 2.2.

The experimental and retrieved FROG traces are shown in figure 3.11. Due to the lower second harmonic signal it was necessary to use a longer integration time of 360 ms to record the trace. The number of steps used was 512 fs and the step size was 13 fs. The experimental trace has a very similar shape to the 1 GHz data, differing mainly around the edges where there is some low intensity signal that trails off towards long delay. This low intensity signal has not been retrieved by the algorithm. The corresponding FROG error is 0.0051, a value that is lower than the 1 GHz measurement suggesting a more accurate retrieval.

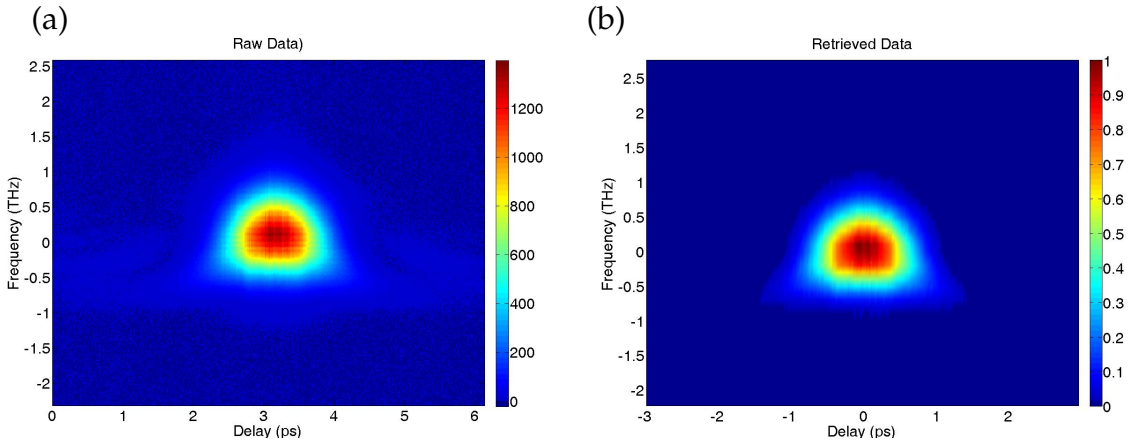

Figure 3.11: Experimental FROG trace (a) and the trace retrieved by the algorithm (b). The laser was a 6 GHz VECSEL emitting a train of single pulses. The train had a centre wavelength of 1049.8 nm with a 2.45 nm bandwidth and average power of 14.6 mW measured before FROG; the pulse length was 730 fs assuming a sech^2 fit. After the FROG trace was recorded the average power remained at 14.6 mW, the bandwidth had slightly narrowed to 2.37 nm centered at 1049.8 nm while the pulse length had increased to 740 fs. The FROG error was 0.0051.

(a)

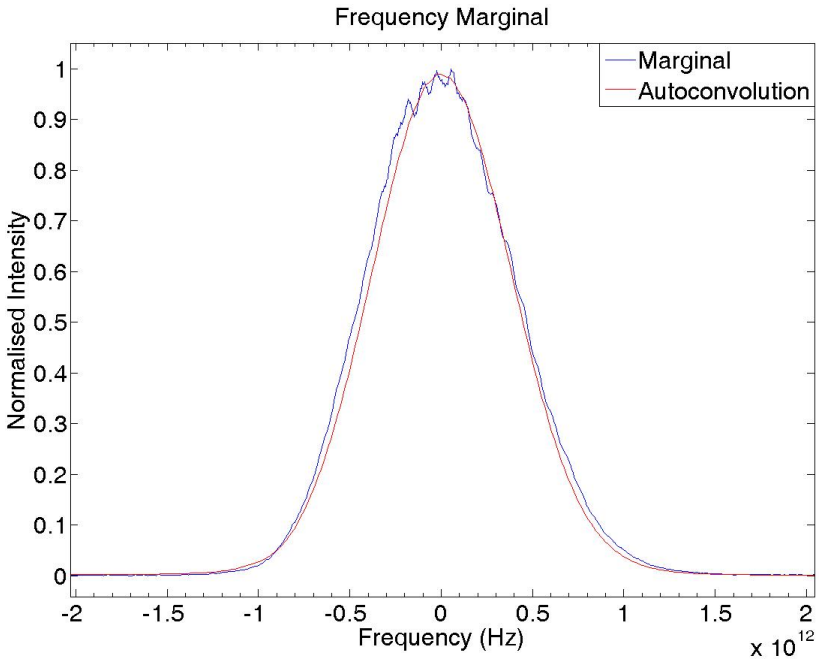

(b)

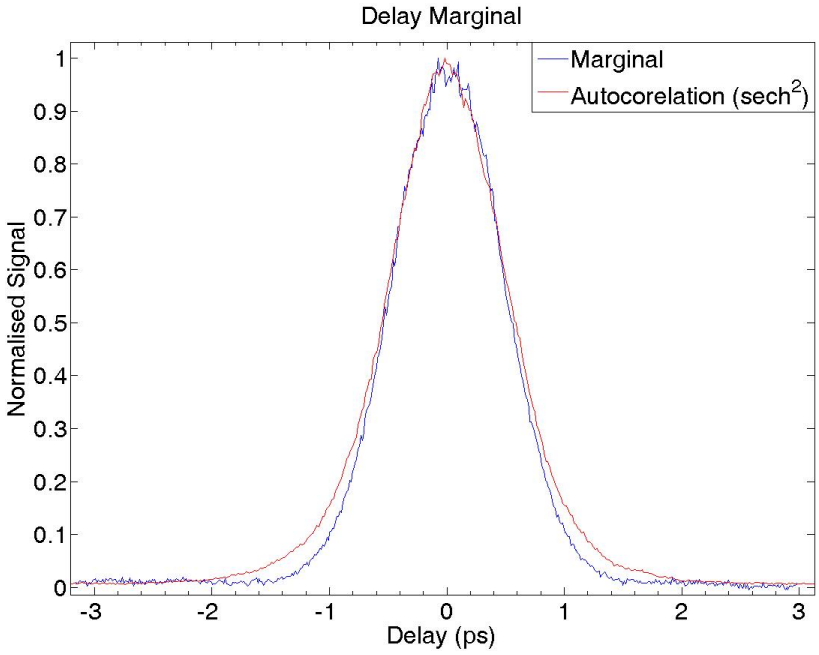

Figure 3.12: Normalized frequency (a) and delay marginals (b) of the experimental FROG trace of figure 3.11 (blue curves); plotted on the same axis are the experimentally measured autocorrelation and spectrum (red curves).

The validity of the experimental FROG trace is again estimated by comparing the marginals with the measured spectral convolution and autocorrelation. The frequency marginal for the 6 GHz trace is shown in figure 3.12 a) plotted along with the measured spectrum. The delay marginal is plotted along with the measured autocorrelation in figure 3.12 b). The frequency marginal is a similar shape to the autoconvolution of the measured spectrum disagreeing more strongly in the low intensity edges of the trace. The agreement seems to be less than with the 1 GHz VECSEL. The autocorrelation agrees strongly with the delay marginal again differing most in the low intensity edges of the trace.

The reliability of the retrieved E-field is again checked against the measured autocorrelation and spectrum. The retrieved spectrum is plotted in figure 3.13 a) along with the measured spectrum. In figure 3.13 b) the square modulus of the retrieved E-field is plotted in the time domain along with the measured autocorrelation (assuming a sech^2 fit).

The spectrum retrieved by the algorithm from the 6 GHz trace is a similar shape to the retrieved spectrum in figure 3.7 a) using the 1 GHz VECSEL; again more negative frequency corresponds to longer wavelength. Both the 1 GHz and 6 GHz spectra are asymmetric with a second low intensity peak towards shorter wavelengths. This time the experimentally recorded spectrum disagrees more strongly with the retrieved spectrum. The measured and retrieved spectra stop overlapping at the edges of the trace below about 40 % of the peak intensity. The two spectra differ in shape most strongly towards the left of the plot where there is a dip in the measured spectrum near -4.7 THz; this dip is absent from the retrieved spectrum and could be an artefact suggesting a slightly misaligned spectrometer.

The square modulus of the retrieved E-Field agrees closely with the same quantity measured by the autocorrelator, here a sech squared fit has been assumed. The only disagreement occurs in the low intensity edges. Both the measured spectrum and autocorrelation contain additional features that are caused by substrate reflections within the VECSEL. These features are again absent from the retrieved data as the sampled time window was not long enough to capture this information.

The instantaneous frequency of the pulse is plotted in figure 3.14 a) along with the square modulus of the retrieved E-field. The graph shows that the pulse again has a nonlinear chirp.

(a)

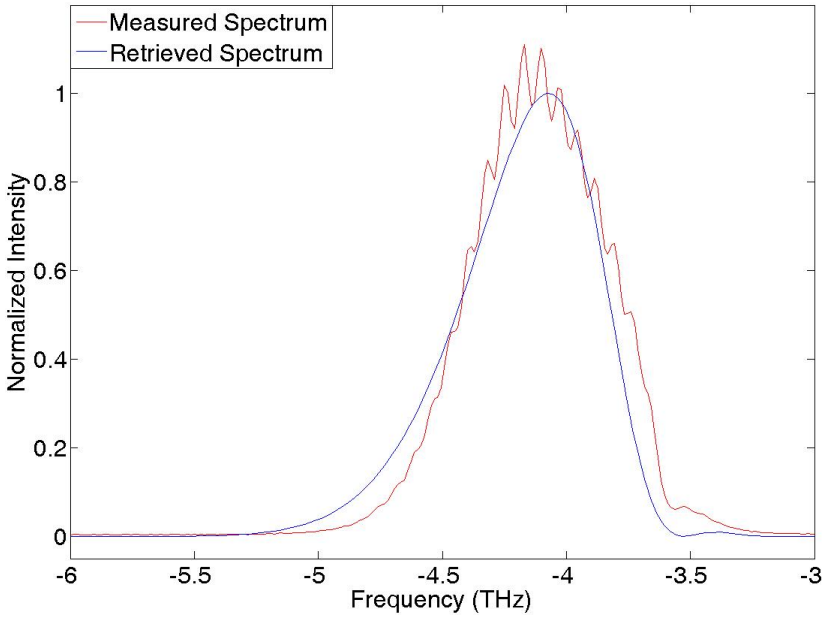

(b)

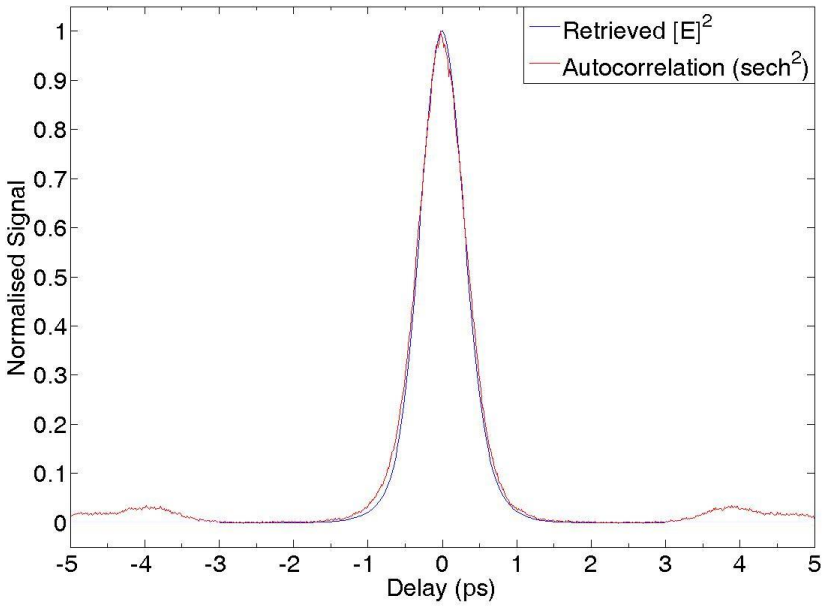

Figure 3.13: Retrieved spectrum (a) and square modulus of the E-field (b) (blue curves) plotted along with the measured autocorrelation multiplied by 0.648 ($sech^2$ fit) and spectrum. All the curves have been normalized. There is evidence of substrate reflections in both the measured spectrum and autocorrelation that has not been picked up by the FROG measurement.

(a)

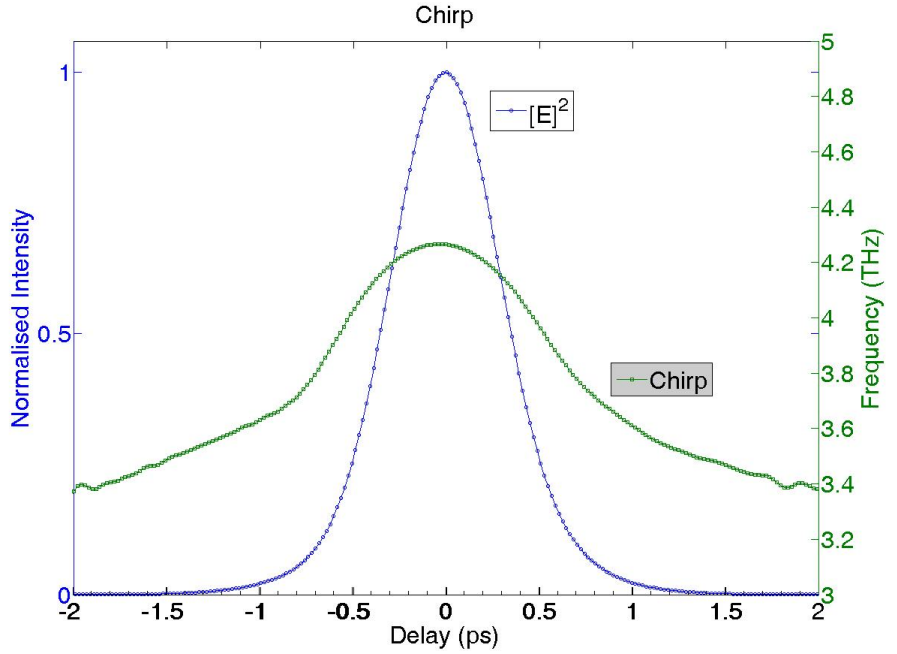

(b)

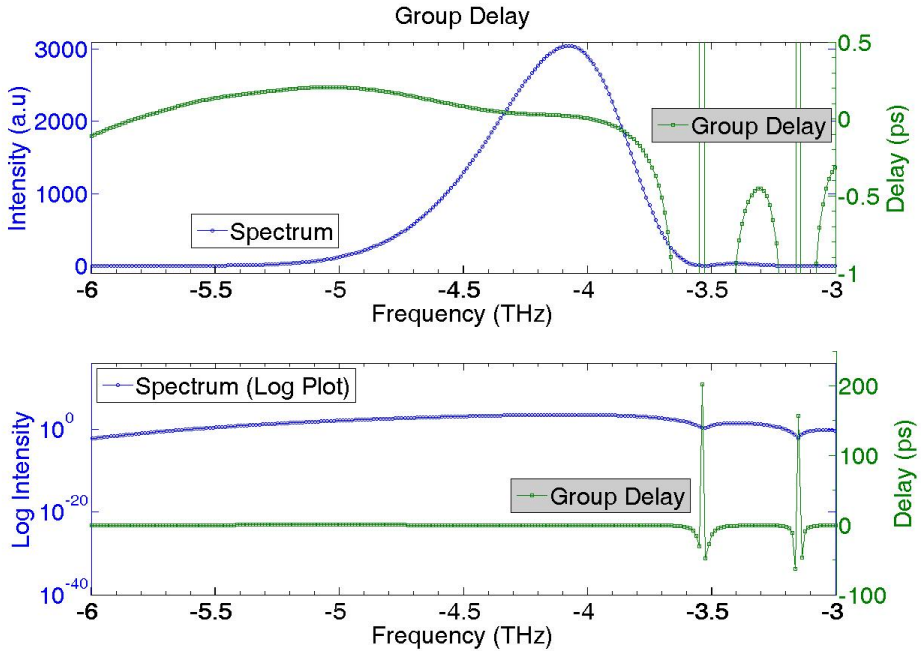

Figure 3.14: Instantaneous frequency and square modulus of the retrieved E-field (a). Group delay and retrieved spectrum are plotted along with a log plot of the retrieved spectrum (b). There are two artificial spikes in the group delay corresponding to local minimum in the retrieved spectrum.

The instantaneous frequency varies parabolically, rising from a minimum of 3.812 THz at a delay of - 0.68 ps up to a maximum of 4.267 THz near zero delay before falling to 3.828 THz at a delay of 0.64 ps. The phase information is again represented in the frequency domain by plotting the group delay of the pulse, shown in figure 3.14 b) along with the retrieved optical spectrum. The nonlinear phase structure is evident in the group delay, which varies across the pulse. The curve appears to be upside down, having a similar shape to the group delay of the 1 GHz VECSEL when mirrored about zero delay. Due to the ambiguity in SHG-FROG it is impossible to tell whether the group delay of the two lasers do have the same sign. Again to quantify the nonlinear phase structure of the retrieved pulse, the group delay and instantaneous frequency plots have been fitted with polynomial curves. In figure 3.15 a) a second order polynomial has been fitted to the instantaneous frequency curve.

From the parameters of the fitted curve it is estimated that the instantaneous frequency is

$$\omega(t) = \omega_0 - At - Bt^2, \tag{3.27}$$

where A = 0.056, B = 1.08 and t is measured in picoseconds. It is tempting to assume that the constant term, ω_0, in the instantaneous frequency corresponds to the carrier envelope phase of the pulse, however FROG is not sensitive to this order of phase so again no number is quoted. By integrating equation 3.27 with respect to t we obtain the temporal phase of the pulse

$$\phi(t) = \phi_0 + \omega_0 t - \frac{1}{2}At^2 - \frac{1}{3}Bt^3. \tag{3.28}$$

In figure 3.15 b) a third order parabola has been fitted to the group delay curve. From the parameters of the fit it is shown that the group delay

$$T_g(\omega) = -A - B(\omega - \omega_0) - C(\omega - \omega_0)^2 - D(\omega - \omega_0)^3. \tag{3.29}$$

Again the constant term, A, has no real meaning here, it corresponds to a translation of the pulse envelope in time which FROG is not sensitive to. The other terms in equation 3.29 have the following values: B = 116.444, C = 55.224, D = 2.175 and ω is measured in rad/sec. The group delay dispersion of the pulse is obtained by differentiating equation 3.29, giving a value for the GDD of -26.490 ps^2. By taking the second and third derivatives of equation 3.29 we get a value for the third order dispersion of 1.399 ps^3, and 0.053 ps^4 for the fourth order dispersion.

(a)

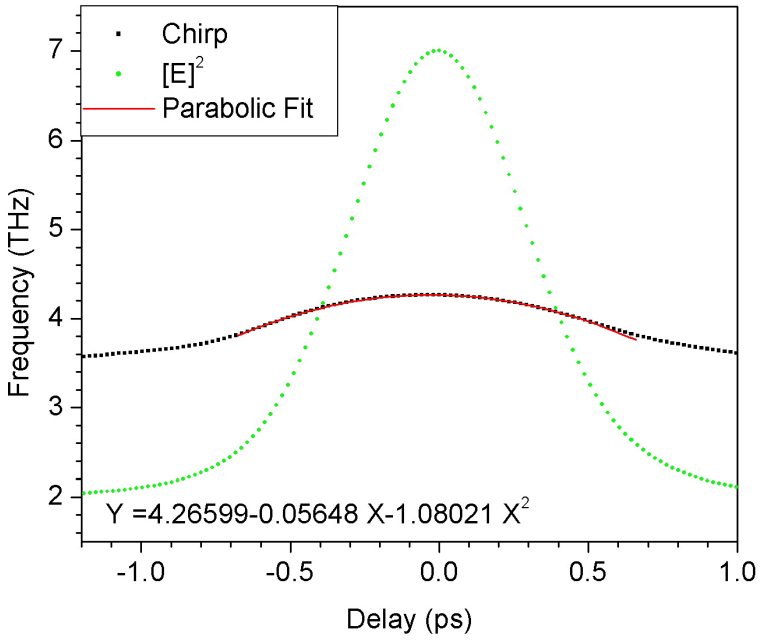

(b)

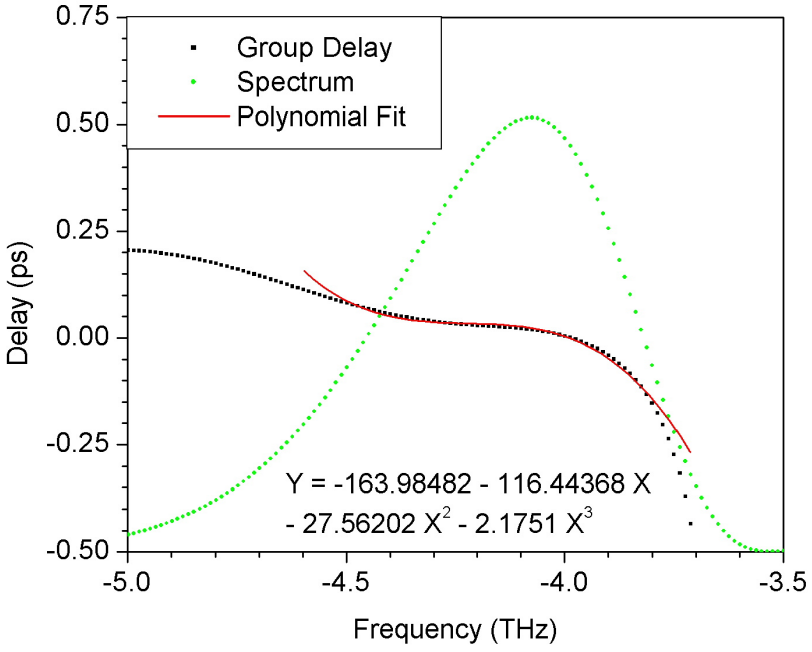

Figure 3.15: Parabolic fit (red curves) to chirp and group delay (black curves) of data from figure 3.14; the phase information in the plots only has real meaning for non zero values of the spectrum/square modulus of the E-field (green curves). The fit parameters for these curves are given at the bottom of the plots.

3.6 Discussion of Results and Conclusions

A single VECSEL gain chip has been mode-locked at two different repetition rates and the phase structure of the resulting pulse trains has been characterised using frequency resolved optical gating. The 1 GHz VECSEL produced a train of double pulses which were 1.57 times transform limited. The 6 GHz laser produced a train of single pulses that were 1.52 times the transform limit. In table 3.2 the results of the FROG measurement are presented for comparison of the two different repetition rates.

Pulse Property	1 GHz VECSEL	6 GHz VECSEL
ϕ_a(t)	$0.05t^2$ - $0.728t^3$	- $0.028t^2$ - 0.36 t^3
GDD	3.104 ps^2	-26.490 ps^2
TOD	0.54 ps^3	-1.399 ps^3
$\Delta\upsilon\Delta\tau$	0.495	0.479

Table 3.2: Comparison of the phase properties of a VECSEL gain chip operating at two different repetition rates.

In the time domain the temporal phase ϕ_a(t) appears to have a different sign for each repetition rate, this may or may not be the case as there is a temporal ambiguity in the SHG FROG measurement. If for example the curve in figure 3.15 a) were flipped about zero in the time axis then the sign of the two would agree. For both repetition rates the pulse train is shown to have a non-zero-cubic phase term. Assuming the sign of the two temporal phases to be the same for each term, the second order temporal phase is 1.79 times larger for the 1 GHz VECSEL and the third order term is 2.02 times larger.

In the frequency domain, values for the group delay dispersion and third order dispersion have been extracted and are displayed in table 3.2. If the sign of the dispersion is again ignored then the two FROG measurements show qualitatively the same behaviour; the VECSEL produces a pulse that has undergone a non-zero group delay dispersion and a small amount of third order dispersion. Quantitatively the 6 GHz VECSEL has experienced nearly nine times as much GDD and almost three times as much TOD as the 1 GHz pulse train.

The FROG measurement has shown that when a Stark mode-locked VECSEL is

adjusted to give maximum bandwidth, the resulting non-transform limited pulse will have a nonlinear chirp arising from a cubic temporal phase; such a chirp is difficult to compress as there is also a quadratic dependence of the temporal phase.

There are many physical mechanisms in a VECSEL that contribute to the phase structure observed in this work. There is a contribution to GDD and TOD arising from the multilayer structure of the gain chip and the SESAM; material dispersion and SPM are always present, and there are also saturation effects within the semiconductor mirrors. An optical pulse incident upon the gain/SESAM will cause a dynamic change to the carrier density of the semiconductor. The changing carrier density in turn alters the gain and refractive index experienced by the pulse; this enhances the line-width of the laser and introduces dispersion to the pulse. It has been reported that the interplay between the carrier-dependent phase change and positive cavity dispersion could result in the formation of quasi-soliton mode-locked pulses of the laser. This effect has been predicted by Pashotta et al. [12] using numerical modelling for pulses greater than 1 ps in length.

3.7 References

[1] E. Siegman, A. *Lasers*. university Science Books, 1986.

[2] Z. Varallyay, J. Fekete, A. Banyasz, and R. Szipocs. "Optimizing input and output chirps up to the third-order for sub-nanojoule, ultra-short pulse compression in small core area PCF". *Applied Physics B (Lasers and Optics)*, B86(4):567–72, 2007.

[3] D. J. Kane and R. Trebino. "Characterization of arbitrary femtosecond pulses using frequency-resolved optical gating". *IEEE Journal of Quantum Electronics*, 29(2):571–9, 1993.

[4] K. W. DeLong, R. Trebino, and D. J. Kane. "Comparison of ultrashort-pulse frequency-resolved-optical-gating traces for three common beam geometries". *Journal of the Optical Society of America B (Optical Physics)*, 11(9):1595–608, 1994.

[5] R. Trebino, K. W. DeLong, D. N. Fittinghoff, J. N. Sweetser, M. A. Krumbugel, B. A. Richman, and D. J. Kane. "Measuring ultrashort laser pulses in the time-frequency domain using frequency-resolved optical gating". *Review of Scientific Instruments*, 68(9):3277–95, 1997.

[6] K. W. DeLong, R. Trebino, J. Hunter, and W. E. White. "Frequency-resolved optical gating with the use of second-harmonic generation". *Journal of the Optical Society of America B (Optical Physics)*, 11(11):2206–15, 1994.

[7] N. Trager, F. *Springer Handbook of Lasers and Optics*. Springer, 2007.

[8] W. Koechner. *Solid-State Laser Engineering*. Springer.

[9] E. Hecht. *OPtics*. Addison Wesley, 2002.

[10] K. W. DeLong, D. N. Fittinghoff, and R. Trebino. "Practical issues in ultrashort-laser-pulse measurement using frequency-resolved optical gating". *IEEE Journal of Quantum Electronics*, 32(7):1253–64, 1996.

[11] R. Trebino. *Frequency-resolved optical gating : the measurement of ultrashort laser pulses*. Kluwer Academic Publishers, 2000.

[12] R. Paschotta, R. Hring, A. Garnache, S. Hoogland, A. C. Tropper, and U. Keller. "Soliton-like pulse-shaping mechanism in passively mode-locked surface-emitting semiconductor lasers". *Applied Physics B: Lasers and Optics*, 75(4):445–451, 2002.

Chapter 4

Theory of Yb-Doped Fibre Amplifiers

Ytterbium doped optical fibre amplifiers allow for the scaling of a low power source emitting near 1 μm to high average powers. As the amplifier is also pumped near 1 μm, such amplifiers are very efficient; nearly 80 % efficiency being achievable. In the case of a double-clad fibre, the amplifier acts as a brightness converter, allowing for the high average power of a low brightness cw source characterised by a large M^2 to be converted into a pulsed signal with high beam quality (low M^2). The amplified signal will have pulse properties governed not only by the seed source but by the properties of the amplifier itself. The amplifier can be designed to preserve the properties of the input pulse in techniques such as chirped pulse amplification. Alternatively, the amplifier can change the phase structure, spectrum and temporal duration of the seed pulse; this can be beneficial if the right fibre parameters are chosen then a linearly chirped spectrally broadened pulse can be generated in a technique known as parabolic amplification.

This section aims to discuss the effects a fibre amplifier may have upon a propagating pulse train. In section 4.1 the effects of fibre structure are discussed; section 4.2 will talk about the spectroscopy of Yb-doped fibres and the gain properties of such fibre while in section 4.3 material dispersion and nonlinear effects of the fibre are described. In the final section, the technique of parabolic amplification will be introduced.

4.1 Fibre Waveguides

The most basic fibre waveguide comprises a length of cylindrical glass with refractive index n_1 surrounded by a cladding layer of refractive index n_2. Such a fibre will guide light provided that the condition $n_1 > n_2$ is met. This type of fibre will usually have a core diameter of less than 10 μm. The small size of the fibre core is chosen to ensure that only the fundamental mode of the fibre may propagate inside of the core. This is done to give the highest quality output beam with M^2 values as low as 1.1, where [1]

$$\omega_0\theta_0 = M^2\frac{\lambda}{\pi}. \tag{4.1}$$

Here ω_0 is the beam waist, θ_0 is the divergence, λ is the wavelength of the transmitted light and a value of M^2 = 1 corresponds to a diffraction limited beam. The cladding diameter is chosen to be large enough to confine the core mode which falls off exponentially inside of the cladding; a typical cladding diameter would be 125 μm.

In order to couple a light source into an optical fibre efficiently it is useful to know the brightness of the source, defined as [1]

$$B = \frac{P}{2\pi A(1-cos\theta)} \approx \frac{P}{\pi A(NA^2)}, \tag{4.2}$$

where NA = $\sqrt{n_1^2 - n_2^2}$ and the source has an area A. When coupling into the fibre the brightness of the fibre can not exceed the brightness of the source, this is summarised by the relationship [1]

$$\pi A_s sin^2(\theta) \leq \pi A_f NA^2; \tag{4.3}$$

where A_s is the area of the source and A_f is the mode area of the fibre core. Maximum coupling efficiency is achieved when the brightness of the source matches the brightness of the fibre. In the case of a single clad fibre all the light propagates inside of the fibre core which by design has a low NA of around 0.08. In the case of Yb-doped amplifiers the core is doped with ytterbium and it is necessary to couple both the pump and seed source into the core. The gain of the amplifier depends upon the amount of pump light absorbed by the ytterbium ions. This is greatly limited as single-mode sources with low NAs appropriate for pumping single-clad amplifiers are of powers typically < 1 W.

The solution to this problem is to employ a double clad fibre, where there is a secondary waveguide formed by the inner cladding, to which a high power multimode

source can easily be coupled; this arrangement is referred to as cladding pumping [2]. An example of a double clad fibre is presented in figure 4.1

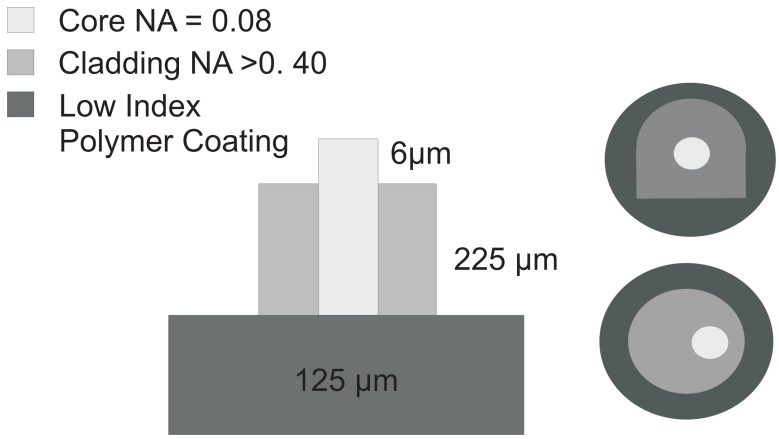

Figure 4.1: Side view of a double clad Yb-doped fibre. Two examples (right) of how the symmetry of the core/inner cladding may be broken to ensure maximum overlap of the cladding modes with the fibre core.

The double-clad fibre has a cylindrical core generally of less than 20 μm diameter, which will support a small number of fibre modes, typically just one. The inner cladding is typically 125 μm in diameter and supports a larger number of modes than the fibre core. The double-clad fibre is completed by coating in a low-index polymer; this ensures confinement of the inner cladding modes and allows for a larger NA of the inner cladding. With NA typically greater than 0.4 it is easy to couple a high power multimode source into the fibre.

To ensure efficient operation of an Yb-doped fibre amplifier it is important to maximise the absorption of the pump light within the fibre core while allowing for uniform absorption/gain along the entire fibre length. To achieve this, the overlap between fibre core and cladding modes is maximised by breaking the cylindrical symmetry of the fibre; for example by positioning the fibre core non-centrally within the inner cladding as in figure 4.1 bottom right, or by having a D shaped inner cladding as in figure 4.1 top right.

The spectroscopic properties of Yb-doped glass allow for pumping over a range of wavelengths, and will be discussed in section 4.2; for now we note that it is most common to pump at around 915 nm or near 975 nm. There are a multitude of sources available at these two wavelengths with powers up to several kW. For the work presented in this thesis, commercially available single-emitter fibre-coupled diodes were

used. The fibreised output from each diode is in excess of 5 W, while the fibre NA and core size are chosen to closely match those of the Yb-doped fibre allowing for high coupling efficiencies.

There are a number of geometries available for pumping a fibre amplifier including v-groove side pumping [3], side spliced fibre pumping [4] and end pumping. For the amplifiers described in this thesis, end pumping was chosen which allows for a simpler launch of the pump and the signal.

4.2 Spectroscopic Properties of Yb-Doped Fibre

Ytterbium-doped fibres have a broad gain bandwidth, offering amplification in the wavelength range 975 nm to 1200 nm. High doping levels can be achieved, enabling large absorption and gain per unit length. A variety of pump sources can be used at wavelengths between 860 nm and 1064 nm. The close proximity of the pump wavelength to the amplification wavelength results in a low quantum defect allowing for efficient amplification; efficiencies of around 80 % are possible.

Ytterbium ions embedded in a glass host have optical transitions between two manifolds, the excited state $^2F_{5/2}$ (which has 3 stark levels) and the ground state $^2F_{7/2}$ which has 4 stark levels. In figure 4.2 the absorption and emission cross section of Yb-doped germanosilicate glass is shown along with the energy level diagram. The transitions between Stark levels are not fully resolved for an Y^{3+} ion in a glass host at room temperature because of the effects of homogeneous and inhomogeneous broadening; these transitions result in the absorption and emission spectrum of figure 4.2 a).

The absorption cross section (solid line) of figure 4.2 a) has three peaks in it and the emission cross section has two peaks. The peak emission wavelength of the Yb^{3+} ion coincides with the peak absorption wavelength, centred at 975 nm. This peak corresponds to transitions between the lowest energy ground state and the lowest energy excited state labelled a) and e) in figure 4.2 b). The next strongest absorption peak is at 915 nm, this absorption has about a third of the strength of the 975 nm absorption, however it is considerably broader. The weakest absorption feature occurs between approximately 1000 nm and 1050 nm. This peak enables the fibre to be pumped by Nd:YAG (1064 nm) and Nd:YLF (1047 nm) lasers; but also introduces a

small, reabsorption loss for signals close to 1 μm. The weaker of the two emission peaks occurs near 1030 nm and is considerably broader than the peak at 975 nm; it is this peak that gives rise to gain for a VECSEL seed near 1040 nm.

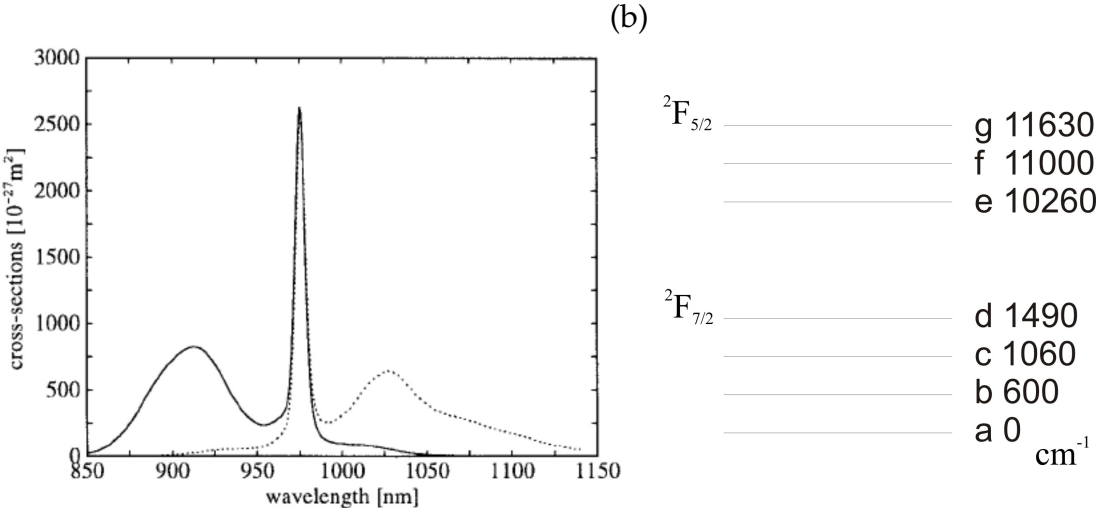

Figure 4.2: Absorption (solid) and emission (dotted) cross sections of Yb in germanosilicate glass a), taken from [5]. Energy level diagram showing the $^2F_{7/2}$ and $^2F_{5/2}$ manifolds along with the stark levels b).

The pump source must be chosen so that the wavelength of the source falls within one of the absorption peaks, it must also be at a shorter wavelength than the seed laser; for example a 1064 nm pump laser will not generate gain at 975 nm. For a particular seed wavelength the choice of pump wavelength will affect the gain and the efficiency of a particular fibre amplifier. Optimum efficiency of an amplifier occurs when the residual pump power after propagating along the entire length of the fibre is just sufficient to reach transparency that is there is zero gain at the end of the fibre; this transparency power is given by [5]

$$P_{trans} = \frac{A_c h\nu_p}{\eta_p \left(\sigma_{21}^{(s)}\sigma_{12}^{(p)}/\sigma_{12}^{(s)} - \sigma_{21}^{(p)}\right)\tau}. \tag{4.4}$$

Here A_c is the core area, $\sigma^{(s/p)}$ is the emission/absorption cross section of the signal/pump, τ is the upper state lifetime, ν_p is the pump frequency and η_p is an overlap factor characterising the fact that some of the pump will propagate in the un-doped cladding. The transparency power at various signal wavelengths is plotted in figure 4.3 for a number of pump wavelengths.

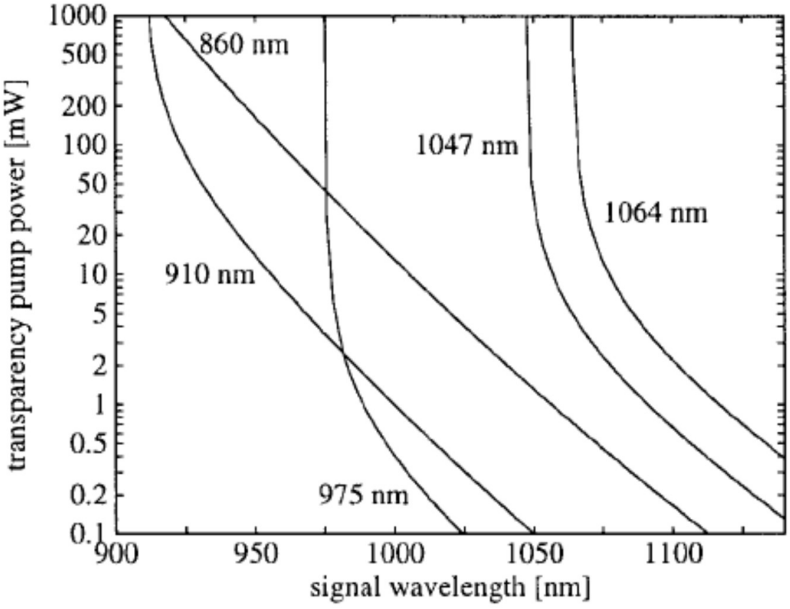

Figure 4.3: Transparancy pump power versus signal wavelength for a number of pump wavelengths taken from [5]; the data was calculated for a single clad fibre.

This shows that for a signal wavelength near 1040 nm the efficiency of the amplifier will be much the same when pumped at either 975 nm or 910 nm, however pumping at shorter wavelengths near 860 nm greatly decreases the efficiency of the amplifier. Depending upon the pump and signal intensities within the fibre core, spontaneously emitted photons will experience gain within the fibre; this process, known as amplified spontaneous emission (ASE) has the effect of reducing the gain experienced at the signal wavelength. The efficiency of pumping at 910 nm can be reduced if significant amplified spontaneous emission (ASE) occurs within the fibre, this is particularly a problem near 975 nm where there is a large emission cross section. One way of avoiding ASE at 975 nm is to use longer fibre lengths; this allows for reabsorption of low wavelength signals pushing the optimum gain of the fibre towards longer wavelengths.

4.2.1 Fibre Gain

The standard rate and propagation equations for a two level system can be used to describe the gain of an Ytterbium doped fibre amplifier [6], assuming that the system is homogeneously broadened and the fibre supports only the fundamental mode.

The upper and lower excited state populations at a particular location in the fibre can be expressed as

$$\frac{dn_2}{dt} = (R_{12} + W_{12})\, n_1 - (R_{21} + W_{21} + A_{21})\, n_2, \tag{4.5}$$

$$\frac{dn_1}{dt} = -(R_{12} + W_{12})\, n_1 + (R_{21} + W_{21} + A_{21})\, n_2. \tag{4.6}$$

It follows that the steady state excited population is given by

$$n_2 = \frac{R_{12} + W_{12}}{R_{12} + R_{21} + W_{12} + W_{21} + A_{21}}, \tag{4.7}$$

where n_1 + n_2 is taken to be equal to 1. In the previous expressions A_{21} is the spontaneous emission rate, the pump induced transitition rates $R_{ij} = \sigma_{ij}^{p} I_p / h\nu_p$ and the signal induced transitions $W_{ij} = \sigma_{ij}^{s} I_s / h\nu_s$ where, $\sigma_{ij}^{p/s}$ is the optical cross section for the relevent transition; $I_{s/p}$ is the signal/pump intensity (in W/m^2). Three more equations are needed to model the gain spectrum of the amplifier; these represent the propogation of pump (P_p), signal (P_s) and ASE (P_a) power at each position along the fibre:

$$\frac{dP_p}{dz} = \eta_p \left[\sigma_{21} n_2 - \sigma_{12} n_1\right] P_p \rho - P_p \alpha_p, \tag{4.8}$$

$$\frac{dP_s}{dz} = \eta_s \left[\sigma_{21} n_2 - \sigma_{12} n_1\right] P_s \rho - P_s \alpha_s, \tag{4.9}$$

$$\frac{dP_a}{dz} = \eta_s \left[\sigma_{21} n_2 - \sigma_{12} n_1\right] P_a \rho - P_s \alpha_a + 2\eta_s \sigma_{21} n_2 \rho_h \nu_s \Delta\nu. \tag{4.10}$$

Here $\alpha_{s/p}$ represents internal loss of the fibre for the signal and pump wavelengths and $\Delta\nu$ is the amplifier homogeneous bandwidth for both polarization states. The model asumes a constant transverse value for the pump, signal and excited population level. This is reasonabley accurate, provided that overlap factors η_p and η_s are used to account for the fact that some fraction of the power propagates inside the fibre cladding. The model first assumes a steady state by setting $\frac{dP_p}{dz} = 0$, then the propagation equations, 4.5, 4.8, 4.9 and 4.10 are solved using standard numerical techniques to obtain the inversion fraction at each point along the fibre. In this model the light in the fibre is considered as a set of discrete spectral components, of bandwidth $\Delta\nu_k$ centred at a frequency ν_k. The bandwidth $\Delta\nu_k$ is the frequency resolution of the model thus a broad bandwidth signal will be made up of many different frequency components.

4.3 Wave Propagation in Silica Fibre

The aim of this section is to discuss the propagation of an ultra-short pulse within a length of silica fibre. The pulse will induce a polarization of the atoms within the fibre, which in turn will effect the propagation of the pulse. It will be shown that the polarization has both linear and nonlinear dependence upon the E-field of the pulse. Maxwell's equations will be used to derive the nonlinear Schrdinger equation describing wave propagation in optical fibre. It will then be shown how both linear and nonlinear polarizations affect the shape of the pulse.

4.3.1 The basic wave equation

Maxwell's equations are presented in Eq(4.11 - 4.14) along with the constitutive relations (4.15 and 4.16).

$$\nabla \cdot D = P, \tag{4.11}$$

$$\nabla \cdot B = 0, \tag{4.12}$$

$$\nabla \times E = -\frac{\partial B}{\partial t}, \tag{4.13}$$

$$\nabla \times H = J + \frac{\partial D}{\partial t}, \tag{4.14}$$

where D is the electric displacement, B is the magnetic flux density, E is the electric field strength and H is the magnetic field strength. The constitutive relations relate the quantities D and B to E and H, they are:

$$D = \epsilon_0 E + P, \tag{4.15}$$

$$B = \mu_0 H + M, \tag{4.16}$$

where ϵ_0 is the vacuum permittivity, μ_0 is the vacuum permeability, P and M are the induced electric and magnetic polarizations. Since optical fibre is a nonmagnetic medium, M is equal to zero. By taking the curl of equation (4.13) and using equations 4.14, 4.15 and 4.16 it is possible to derive the wave equation

$$\nabla \times \nabla \times E = -\frac{1}{c^2}\frac{\partial^2 E}{\partial t^2} - \mu_0 \frac{\partial^2 P}{\partial t^2}, \tag{4.17}$$

where c is the speed of light in vacuum equal to $1/\sqrt{\epsilon_0 \mu_0}$. For a complete description it is necessary to relate the induced polarization P to the electric field E, in general

such an evaluation requires a quantum mechanical approach. However in the wavelength range of interest 0.5 - 2 μm, silica fibre is far from its material resonance and a phenomenological description of the polarization is valid [7],page :

$$P = \epsilon_0 \left(\chi^{(1)} \cdot E + \chi^{(2)} \cdot E^2 + \chi^{(3)} \cdot E^3 \right). \tag{4.18}$$

The linear susceptibility $\chi^{(1)}$ is the dominant term in equation 4.18. The second order term $\chi^{(2)}$ is responsible for effects such as second harmonic generation, however it is zero for materials such as silica fibre that have an inversion symmetry. Hence most of the nonlinear effects in optical fibre depend solely upon $\chi^{(3)}$. This term is responsible for third harmonic generation, four-wave mixing and nonlinear refraction. Third harmonic generation and four-wave mixing will generate new frequency components of a propagating pulse, however to have efficient conversion requires special care to ensure phase matching; hence in the following only the effects arising from the nonlinear refractive index will be considered.

The induced polarization consists of a linear and nonlinear component

$$P(r,t) = P_L(r,t) + P_{NL}(r,t), \tag{4.19}$$

where

$$P_L(r,t) = \epsilon_0 \int_{-\infty}^{+\infty} \chi^{(1)}(t-t') \cdot E(r,t')dt' \tag{4.20}$$

$$P_{NL}(r,t) = \epsilon_0 \int\int\int_{-\infty}^{+\infty} \chi^{(3)}(t-t_1, t-t_2, t-t_3) \vdots E(t-t_1)E(t-t_2)E(t-t_3)dt_1 dt_2 dt_3. \tag{4.21}$$

These expressions are valid in the electric-dipole approximation and assume that the medium response is local. Using the expression $\nabla \times \nabla = \nabla \cdot (\nabla E) - \nabla^2 E = -\nabla^2 E$ we rewrite equation 4.17 as

$$\nabla^2 E - \frac{1}{c^2}\frac{\partial^2 E}{\partial t^2} = \mu_0 \frac{\partial^2 P_L}{\partial t^2} + \mu_0 \frac{\partial^2 P_{NL}}{\partial t^2}. \tag{4.22}$$

In the next two sections this equation will be used to consider the linear and nonlinear effects upon the shape of a pulse propagating in a length of fibre.

4.3.2 Fibre Modes

By setting $P_N L$ in equation 4.22 equal to zero, we can study the linear effects of pulse propagation. These basically arise from the dispersive nature of the optical medium. It is useful to work in the frequency domain while doing this analysis; so we start by taking the Fourier transform of equation 4.22

$$\nabla^2 \tilde{E}(r,\omega) + n^2(\omega)\frac{\omega^2}{c^2}\tilde{E}(r,\omega) = 0, \tag{4.23}$$

Where $\tilde{E}(r,\omega)$ is the Fourier transform of $E(r,t)$. The frequency-dependent dielectric constant $\epsilon(\omega)$ has been replaced by $n^2(\omega)$; this amounts to ignoring the effect of optical loss within the fibre. Loss will be included later as a perturbation. The term $n^2(\omega)$ is described by the Sellmeier equation [7],

$$n^2(\omega) = 1 + \sum_{j=1}^{m} \frac{B_j \omega_j^2}{\omega_j^2 - \omega^2}, \tag{4.24}$$

where ω_j is a resonance frequency, B_j is the strength of the j_{th} resonance and the sum extends over all material resonances that contribute to the frequency range under scrutiny.

It can be shown that equation 4.23 has a general solution of the form

$$\tilde{E}_z(r,\omega) = A(\omega)F(\rho)exp(\pm im\phi)exp(i\beta z), \tag{4.25}$$

where $A(\omega)$ is a normalisation constant, β is the propagation constant, m is an integer and $F(\rho)$ is the solution of

$$\frac{d^2F}{d\rho^2} + \frac{1}{\rho}\frac{dF}{d\rho} + \left(n^2k_0^2 - \beta^2 - \frac{m^2}{\rho^2}\right)F = 0. \tag{4.26}$$

The propagation constant β is obtained by solving the eigenvalue equation [7]

$$\left[\frac{J_m'(\kappa a)}{\kappa J_m(\kappa a)} + \frac{K_m'(\gamma a)}{\gamma K_m(\gamma a)}\right]\left[\frac{J_m'(\kappa a)}{\kappa J_m(\kappa a)} + \frac{n_2^2}{n_1^2}\frac{K_m'(\gamma a)}{\gamma K_m(\gamma a)}\right] = \left(\frac{m\beta k_0\left(n_1^2 - n_2^2\right)}{an_1\kappa^2\gamma^2}\right). \tag{4.27}$$

For each value of the integer m there is generally more than one solution to the eigenvalue equation. Each solution gives a different value of β corresponding to a different mode of the fibre. The corresponding modal field distribution is given by equation 4.25. The propagation constant is responsible for linear dispersion within an optical fibre and is often expressed as a Taylor expansion about ω_0

$$\beta(\omega_0) = \beta_0 + (\omega - \omega_0)\beta_1 + \frac{1}{2}(\omega - \omega_0)^2\beta_2 + \frac{1}{6}(\omega - \omega_0)^3\beta_3; \tag{4.28}$$

where

$$\beta_m = \left(\frac{d^m \beta}{d\omega^m}\right)_{\omega=\omega_0}. \tag{4.29}$$

It should be noted that the different modes of the fibre will experience different values of optical gain as well as dispersion when the fibre is used as an amplifier. It is thus desirable to operate the amplifier in a single mode. The condition for single mode operation of a fibre is that the fibre V number be less that 2.405, where

$$V = k_0 a \left(n_1^2 - n_2^2\right)^{\frac{1}{2}}. \tag{4.30}$$

Here the term a is the radius of the fibre core and n_1 (n_2) is the refractive index of the fibre core (cladding). The fundamental fibre mode can be approximated by

$$\tilde{E}(r,\omega) = \hat{x}\left[A(\omega)F(x,y)exp(i\beta(\omega)z)\right]. \tag{4.31}$$

The transverse distribution of the field inside of the core is given by

$$F(x,y) = J_0(\kappa\rho), \rho \leq a. \tag{4.32}$$

This falls off exponentially inside the cladding;

$$F(x,y) = \left(\frac{a}{\rho}\right)^{\frac{1}{2}} J_0(\kappa a)exp\left[-\gamma(\rho - a)\right], \rho \geq a, \tag{4.33}$$

where $\rho = (x^2 + y^2)^{\frac{1}{2}}$ is the radial distance, $\kappa = (n_1^2 k_0 - \beta^2)^{\frac{1}{2}}$, $\gamma = (\beta^2 - n_2^2 k_0)$ and J_0 is the Bessel function. As a result of the fundamental mode not being zero inside the fibre cladding a propagating pulse will see a refractive index that has a component due to the cladding; this effect is known as waveguide dispersion.

4.3.3 Nonlinear Schrödinger Equation

Pulse propogation including nonlinear effects is described by the following equation [7]

$$\frac{\partial A}{\partial Z} + \frac{\alpha}{2}A + \frac{i\beta_2}{2}\frac{\partial^2 A}{\partial T^2} - \frac{\beta_3}{6}\frac{\partial^3 A}{\partial T^3} = i\gamma\left(|A|^2 A + \frac{i}{\omega_0}\frac{\partial}{\partial T}(|A|^2 A) - T_R A\frac{\partial |A|^2}{\partial T}\right). \tag{4.34}$$

This equation is the nonlinear Schrödinger equation (NLS) , its solutions describe the propagation of light through optical fibre. The term Z is longitudinal position

within the fibre and T is time. The term A is the pulse amplitude normalised such that $|A|^2$ represents the optical power. The linear loss of the fibre is described by the absorption coefficient α. Nonlinearities appear on the right hand side of equation 4.34 where the constant T_R can be related to the slope of the Raman gain spectrum and $\gamma = n_2\omega_0/cA_{eff}$. The term A_{eff} is the effective area of the fibre mode given by

$$A_{eff} = \frac{\left(\int\int_{-\infty}^{+\infty} |F(x,y)|^2 \, dxdy\right)^2}{\int\int_{-\infty}^{+\infty} |F(x,y)|^4 \, dxdy}, \tag{4.35}$$

while n_2 is the intensity dependent refractive index given by

$$n_2 = \frac{3}{8n} Re(\chi^3_{xxxx}). \tag{4.36}$$

A pulse entering a length of optical fibre will experience a number of effects, causing its shape to change in the time and frequency domains depending upon the relative strengths of the terms in equation 4.34. These effects are discussed in the next two sections.

4.3.4 Linear Propagation

The different frequency components of an optical pulse propagating within a length of optical fibre will propagate at different velocities due to the dispersive nature of the glass. Dispersion is accounted for by the β_2 and β_3 terms in equation 4.34. The β_2 term gives rise to group velocity dispersion (GVD). This will cause a change in phase of the spectral components of the pulse; it does not affect the spectrum of the pulse, but does alter the pulse duration. The change in pulse length depends upon the initial pulse duration T_0 and the propagation length. In the case of a Gaussian pulse, the pulse length after propagating a distance z along an optical fibre is

$$T_1(z) = T_0 \left[1 + \left(\frac{z\,|\beta_2|}{T_0^2}\right)^2\right]^{\frac{1}{2}}. \tag{4.37}$$

The pulse with increased temporal duration is now said to be linearly chirped; being upchirped if β_2 is positive and down if β_2 is negative. The relation in equation 4.37 assumed that the pulse T_0 was unchirped. If it had, for example, been upchirped by passing through a length of fibre with β_2 = + a, it would then be compressed in time, back to its original duration by passing through an equal length of fibre with β_2 = - a;

this technique is referred to as dispersion compensation. At 1 μm the fibre introduces negative dispersion to the pulse.

The β_3 term is generally much weaker than the β_2 term. It gives rise to third order dispersion (TOD), which will again distort the pulse in the time domain. This distortion causes the pulse to become asymmetric in the time domain with an oscillatory structure near one of its edges; this will be the trailing (leading) edge for positive (negative) β_3.

4.3.5 Nonlinear Propagation

Under intense excitation by an electric field the induced polarisation will have a nonlinear response and the γ term in equation 4.34 will be nonzero. The nonlinear effects that arise in optical fibre can be divided into two categories. The first set of effects are elastic, thus energy is not exchanged between the pulse and the atoms of the fibre. Such effects include self-phase-modulation (SPM), cross-phase-modulation (XPM) and third harmonic generation and four-wave mixing. For the fibre amplifiers described in this thesis the only elastic effect that need be considered is SPM.

SPM arises as a result of the intensity dependence of refractive index. It introduces an intensity-dependent phase shift to an optical pulse. This phase shift in turn introduces new spectral components to the pulse. The magnitude of the spectral broadening increases with propagation length. The resulting spectrum is broader with an oscillatory structure covering the entire frequency range. These oscillations arise because the chirp induced by the SPM ($\frac{d\phi}{dt}$) varies linearly across the pulse it will in general have the same value at two points across the pulse. At these two points the pulse will have the same instantaneous frequency. It is the interaction of these two points that creates the oscillatory nature of the SPM broadened spectra, examples of which are depicted in figure 4.4 for different sized phase shifts.

The second class of nonlinear effects involve inelastic scattering, where energy is exchanged between the dielectric lattice and the electric field of the pulse in the form of phonons. Two such effects are stimulated Raman scattering (SRS) and stimulated Brillouin scattering (SBS); the latter is not considered in this thesis as it only has a large gain for very narrow excitation bandwidths. An optical wave travelling along a length of fibre can act as a pump source for the SRS. The effect removes a fraction of the light (approximately 10^{-6}) from the pump at a frequency ω_p and creates a Stokes

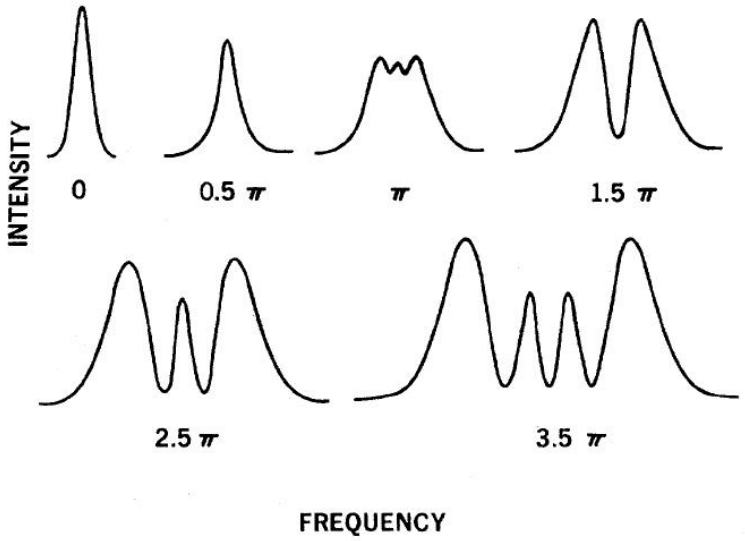

Figure 4.4: SPM-broadend spectra for an unchirped Gaussian pulse taken fron [7]. Spectra are labeled, showing the maximum nonlinear phase shift ϕ_{max}.

wave at another frequency ω_s. The effect has a gain bandwidth $g_R(\Omega)$ of around 40 THz depending upon the exact composition of the fibre core. The new frequency $\omega_s = \omega_p \pm \Omega$ is created by exchanging a phonon between a pump photon and the fibre lattice, where the energy of the phonon satisfies the equation $\hbar\nu$. The new wave is referred to as a Stokes (anti-Stokes) if the pump photon looses (gains) energy in the interaction. The anti-Stokes wave is rarely observed in optical fibre as the Stokes wave has a much higher gain; the latter will propagate in the same direction as the pump wave. For the fibre amplifier configurations discussed in this thesis, the parasitic loss associated with SRS will be insignificant compared to the effect of ASE.

4.4 Parabolic Amplification

When designing a fibre amplifier it is important to consider the relative size of the various dispersive effects of the fibre. This can be done by defining two length scales over which the pulse must propagate before the linear and nonlinear dispersive effects become significant,

$$L_D = \frac{T_0^2}{\beta^2}, \tag{4.38}$$

$$L_{NL} = \frac{1}{\gamma P_0}. \tag{4.39}$$

Where P_0 is the peak power of the pulse at the start of the fibre. For fiber lengths greater than L_D linear dispersive effects become important, while L_{NL} is the minimum length of fibre required for nonlinear effects to become important.

In the following chapters two regimes of amplification will be demonstrated, in chapter 5 an amplifier is designed so that the fibre length $L \leq L_D$ and $L \ll L_{NL}$; in this regime the nonlinear effects are negligible and only linear dispersion will affect the pulse. In chapter 6 a second regime is considered where the fibre length is greater than both L_D and L_{NL}, it is the aim of this section to demonstrate that under the correct operating conditions the linear dispersion and nonlinear effects of the fibre cooperate to produce a spectrally broadened linearly chirped amplified pulse; this technique is referred to as parabolic amplification.

Parabolic pulse propagation has been demonstrated in normal fibre without gain, in fibre amplifiers [8, 9] and in fibre lasers [10]. After propagating along a length of normally dispersive fibre the pulse will have evolved to have a parabolic intensity profile, this profile has been demonstrated to be maintained after propagating in additional lengths of normally dispersive fibre without gain [11]. The length of fibre required to reach the parabolic regime depends upon the peak power of the input pulse and the fibre parameters gain (g), β_2, and γ; the form of the gain profile has been shown to determine the scaling of the pulse as it propagates [12].

Kruglov et al. have used self-similarity analysis of the nonlinear Schrödinger equation to derive equations for designing a fibre amplifier to produce parabolic pulses [13]. To achieve this Kruglov et al. first reduce the number of degrees of freedom by rewriting the nonlinear Schrödinger equation in terms of the following variables:

$$A(z,T) = f(z)F(z,T) = f(z)F(\vartheta), \tag{4.40}$$

$$\Phi(z,T) = \varphi(z) + C(z)T^2, \tag{4.41}$$

$$\vartheta = f^2(z)exp(-gz)T. \tag{4.42}$$

$$\tag{4.43}$$

Solutions to the NLS of the form $\Psi(z,T) = A(z,T)exp[i\Phi(z,T)]$ may then be found in the limit $z \to \infty$. In the above equations the term $f(z)$ describes the evolution of the peak amplitude of the pulse with propagation distance and has the same dimensions

as $\Psi(z,T)$. $F(\vartheta)$ is a normalised, dimensionless function that describes the temporal profile of the pulse. The phase term $\Phi(z,T)$ contains the z-dependent phase offset $\varphi(z)$ and chirp parameter $C(z)$. The term ϑ is the self-similarity variable [13] where g is the gain of the fibre.

For a particular fibre amplifier where g, β_2, and γ are fixed, the rate at which an input pulse evolves towards the parabolic regime will depend upon the peak power of the input pulse alone; there exists an optimum pulse length for the fastest evolution into the parabolic regime given by

$$T_0 = \frac{6\sqrt{\gamma\beta_2/2A_0}}{g}, \tag{4.44}$$

where

$$A_0 = \frac{1}{2}\left(\frac{gU_{in}}{\sqrt{\gamma\beta_2/2}}\right) \tag{4.45}$$

In the above equation U_{in} is the initial pulse energy before entering the fibre amplifier. If this pulse duration is unobtainable then it is still possible to optimise the evolution by altering the pulse energy, the optimum pulse energy for fixed pulse duration is given by

$$U_{in}^{opt} = \frac{2T_0^3 g^2}{27\gamma\beta_2}. \tag{4.46}$$

Kruglov et al. have also derived an equation for the characteristic length required to reach the parabolic regime within a particular fibre amplifier:

$$z_c(N) = \frac{3}{2g} ln\left(\frac{Ng}{6\left|\gamma\right| A_0^2}\right). \tag{4.47}$$

Here the pulse is thought to be close to the parabolic regime at $z \geq z_c(N)$ for large values of N. It is reported in [13] that "simulations indicate pulse propogation well into the parabolic regime for values of $N > 100$", where $N^2 = G|_{T=0}$ and

$$G = \frac{\left|\gamma F^2\right|}{\left|\frac{\beta_2}{2F}\frac{d^2F}{d\vartheta^2} f^2 exp(-2gz)\right|} \tag{4.48}$$

The above expression appears in [13] to justify the simplifications used to derive equations 4.44 - 4.47 and will not be discussed any further in this thesis.

In designing an amplifier to operate in the parabolic regime the fibre length must be made greater than z_c and the seed pulse should be adjusted to be as close as possible to the optimum pulse energy/duration. Finally we note that the output power

of existing amplifiers operating in the parabolic regime has been limited to tens of watts, due to the finite gain bandwidth of Yb-doped amplifiers.

4.5 References

[1] P. Dupriez. *Advanced Pulsed High Power Laser Systems And Their Applications*. PhD thesis, University of Southampton, 2007.

[2] J. Kafka. "Laser Diode Pumped Fiber Laser With Pump Cavity US Patent 4829529", 1989.

[3] D. J. Ripin and L. Goldberg. "High efficiency side-coupling of light into optical fibres using imbedded v-grooves". *Electronics Letters*, 31(25):2204–2205, 1995.

[4] V. P. Gapontsev and I. Samartsev. "Coupling Arrangement Between A Multi-Mode Light Source And An Optical Fibre Through An Intermediate Optical Fibre Length". *US Patent*, pages 5,999,673, 1996.

[5] R. Paschotta, J. Nilsson, A. C. Tropper, and D. C. Hanna. "Ytterbium-doped fiber amplifiers". *Quantum Electronics, IEEE Journal of*, 33(7):1049–1056, 1997.

[6] F. He, J. H. Price, K. T. Vu, A. Malinowski, J. K. Sahu, and D. J. Richardson. "Optimisation of cascaded Yb fiber amplifier chains using numerical-modelling". *Opt. Express*, 14(26):12846–12858, 2006.

[7] P. Agrawal, G. *Nonlinear Fiber Optics*. Academic Press, 2001.

[8] P. Dupriez, C. Finot, A. Malinowski, J. K. Sahu, J. Nilsson, D. J. Richardson, K. G. Wilcox, H. D. Foreman, and A. C. Tropper. "High-power, high repetition rate picosecond and femtosecond sources based on Yb-doped fiber amplification of VECSELs". *Optics Express*, 14(21), 2006.

[9] Jens Limpert, T. Schreiber, T. Clausnitzer, K. Zllner, H. Fuchs, E. Kley, H. Zellmer, and A. Tnnermann. "High-power femtosecond Yb-doped fiber amplifier". *Opt. Express*, 10(14):628–638, 2002.

[10] F. Ilday, J. R. Buckley, W. G. Clark, and F. W. Wise. "Self-Similar Evolution of Parabolic Pulses in a Laser". *Physical Review Letters*, 92(21):213902, 2004.

[11] M. E. Fermann, V. I. Kruglov, B. C. Thomsen, J. M. Dudley, and J. D. Harvey. "Self-Similar Propagation and Amplification of Parabolic Pulses in Optical Fibers". *Physical Review Letters*, 84(26):6010, 2000.

[12] V. I. Kruglov, A. C. Peacock, J. M. Dudley, and J. D. Harvey. "Self-similar propagation of high-power parabolic pulses in optical fiber amplifiers". *Opt. Lett.*, 25(24):1753–1755, 2000.

[13] V. I. Kruglov, A. C. Peacock, J. D. Harvey, and J. M. Dudley. "Self-similar propagation of parabolic pulses in normal-dispersion fiber amplifiers". *J. Opt. Soc. Am. B*, 19(3):461–469, 2002.

Chapter 5

High Repetition Rate Ytterbium Doped Fibre Amplifier

In this section the amplification of VECSEL pulses is demonstrated in single stage Yb-doped fibre amplifiers. The amplifier has been designed to minimise the effects of material and nonlinear dispersion upon the pulse train, preserving the desirable properties of the VECSEL including pulse length, while increasing the average power of the pulse train to over 1.5 W.

5.1 High Repetition Rate Laser Sources

Increasing the repetition rate of a laser source has the seemingly undesirable effect of reducing the peak power of the laser pulse. However, there are applications that benefit from a high repetition rate source; the term high repetition rate is confusingly used in the literature to refer to sources operating from 100 KHz to in excess of 1 THz. One application that benefits from a high repetition rate, is thermally inducing optical changes in glasses. In this application a pulsed source is focussed within the glass and nonlinear absorption used to produce localised heating; the energy absorbed per pulse thus depends upon peak power, while the rate of thermal heating depends upon repetition rate. This technique has been demonstrated at up to 25 MHz with 5 nJ pulses [1]. However, the benefit of increasing the repetition rate to the GHz regime has not been investigated.

At a repetition rate of about 0.3 GHz, the cavity round trip time of the VECSEL is of the same order as the lifetime of the quantum well gain making any further reduc-

tion in repetition rate difficult. The remainder of this section will thus concentrate on sources for applications requiring multi GHz repetition rates. Possible applications include the pumping of parametric amplifiers [2], optical clocking of integrated circuits [3], generating frequency combs [4] and optical sampling [5].

The highest repetition rates for a solid state laser have been achieved with the Nd:YVO_4 laser, which has been used to generate pulses with duration 2.7 ps, centred around 1064 nm, at a repetition rate of 157 GHz [6]. At 156 GHz the free spectral range of the cavity is equal to 60 % of the FWHM gain bandwidth of the crystal; thus setting an upper limit to the repetition rate of such lasers. Nd:YVO_4 lasers can operate at high powers; for example 2.1 W has been demonstrated at 10.3 GHz [6]. The pulse length of such lasers is limited to around 1 ps and is typically much longer. Another problem arises at high repetition rates, to avoid the laser's susceptibility to Q-switched mode-locking it is necessary to keep the mode area within the gain as small as possible. This means that the pump source must have a high beam quality to pump the laser, the highest repetition rates have thus been achieved using a Ti:sapphire laser as the pump source.

OPO conversion of a Nd:YVO_4 source operating at 81.8 GHz from 1064 nm to 1569 nm has been demonstrated [7]. This source was tuneable from 1541.4 to 1592.2 nm. In this work it was first, necessary to increase the output power using an Yb-doped fibre amplifier. This technique could be employed with VECSELS operating around 1 μm to gain access to telecoms wavelengths.

Shorter pulse lengths and broader bandwidths are obtainable with other solid state lasers. An 80-fs pulse train at 4 GHz repetition rate, has been demonstrated using a Cr^{4+}:YAG laser [8] operating near 1.5 μm; however, the mode-locking was not self starting. The Ti:sapphire laser has the broadest gain bandwidth of any solid state laser and has produced the shortest pulses. Operation of Ti:sapphire laser at GHz repetition rates is of particular interest for generating frequency combs, where pulses with an octave-spanning bandwidth are required. The higher repetition rate makes the frequency modes more easily resolvable, as each mode has more energy and there will be a greater spacing in frequency between modes. Ti:sapphire lasers have been demonstrated at 1 GHz [9] with an octave spanning bandwidth directly from the oscillator and average power of 900 mW. The highest repetition rate achieved with a Ti:sapphire has been 10 GHz [10] at an average power of 1 W; however, this source re-

quired spectral broadening inside a photonic crystal fibre to reach an octave in bandwidth.

The sources presented so far have all been fundamentally mode-locked, harmonic mode locking is an alternative approach to achieving high repetition rates. This technique is commonly employed in fibre lasers where the fundamental repetition rate of the laser is limited to a few hundred MHz. Harmonic mode locking exploits the fact that fibre lasers will produce multiple pulses when pumped above a certain threshold. When these pulses are equally spaced, the laser is said to be harmonically mode locked. The repetition rate of such a laser is equal to the number of pulses inside the fibre times the free spectral range of the cavity.

Passive harmonic mode locking has been used to produce transform limited 500 fs pulses with an Yb-doped fibre laser at a repetition rate of 1.5 GHz [11]. This source had a relatively large pulse-to-pulse timing jitter of 6 ps. Harmonic mode locking can also be exploited in actively mode-locked lasers. An active harmonically mode-locked, erbium doped fibre laser has been demonstrated with a repetition rate of up to 200 GHz [12]. Harmonically mode-locked fibre lasers are prone to pulse drop out and produce spectra with additional features such as sidebands [13]. The highest repetition rates have been achieved with harmonically mode-locked Distributed-Bragg-Reflector (DBR) lasers. Up to 1.54 THz has been generated with sub picosecond pulse duration [14]; however the average power was limited to about 15 mW and the pulse spectrum was not as smooth as those obtained with a VECSEL.

The combination of VECSEL and YDFA offers a compact, cheap source of sub picosecond pulses over the wavelength range 1 - 1.1 μm, with high average powers and at high repetition rates. High power VECSEL YDFAs have been demonstrated by P.Dupriez et.al [15] at repetition rates of 1 GHz. In this work, pulses from two different VECSELs were amplified in cascaded ytterbium doped fibre amplifiers. Amplification was demonstrated in an SPM dominated regime producing over 200 W of average power and in the parabolic pulse regime with an average power of 52 W. Pulses produced in the parabolic regime had a linear chirp enabling compression down to 110 fs. The demonstration of these techniques in simpler, single stage amplifiers at higher repetition rates would provide an alternative to the sources discussed in this section.

5.2 Design of the VECSEL Seed

Two different VECSELs were used as seed lasers in these experiments with repetition rates of 1 GHz and 6 GHz. In both the 1 GHz and the 6 GHz lasers the gain chips were pieces taken from the same wafer of QT1544 and the SESAMs were pieces of QT1627; the structure of both the gain and the SESAM have been discussed in section 2.2. The design considerations and performance of the 1 GHz z-cavity have already been discussed in chapter 2. In this section I will describe the construction of a 6 GHz v-cavity as such cavities have been used with VECSELs up to repetition rates of 50 GHz [16]. In figure 5.1 the arrangement of the 6 GHz cavity is shown.

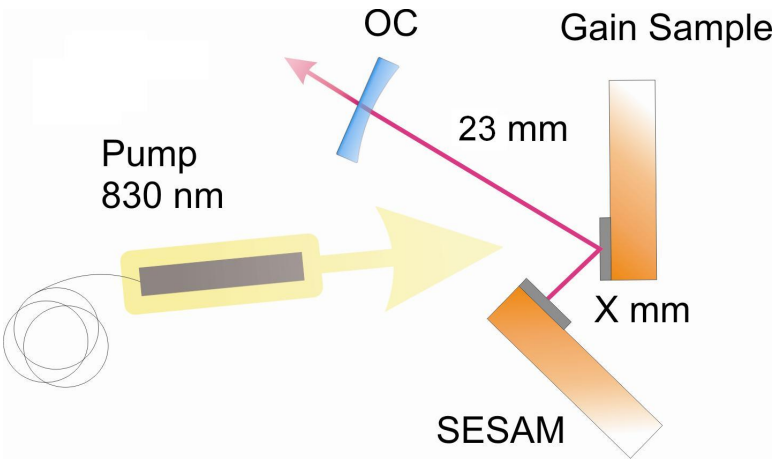

Figure 5.1: A 6 GHz v-cavity. OC: 25 mm radius of curvature output coupler; X: is a variable separation between SESAM and gain chip.

In this cavity the gain chip acts as a turning mirror enabling a double pass upon the gain, while the SESAM acts as an end mirror. The gain chip was angle polished before being bonded, with silver paint, to a water-cooled copper heat sink. Temperature tuning of the laser's peak gain wavelength was enabled by controlling the temperature of the heat sink, using a Peltier. The SESAM was bonded to a separate copper heat-sink; the temperature of this heat-sink was not actively controlled. An 830 nm fibre coupled pump diode was used to pump the gain chip providing up to 1.3 W in a 60 μm radius spot.

The total length of the cavity was less than 25 mm. The output coupler was positioned approximately 23 mm away from the gain chip allowing for a cavity mode of approximately 60 μm upon the gain, matching the size of the pump spot. Both the gain and the SESAM were mounted upon x,y,z stages, this allowed for different re-

gions of the gain to be pumped by translating the gain (without changing the cavity length), while the separation labelled 'x' between the SESAM and the gain chip could be adjusted for stable mode locking. To achieve stable mode locking it is necessary to satisfy the condition in equation 2.13:

$$\frac{E_{sat,a}}{E_{sat,g}} = \frac{F_{sat,a}A_a}{F_{sat,g}A_g} << 1. \tag{5.1}$$

To this end the cavities are aligned such that the cavity mode forms an approximately 60 μm radius spot upon the gain and a smaller spot < 15 μm radius upon the SESAM.

The dependence of the cavity mode size upon the relative positions of gain chip and SESAM is shown in figure 5.2a and 5.2b as functions of 'x' and the total cavity length respectively. The two shaded areas are regions of stability over which equation 5.1 is satisfied and mode matching with the pump spot is sufficient for lasing. It can be seen that the length of the cavity can be changed over a range < 0.02 mm. This combined with the short length of the cavity makes the 6 GHz laser more sensitive to small changes in cavity length than the 1 GHz cavity where equation 5.1 is satisfied for translations of the SESAM over a length range of approximately 2 mm. The output characteristics of this source will be discussed later along with those of the 1 GHz laser.

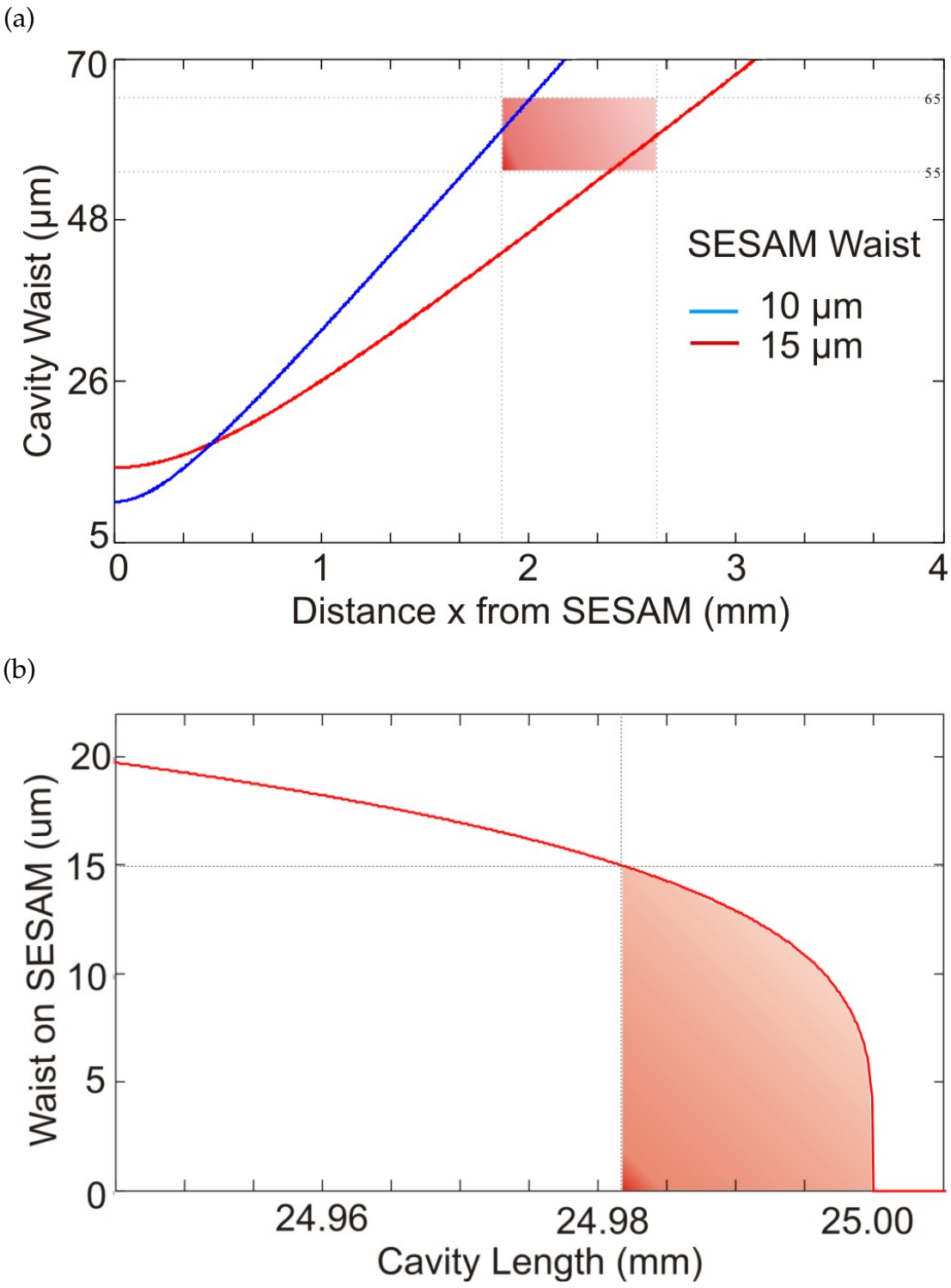

Figure 5.2: Stability curves for the 6 GHz cavity. (a) Cavity mode upon the gain for a fixed cavity length 24.99 mm as a function of X, (b) cavity waist upon SESAM as a function of the total cavity length.

5.3 Amplifier Design

The amplifier system described in this work allows for the average power of a Stark-effect-mode-locked VECSEL to be increased from around 40 mW to over 1.5 W while maintaining the good pulse characteristics of the VECSEL, including pulse length. To do this a short length of fibre was used to reduce the effect of material dispersion upon the temporal length of the amplified pulses. The fibre had a relatively large 20 μm core, which reduces the peak power within the fibre core and helps to suppress unwanted nonlinear effects such as self phase modulation (SPM). The large core increases the overlap with the cladding modes and enables more ytterbium ions to be incorporated into the fibre; this increases the gain of the amplifier, allowing for a reduction in GDD by using shorter lengths of fibre. The fibre had a V-number of 4.23 at 1040 nm; to ensure operation in a single spatial mode a bend radius of 20 cm was introduced into the fibre. The arrangement of the amplifier can be seen in figure 5.3.

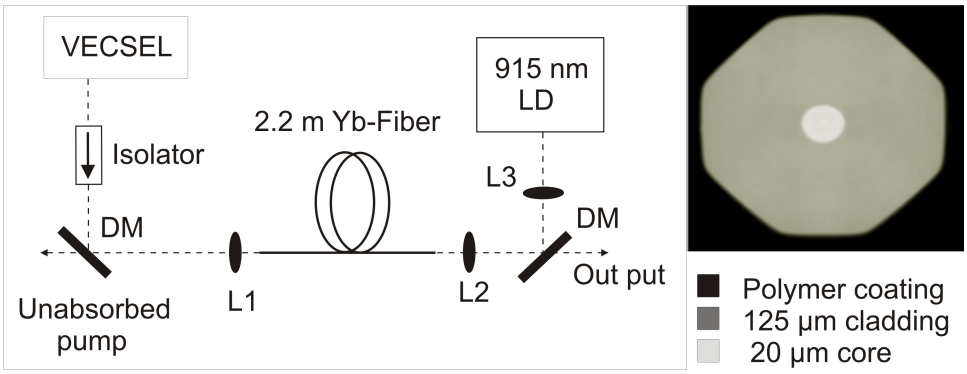

Figure 5.3: Arrangement of the fibre amplifier. DM: dichroic mirror, rflects at 915 nm and transmitting around 1040 nm; L1 and L3: focal length 4.5 mm lenses with 0.45 NA; L2: focal length 8 mm lens with 0.5 NA; LD: 5.5 W laser diode for pumping of the fibre at 915 nm.

The fibre had a 20 μm cylindrical core with a low NA of 0.07. The inner glass cladding had a diameter of 125 μm and NA > 0.46. The inner cladding was octagonal shaped to ensure maximum overlap of the cladding modes with the fibre core. A 245 μm thick low index polymer coating (not shown in figure 5.3) ensured confinement of the cladding modes while protecting the fibre from damage. The amplifier was cladding pumped by a 5 W fibre coupled diode emitting around 915 nm. In the arrangement of figure 5.3 between 4 and 5.2 W of pump light was incident upon the

end of the fibre as the dichroic mirror was less than 95 % reflective at 915 nm; it had a 90 % transmission around 1040 nm.

An important parameter affecting the operation of a fibre amplifier is the coupling efficiency of the pump and the seed into the fibre. The fibre output of the pump diode had a diameter of 100 μm and NA of 0.2, it was thus estimated from equation 3.3 that the maximum obtainable coupling efficiency of the pump into the fibre cladding should be close to 100 % while it should be around 1 % for the seed into the fibre core. These values were however lower in practice due to overfilling of the lenses.

Two techniques were employed to estimate the maximum power obtainable from the fibre amplifier; the output of the fibre could be modelled for different incident pump and seed powers using free software provided with the fibre (Liekki application designer 3.2). The modelling results can be seen in figure 5.4. The software assumes that 100 % of the pump/seed is coupled into the fibre. The user specifies the type of Liekki fibre being used along with the amplifier configuration including pump/cw-seed wavelengths and intensities. The program then returns power values for ASE, residual pump and amplified signal for both ends of the fibre. In figure 5.4 a) the output power of a 2.2 m length of Liekki fibre has been calculated for various cw-seed powers at 1042 nm, with a constant pump power coupled into the fibre of 4 W; the seed source is assumed to be monochromatic. In figure 5.4 b) the pump power has been varied between 3 and 10 W for three different seed powers coupled into the fibre. The two graphs show that for the available pump and seed powers we should expect to get between 1.1 and 2 W of average power after amplification.

The second technique employed to estimate the power obtainable with the amplifier setup of figure 5.3 was to create a fibre laser from 2.3 m of Liekki fibre. The configuration of the fibre laser was the same as for the amplifier, figure 5.3, with no seed light coupled into the fibre. Feedback was provided by the partial reflections at the two, plane cleaved, ends of the fibre. The total output from both ends of this fibre with 4 W of incident pump was measured to be 1.7 W, this includes the residual pump power measured to be around 300 mW. From this we estimate that the fibre amplifier should operate at around 1.4 W. After this measurement the laser was converted to an amplifier by angle cleaving the input end of the fibre.

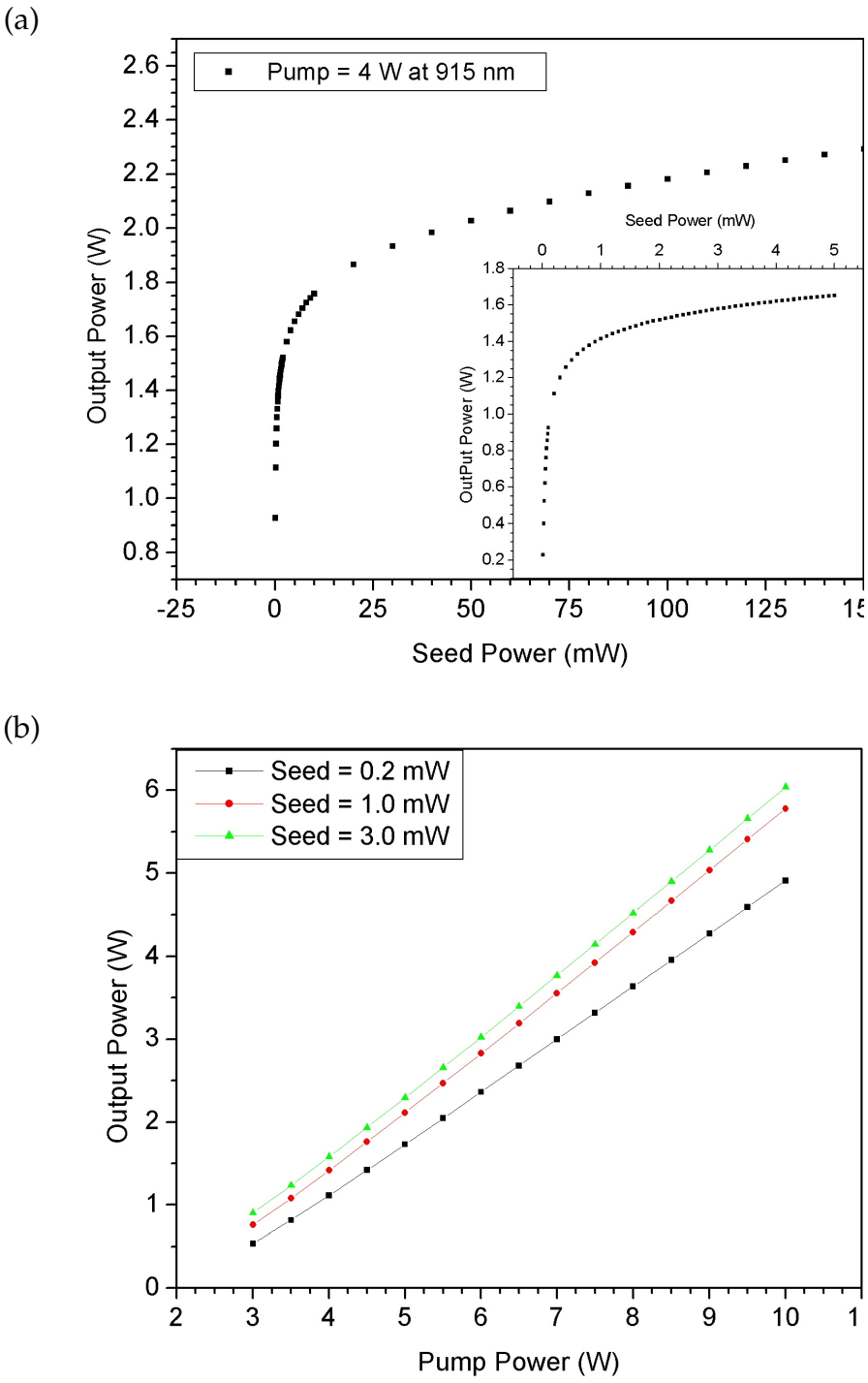

Figure 5.4: Liekki modelling results of a 2.2 m long fibre amplifier with cw seed at 1042 nm. (a) constant pump of 4 W, (b) variable pump for three fixed seed powers of 0.2, 1 and 3 mW. All powers are those coupled into the fibre (not the incident power).

Two spectra of the output from one end of the fibre laser are shown in figure 5.5, with the laser operating just below and slightly above threshold. The peak of the laser wavelength corresponds to the peak gain of the fibre and is at 1037.5 nm. In order to reduce competition between lasing close to 1037.5 nm and amplification around 1045 nm, the fibre was angle cleaved at the input end of the seed; this greatly raises the laser threshold of the fibre increasing the efficiency of amplification.

Finally, an optical isolator was used between the VECSEL and the amplifier to prevent any light from the amplifier coupling into the VECSEL; this feedback was observed to be sufficient to disturb the stable mode-locking of the VECSEL despite the high-Q of the cavity.

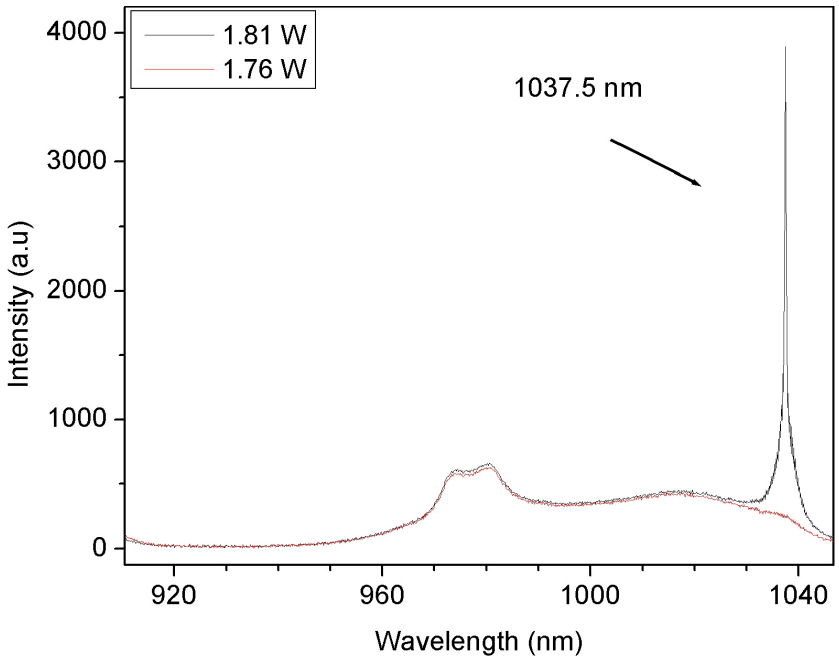

Figure 5.5: Laser spectra for 2.3 m of large core Yb-doped fibre for two different pump powers: 1.81 W (black curve) fibre lasing just above threshold, centre wavelength is 1037.5 nm; 1.76 W (red curve) showing only the ASE as the fibre is just below the laser threshold.

5.4 Fibre Amplifier Output Characteristics with a 1 GHz Seed

In order to characterise the effect of amplification upon the VECSEL pulse train, spectra and autocorrelations of the pulse train were recorded before and after the fibre; the average power of the seed and amplified pulse train was also measured. The 1 GHz seed operated with a threshold of 640 mW and had an average power, measured after the isolator, of 20 mW when pumped with 1.3 W. The pulse train was centred at 1042.3 nm with a bandwidth of 3.2 nm, measured as the full width at half maxima of the spectrum in figure 5.6 a).

The spectrum before amplification was slightly asymmetric with a tailing edge towards longer wavelengths. The modulations in the spectra are evenly spaced and can be attributed to reflections from the back of the gain chip; these modulations can be removed by angle polishing the substrate of the gain chip, so that any light reflected from the substrate will not be coupled back into the cavity mode. This was not attempted with the 1 GHz chip but is demonstrated in the next section with the 6 GHz laser. The pulse train had a temporal duration of 460 fs, this means that the pulses before amplification were 1.29 times transform limited; this assumes a sech squared fit to the autocorrelation in figure 5.6 b).

After amplification the average power of the pulse train had increased to 1.61 W, this number includes some ASE. The amplified spectrum, figure 5.6 c), shows a decrease in bandwidth of 0.17 nm, the centre wavelength has also shifted to a shorter wavelength of 1041.51 nm, while the overall shape of the spectrum is the same as before amplification including the modulations from the substrate reflections. Using the spectrum in figure 5.6 e) it is estimated that the amplified pulse train accounts for more than 98.8 % of the power measured after amplification; the residual ASE contributing less than 19.32 mW to the measured power.

The temporal width of the amplified pulse train has increased slightly to 510 fs, this is assuming a sech squared fit to the autocorrelation in figure d). The amplified pulse train has a feature present either side of the main peak in the autocorrelation; these wings are also present with the seed source and can be seen more clearly in figure 5.6 d), from which it is estimated that less than 5 % of the pulse energy is in these wings.

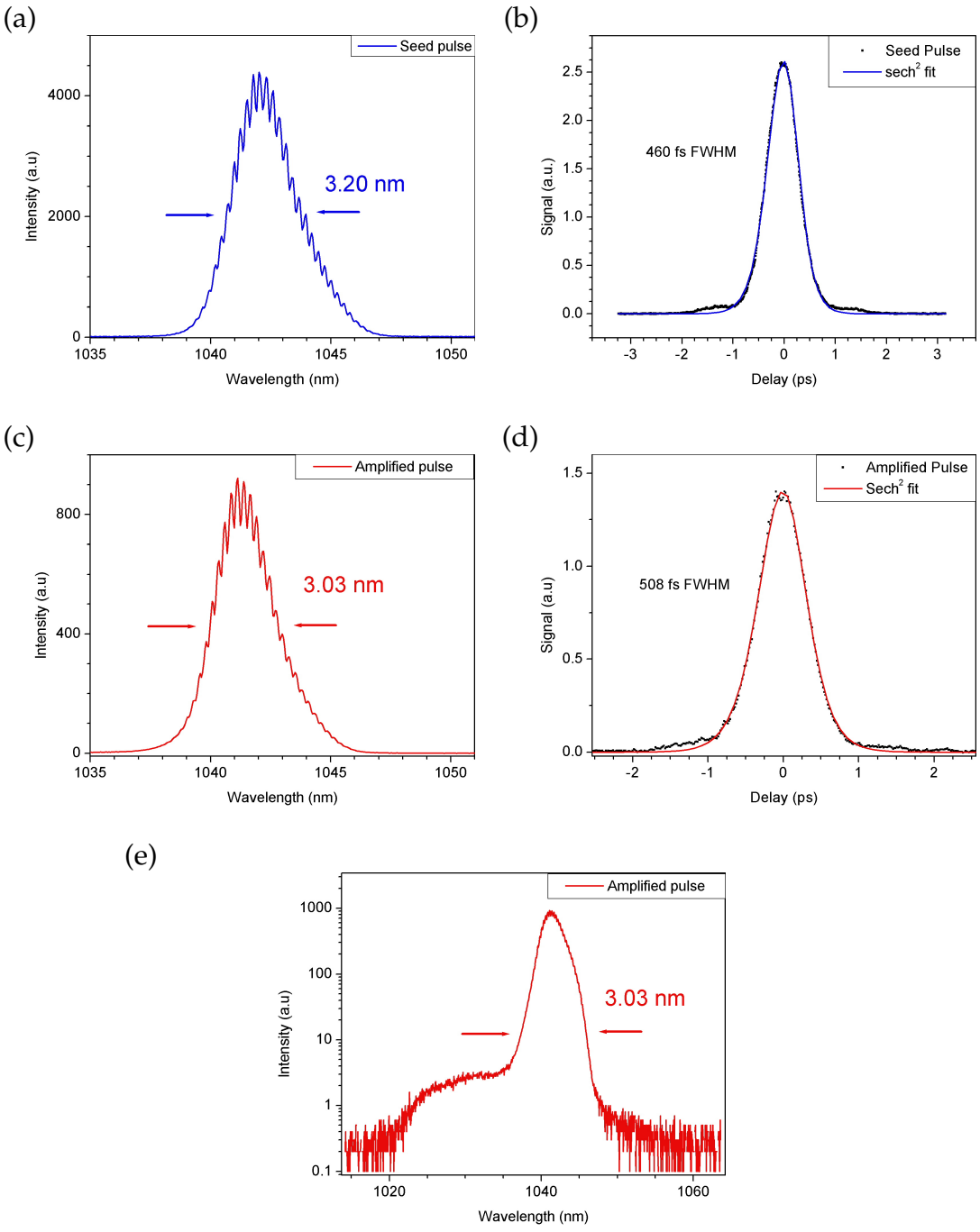

Figure 5.6: Amplifier results with a 1 GHz VECSEL seed: (a) seed spectrum; (b) autocorrelation of VECSEL seed including a sech^2 fit; (c) amplified spectrum; (d) autocorrelation of amplified pulse train; (e) log plot of amplified spectrum showing residual ASE. The modulations present in both the amplified and seed spectra are due to substrate reflections within the VECSEL.

Summarising these results, the average power of the 1 GHz pulse train has been increased by 19 dB while maintaining the pulse shape in the time and frequency domain; this suggests the absence of nonlinearities and higher order dispersion. The amplified pulse energy was 1.59 nJ and the peak power was 2744 W. The time-bandwidth product of the pulse train increased despite a reduction in spectral bandwidth. The reduced bandwidth is caused by gain filtering, while the increased chirp can be attributed to linear material dispersion.

If any spectral changes to the pulse caused by amplification are ignored, it is possible to estimate the amount of material dispersion experienced by the pulse in the following way. We assume that the seed pulse is initially linearly chirped and that this chirp arose from passing through a material of length z, which has the same value of $|\beta_2|$ as the fibre. In this way we should be able to obtain two values for the possible GVD of the fibre depending upon the initial sign of the chirp of the pulse. If β_2 is positive before amplification, then the pulse will be compressed as it propagates along the fibre which has a negative β_2 until it reaches its transform limited duration after a distance equal to z; from this point onwards the pulse will start to lengthen in time. However, if β_2 is negative before amplification then the pulse will continue to lengthen in time along the entire length of the fibre.

Using equation 4.37, two expressions are obtained for the length of a transform limited pulse T_0 after passing through a length of material of thickness z or L $\pm$ z.

$$T_1^2 = T_0^2 \left[1 + \left(\frac{z}{L_D} \right)^2 \right], \tag{5.2}$$

$$T_2^2 = T_0^2 \left[1 + \left(\frac{L \pm z}{L_D} \right)^2 \right]. \tag{5.3}$$

Here L is the fibre length equal to 2.2 m, T_1 is the initial length of the seed pulse, T_2 is the length of the amplified pulse train, $L_D = T_0^2 / |\beta_2|$ and T_0 is the bandwidth limited duration of the seed pulse equal to $T_1/1.29$. In the above equation all the pulse lengths are given as the half-width at 1/e intensity, where $T_{FWHM} = 2(ln2)^{\frac{1}{2}} T_{HW}$. Equations 5.2 and 5.3 can be rearranged to give two expressions for L_D which we equate to give

$$z^2 \left(\frac{T_1^2}{T_0^2} - 1 \right)^{-1} = (L \pm z)^2 \left(\frac{T_2^2}{T_0^2} - 1 \right)^{-1}. \tag{5.4}$$

When this equation is solved, a value of 0.975 m is obtained for z. Equation 5.3 can

be rearranged to give the following expression for $|\beta_2|$:

$$\left|\beta^2\right| = T_0^2 \left(\frac{T_2^2}{T_0^2} - 1\right)^{\frac{1}{2}} (L \pm z)^{-1}. \tag{5.5}$$

Using z = 0.975 m, equation 5.5 yields two possible values, either $|\beta_2|$ equals $14.66 \times 10^{-3} ps^2 m^{-1}$ or $37.98 \times 10^{-3}\ ps^2/m$. Liekki do not provide any information on the material dispersion of their fibre, however, these calculated values are consistent with values used for modelling pulse propagation in Yb-doped fibre around 1 μm of $25 \times 10^{-3}\ ps^2/m$ [17].

5.5 Fibre Amplifier Output Characteristics with a 6 GHz Seed

In this section amplification at a higher repetion rate is demonstrated using a 6 Ghz seed. The 6 Ghz VECSEL produced a train of pulses with a slightly broader bandwidth and temporal duration than the 1 GHz VECSEL. The pulse train was 1.6 times transform limited compared to the 1 GHz VECSEL which was 1.29 times the transform limit; meaning that the 6 GHz pulse train was more strongly chirped than the 1 GHz laser before amplification. The pulse train had an average power of 20 mW measured after the isolator and the laser threshold was 680 mW.

The 6 GHz seed had an asymmetric spectrum, again with the trailing edge towards longer wavelengths. The seed spectrum can be seen in figure 5.7 a); it was centred at 1042.88 nm and had a bandwidth of 3.39 nm. The modulations present in the 1 GHz spectral data have been removed by angle polishing the 6 GHz gain chip; this has also reduced the size of the side peaks seen in the autocorrelation. The seed pulse had a duration of 540 fs assuming a sech squared fit to the autocorrelation in figure 5.7 b).

After amplification, the bandwidth of the pulse had decreased by 0.32 nm and shifted towards shorter wavelengths. The amplified spectrum, figure 5.7 c), has a FWHM bandwidth of 3.07 nm centred at 1042.63 nm. The shape of the pulse spectrum has been changed slightly by amplification, becoming more symmetrical with the longer wavelength edge becoming steeper. The average power of the pulse train was increased to 1.58 W, this figure includes some ASE, estimated from figure 5.7 e) to be

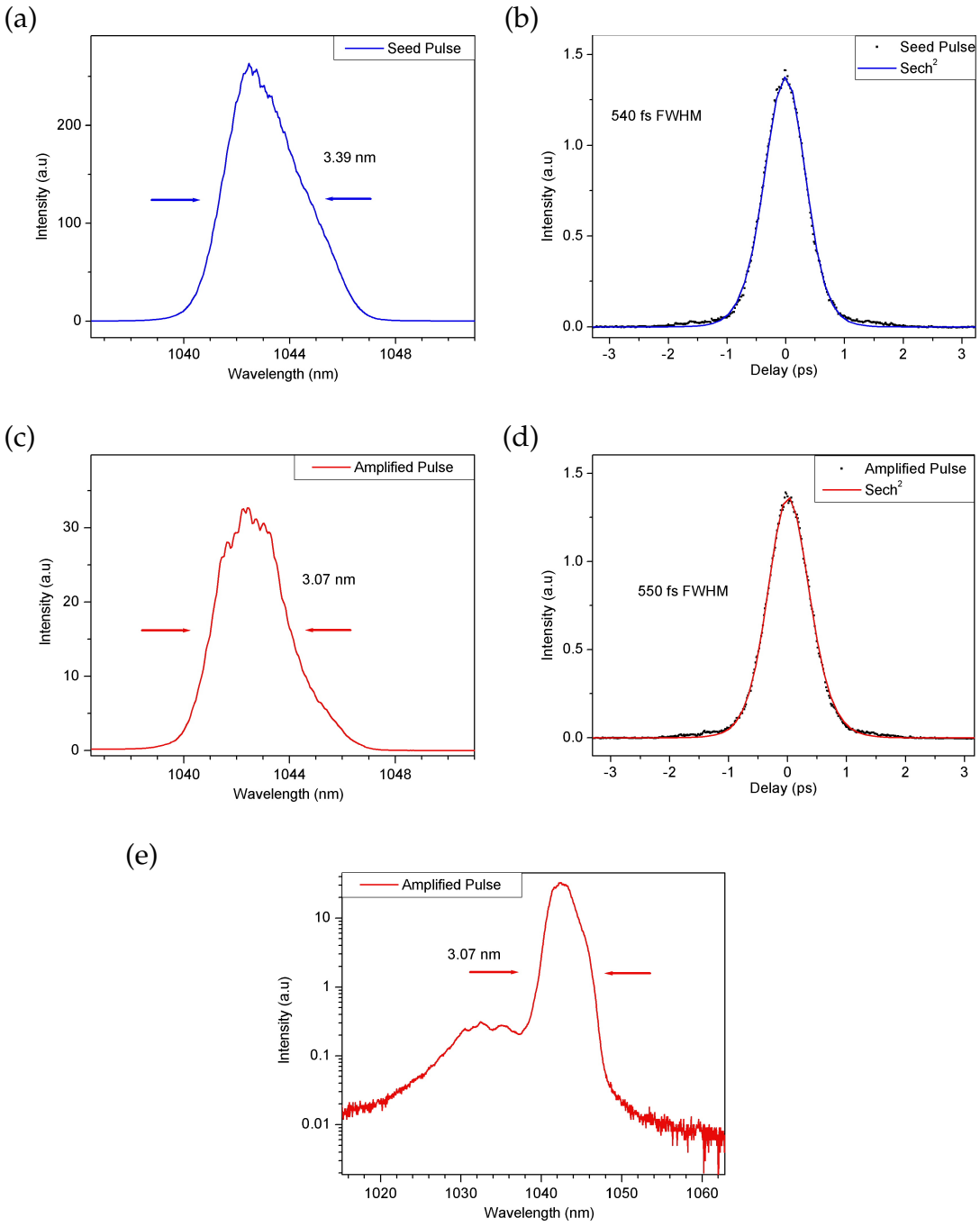

Figure 5.7: Amplifier results with a 6 GHz VECSEL seed: (a) seed spectrum; (b) autocorrelation of VECSEL seed including a sech^2 fit; (c) amplified spectrum; (d) autocorrelation of amplified pulse train; (e) log plot of amplified spectrum showing residual ASE. The modulations present in both the amplified and seed spectra are due to substrate reflections within the VECSEL.

less than 5 % of the total power measured after amplification. The pulse duration has increased after amplification to 550 fs; the amplified pulse train was thus 1.47 times transform limited.

Summarising these results, the 6 GHz pulse train has been amplified by 18.8 dB while maintaining the temporal shape of the pulse train. The amplified pulse energy was 250 pJ and the peak power was 460 W. The change in spectral shape is a small effect, probably caused by the non-uniform gain experienced across the bandwidth of the pulse. The nonlinear effect of SPM can cause spectral narrowing, when the seed pulse initially has a negative frequency chirp [18]. However the effect depends strongly upon peak power and would be stronger for the 1GHz laser, which experienced less spectral narrowing than the 6 GHz pulse train. An estimate for the GVD experienced by the pulse in the fibre can again be made by using equations 5.4 and 5.5, by doing this, two possible values of $16.09 \times 10^{-3}\ ps^2/m$ or $47.45 \times 10^{-3}\ ps^2/m$ are obtained for β_2.

5.6 Conclusions

A single stage Yb-doped fibre amplifier has been constructed, enabling the amplification of VECSEL pulses in a regime of low linear dispersion with negligible nonlinear effects. Up to 19 dB of gain has been achieved at 1 GHz and 18.8 dB at 6 GHz, the slight difference arising because of a slightly lower coupling efficiency of the 6 GHz seed into the fibre core. At high repetition rates the gain of the fibre depends upon the average power of the VECSEL seed, so this technique should be scalable to much higher repetition rates.

The amplified pulse train maintained its shape in the time domain, increasing slightly in length; this is an indication that the only dispersive effect of significance was the linear dispersion of the fibre, which was minimised by the short length of fibre being used. In the frequency domain the pulse bandwidth was narrowed slightly, this effect is primarily caused by the gain of the fibre.

The modelling software provided by Liekki shows that the output power of the 2.2 m long amplifier presented in this work could be increased in three ways. The first way is to increase the average power of the seed light coupled into the fibre; figure 5.4 shows that around 1.9 W output power should be achievable with 20 mW coupled

into the fibre. In practice this would require designing a VECSEL that operates with an increased average power of around 100 mW. This is the least practical approach to a higher power amplifier. The amplified signal can also be increased by introducing more pump power into the fibre; to do this a fibreised pump combiner could be used to pump with up to 40 W. In addition to pumping harder a longer length of fibre could also be used, this will increase the length of the amplified pulse in the time domain by introducing extra material dispersion; eventually the length of the fibre will become great enough that nonlinear effects will become significant.

The optimum length of fibre would be one where linear dispersion has only a minimum effect upon the pulse length and the nonlinear effects can still be ignored. When estimating this optimum fibre length it is useful to characterise the linear and nonlinear effects by assigning them dispersion lengths L_D and L_{NL} as done in section 4.4. The effect of material dispersion is characterised by the length L_D, the duration of a Gaussian pulse will be increased by a factor of $\sqrt{2}$ when the fibre length is made equal to the dispersion length L_D. Using a 500 fs input pulse L_D will be equal to 10 m. Using an input power of 1.5 W and a 500 fs pulse with a 6 GHz repetition rate will experience nonlinear effects within the fibre with characteristic length L_{NL} = 3.7 m; if the input power is increased to 5 W then L_{NL} = 1.1 m. This analysis is simplistic but leads to the prediction that this technique could be scaled to powers of around 5 W.

5.7 References

[1] C. B. Schaffer, A. Brodeur, J. F. Garcia, and E. Mazur. "Micromachining bulk glass by use of femtosecond laser pulses with nanojoule energy". *Optics Letters*, 26(2):93–5, 2001.

[2] S. Lecomte, R. Paschotta, M. Golling, D. Ebling, and U. Keller. "Synchronously pumped optical parametric oscillators in the 1.5-mu;m spectral region with a repetition rate of 10 GHz". *Journal of the Optical Society of America B (Optical Physics)*, 21(4):844–50, 2004.

[3] D. A. B. Miller. "Optics for low-energy communication inside digital processors: quantum detectors, sources, and modulators as efficient impedance converters". *Optics Letters*, 14(2):146–8, 1989.

[4] V. Gerginov, C. E. Tanner, S. A. Diddams, A. Bartels, and L. Hollberg. "High-resolution spectroscopy with a femtosecond laser frequency comb". *Opt. Lett.*, 30(13):1734–1736, 2005.

[5] A. Bartels, F. Hudert, C. Janke, T. Dekorsy, and K. Kohler. "Femtosecond time-resolved optical pump-probe spectroscopy at kilohertz-scan-rates over nanosecond-time-delays without mechanical delay line", 2006.

[6] L. Krainer, R. Paschotta, S. Lecomte, M. Moser, K. J. Weingarten, and U. Keller. "Compact Nd:YVO4 lasers with pulse repetition rates up to 160 GHz". *IEEE Journal of Quantum Electronics*, 38(10):1331–8, 2002.

[7] S. Lecomte, R. Paschotta, S. Pawlik, B. Schmidt, K. Furusawa, A. Malinowski, D. J. Richardson, and U. Keller. "Synchronously pumped optical parametric oscillator with a repetition rate of 81.8 GHz". *IEEE Photonics Technology Letters*, 17(2):483–5, 2005.

[8] C. G. Leburn, A. A. Lagatsky, C. T. A. Brown, and W. Sibbett. "Femtosecond Cr¡sup¿4+¡/sup¿:YAG laser with 4 GHz pulse repetition rate". *Electronics Letters*, 40(13):805–807, 2004.

[9] T. M. Fortier, A. Bartels, and S. A. Diddams. "Octave-spanning Ti:sapphire laser with a repetition rate gt;1 GHz for optical frequency measurements and comparisons". *Optics Letters*, 31(7):1011–13, 2006.

[10] A. Bartels, D. Heinecke, and S. A. Diddams. "Passively mode-locked 10 GHz femtosecond Ti:sapphire laser". *Optics Letters*, 33(16):1905–7, 2008.

[11] Zhou Shian, D. G. Ouzounov, and F. W. Wise. "Passive harmonic mode-locking of a soliton Yb fiber laser at repetition rates to 1.5 GHz". *Optics Letters*, 31(8):1041–3, 2006.

[12] E. Yoshida and M. Nakazawa. "80 200 GHz erbium doped fibre laser using a rational harmonic mode-locking technique". *Electronics Letters*, 32(15):1370–2, 1996.

[13] Blend Orta, Ammar Hideur, and Marc Brunel. "Passive harmonic mode locking with a high-power ytterbium-doped double-cladfiber laser". *Opt. Lett.*, 29(17):1995–1997, 2004.

[14] S. Arahira, Y. Matsui, and Y. Ogawa. "Mode-locking at very high repetition rates more than terahertz in passively mode-locked distributed-Bragg-reflector laser diodes". *IEEE Journal of Quantum Electronics*, 32(7):1211–24, 1996.

[15] P. Dupriez, C. Finot, A. Malinowski, J. K. Sahu, J. Nilsson, D. J. Richardson, K. G. Wilcox, H. D. Foreman, and A. C. Tropper. "High-power, high repetition rate picosecond and femtosecond sources based on Yb-doped fiber amplification of VECSELs". *Optics Express*, 14(21), 2006.

[16] D. Lorenser, D. J. H. C. Maas, H. J. Unold, A. R. Bellancourt, B. Rudin, E. Gini, Ebling Dirk, and U. Keller. "50-GHz passively mode-locked surface-emitting semiconductor laser with 100-mW average output power". *IEEE Journal of Quantum Electronics*, 42(8):838–47, 2006.

[17] V. I. Kruglov, A. C. Peacock, J. D. Harvey, and J. M. Dudley. "Self-similar propagation of parabolic pulses in normal-dispersion fiber amplifiers". *J. Opt. Soc. Am. B*, 19(3):461–469, 2002.

[18] J. Limpert, T. Gabler, A. Liem, H. Zellmer, and A. Tnnermann. "SPM-induced spectral compression of picosecond pulses in a single-mode Yb-doped fiber amplifier". *Applied Physics B: Lasers and Optics*, 74(2):191–195, 2002.

Chapter 6

Nonlinear Amplification in a VECSEL-YDFA

The work described in this chapter aimed to investigate the possibility of exploiting the nonlinear properties of a fibre amplifier to spectrally broaden a VECSEL pulse train. As has been described in section 4.4, it is possible for a pulse train to evolve towards a parabolic intensity profile with the important property of a linear frequency chirp. The pulse duration can be reduced to below that of the seed pulse by compensating for the linear chirp after amplification. Parabolic amplification of a VECSEL pulse train has previously been demonstrated in a multistage MOPA system [1]; this system achieved an average power of 53 W with a pulse duration, after compression, of 110 fs. The design and testing of a simpler single stage amplifier is described in this chapter. Computer modelling of the fibre gain and nonlinear pulse propagation indicate that a parabolic pulse profile with an average power greater than 3 W should be obtainable.

The evolution of a pulse towards the parabolic regime depends upon the initial pulse energy and pulse duration as well as the fibre: length, gain and nonlinear parameter γ; where $\gamma = n_2\omega_0/cA_{eff}$ and A_{eff} is the effective area of the fibre mode. Only limited control over the fibre gain and nonlinear parameter gamma is possible, this is also the case with the duration of the VECSEL pulses, limited at the time of this experiment to a minimum of around 480 fs. A Liekki fibre with a core size of 6 μm was chosen for the amplifier since the small mode area (A_{eff}) will give enhanced spectral broadening compared to the large core fibre of section 5.

Once the type of fibre was chosen the analytical techniques described in section

4.4 were used to estimate the minimum fibre length and the optimum pulse parameters for fast evolution into the parabolic regime. Computer modelling of the gain and nonlinear pulse propagation were carried out to obtain the optimum pump configuration (with the available sources) and the extent of spectral broadening that could be expected. The computer modelling indicated that a parabolic pulse profile with an average power greater than 3 W should be obtainable. An amplifier was constructed but failed to demonstrate significant gain at the VECSEL wavelength. This is believed to be due to the low power of the pump source and a mismatch between the peak gain wavelength of the fibre and VECSEL seed.

6.1 Designing a Single Stage Parabolic Amplifier

The amplifier design was chosen to be based around a length of Liekki fibre with a 6 μm diameter core. This fibre will have a larger nonlinear parameter γ, increasing the spectral broadening caused by SPM, compared to the larger core fibre used previously in section 5. Once the fibre type was chosen, the analytical expressions described in section 4.4 were used to estimate the optimum pulse energy and pulse length required to reach the parabolic regime; the system is considered optimised when the available pulse length (energy) is chosen to minimize the length of fibre z_c required to reach the parabolic regime.

To achieve the fastest convergence towards the parabolic regime, using a 20 mW seed with a 1 GHz repetition rate, the optimum initial pulse duration is given by equation 4.44 (repeated below)

$$T_0 = \frac{6\sqrt{\gamma\beta_2/2A_0}}{g}, \tag{6.1}$$

where T_0 is 14 fs. This time is clearly unobtainable with a VECSEL; the rate of convergence towards the parabolic regime can instead be increased by optimising the pulse energy of the VECSEL. Assuming a pulse duration of 500 fs, the optimum pulse energy of the seed is given by equation 4.46 (repeated below)

$$U_{in}^{opt} = \frac{2T_0^3 g^2}{27\gamma\beta_2}, \tag{6.2}$$

where U_{in}^{opt} will be 93 pJ, which corresponds to an average power of 93 mW at 1 GHz. The available gain sample used in this work is over four years old and gives a maxi-

mum output of around 20 mW; however when newly grown the sample would operate near 100 mW [2].

The following parameters were used in the optimisation equations: $g = 1.23\ m^{-1}$, $\gamma = 0.006\ W^{-1}m^{-1}$, $B_2 = 0.025\ ps^2/m$, $U_{in} = 20$ pJ and $A_0 = 9.54$. In the literature γ has a number of measured values in the range 2 - 3.5×10^{-20} [3], a value of $n_2 = 2.2\times10^{-20}$ is used throughout this chapter. The value of linear gain was obtained by modelling the output power of a VECSEL pulse train after amplification in 15 m of Liekki fibre; the model will be described later where it is used to obtain a more realistic gain profile, necessary for modelling the nonlinear propagation of a pulse.

The minimum length of fibre required to reach the parabolic regime can be calculated using equation 4.47

$$z_c(N) = \frac{3}{2g} ln\left(\frac{Ng}{6\left|\gamma\right| A_0^2}\right); \tag{6.3}$$

with the pulse parameters obtainable and a value of $N = 100$, z_c has a value of 4.42 m. It was concluded from this analytical treatment that the amplifier needs to be greater than 4.42 m in length; however, the amplifier length could be reduced by increasing the average power of the 1 GHz VECSEL to 93 mW. These calculations assume a linear gain along the fibre of 1.23 m^{-1} achieved using 15 m of Liekki fibre pumped with 10 W at 920 nm. Once the pulse train reaches the parabolic regime, the parabolic profile and linear chirp will be maintained along the remaining length of the amplifier; it is thus desirable to make the amplifier longer than z_c since this will increase the output power and spectral broadening of the pulse train. The optimum length of the fibre, for obtaining the shortest pulse after compression with the highest average power, depends upon how the amplifier is pumped. The inversion at each point along the fibre determines the gain at that location; for example if the fibre were single clad with pump light propagating colinearly with the signal within the fibre core, the inversion will result in reabsorption of shorter wavelengths as the fibre length is increased pushing the fibre gain towards longer wavelengths. In a double clad fibre the pump light is not absorbed so strongly by the fibre core and the inversion becomes a more complicated function of fibre length. In order to decide upon the best pump configuration for the amplifier, the gain of a 15 m length of fibre was modelled assuming a 20 mW VECSEL seed, the results of this modelling are presented in section 6.1.1.

6.1.1 Fibre Gain Modelling

In order to effectively model the nonlinear propagation of the pulse along the fibre length a more realistic gain profile is required. To model the gain of Ytterbium doped fibre, software developed here in Southampton by Fei He et al. was used [4]; this software is commercially available from VPI systems. The model has been adapted from existing telecoms software used for modelling erbium doped fibre amplifiers. The model approximates the lateral inversion along the fibre to a flat top profile, replacing the true radial dependence with overlap integrals for the signal and pump. The model uses equations 4.8 - 4.10 and 4.5 to obtain the inversion fraction along the fibre. Steady state solutions are imposed by setting $\partial N_2(\lambda, t, z)/\partial t = 0$ and using the conservation condition $N_2 + N_1 = 1$ to solve for the inversion fraction at a given location. The propagation equations 4.8 - 4.10 are then integrated along the amplifier to obtain the inversion fraction at each point within the fibre. The software can model both single frequency and broadband sources where light is treated as a number of optical beams of frequency $\Delta\nu_k$ centered at $\lambda_k = c/\nu_k$.

Using the gain modelling software three different end pumping configurations were investigated, in each case a 20 mW, 500 fs pulse centred at 1040 nm was used as the seed. The first configuration involved pumping the double-clad fibre with a 920 nm pump source, such that the pump propagated along the fibre in the same direction as the signal light (forward pumping). A wavelength of 920 nm was chosen since we had two 5 W pump diodes available at this wavelength and it coincides with one of the ytterbium absorption peaks in figure 4.2. The results of this modelling can be seen in figure 6.1, where the model was run for nine different pump powers ranging from 1 - 25 W. In figure 6.1 a) the total gain of the fibre (dB) has been plotted for each of the nine pump powers showing an initial steep change in gain with increasing pump power; at around 5 W the curve shallows but the gain continues to increase with pump power even after 25 W.

The model calculates the inversion within the fibre as a function of length which can be seen in figure 6.1 b); the 9 pump powers used in the model are also indicated in this figure. The modelling shows that the inversion continues to increase with pump power all the way up to 25 W of pumplight, the greatest inversion occurring within the first two meters of the fibre at every pump power. After about 6 m the curve flattens out indicating that most of the fibre gain will occur before this point.

The final feature in the inversion plot is a negative gradient for lower pump powers after about 12 m, this feature will cause some reabsorption of the signal near the end of the fibre.

The last figure 6.1 c), shows the signal power and residual pump power (dBm) at different points along the fibre. In this figure the bottom curve corresponds to the lowest pump power (1 W) and the top curve is calculated for the highest pump power of 25 W. The lowest four output powers (pump less that 5 W) all show signs of reabsorption within the last 3 m of the fibre. The 6th curve from the bottom, highlighted by an arrow, corresponds to a pump power of 10 W; as will be explained, this pump power was chosen as the most practical for the amplifier.

The second pump configuration was to forward pump the fibre with a 975 nm source, at this wavelength the Yb^{3+} absorption is strongest, suggesting that the amplifier will give more gain than when pumped at 920 nm. Results of modelling with a 975 pump can be seen in figure 6.2, the three graphs show the same trends as in figure 6.1. Pumping at 975 nm does indeed give higher gain and slightly greater output power than pumping with a 920 nm source; for 10 W of pump power the 975 nm source will give 23 dB of gain (3990 mW output power) compared to 22 dB (3160 mW) when pumped with a 920 nm source. A slight disadvantage of using a 975 nm source is that the Yb^{3+} absorption feature is spectrally narrow at this wavelength, necessitating the stabilisation of the pump wavelength; this is not the case with 920 nm source.

The final pump configuration to be investigated was to backward pump the fibre with a 920 nm source so that the seed propagated in the opposite direction to the pump light. These results show the correct trends expected for the pump configuration, but it should be noted that the results presented in figure 6.3 are not as accurate as those of figures 6.1 and 6.2. When modelling a backward pumped amplifier as the signal increases along the fibre so will the pump intensity making the inversion calculation more involved, a longer time or more powerful computer is required to reach the same level of accuracy as was achieved with a forward pumped amplifier.

The most significant feature of the end pumping scheme can be seen in figure 6.3 c) where at all pump powers the signal initially experiences negative gain. Even with a pump power of 25 W the seed has to travel over three metres of fibre before increasing in intensity.

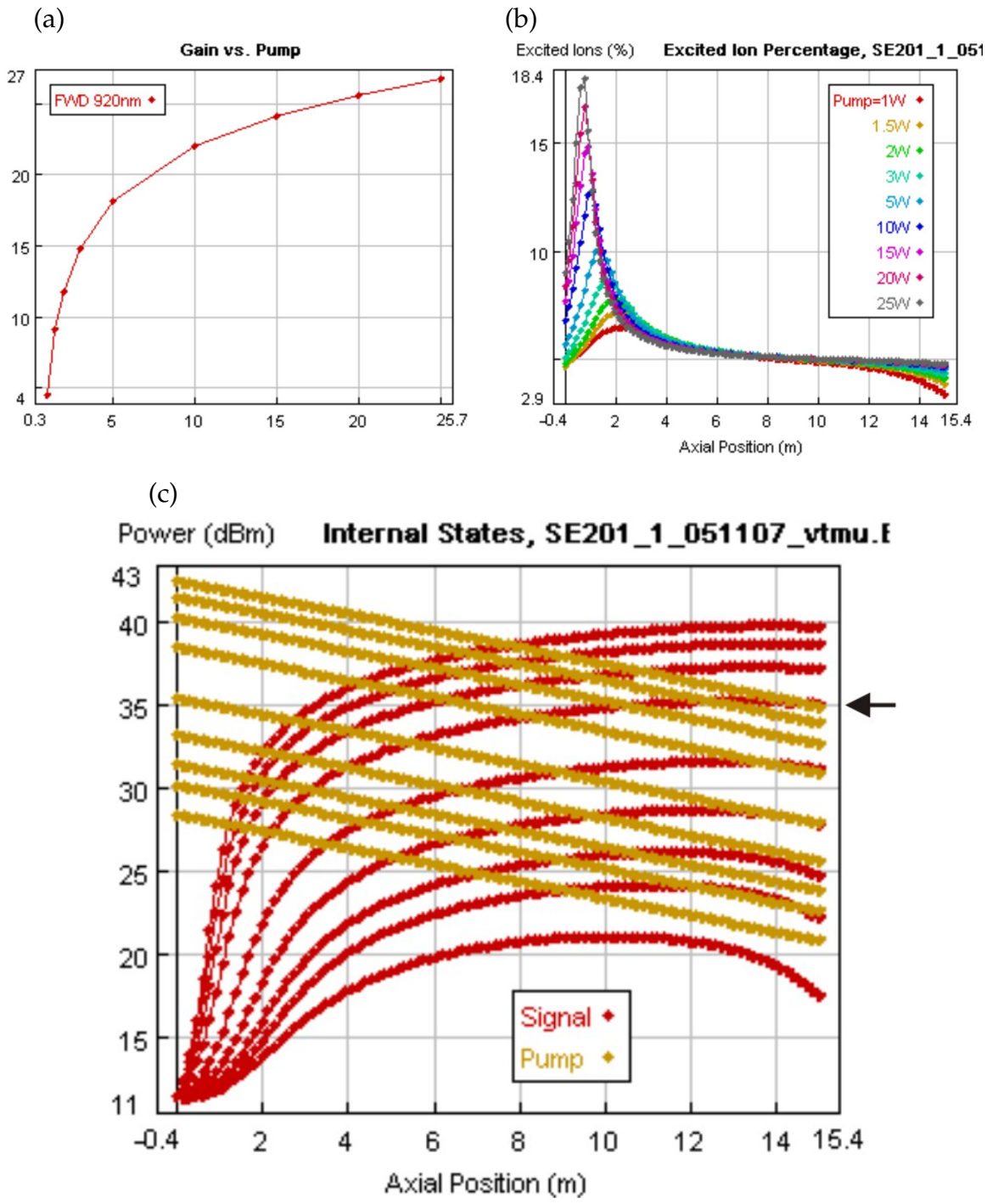

Figure 6.1: Modelling results for Liekki fibre with a 20 mW seed propagating in the same direction as a 920 nm pump: (a) gain in dBm for various incident pump powers, (b) fibre inversion percentage, (c) amplified signal strength (1040 nm) and residual pump vs fibre length; arrow indicates 10 W pump result. The data indicates that the peak gain occurs within the first 2 m of the fibre and that for pump powers that are < 5 W some reabsorption of the signal takes place in the final 3 m of the fibre.

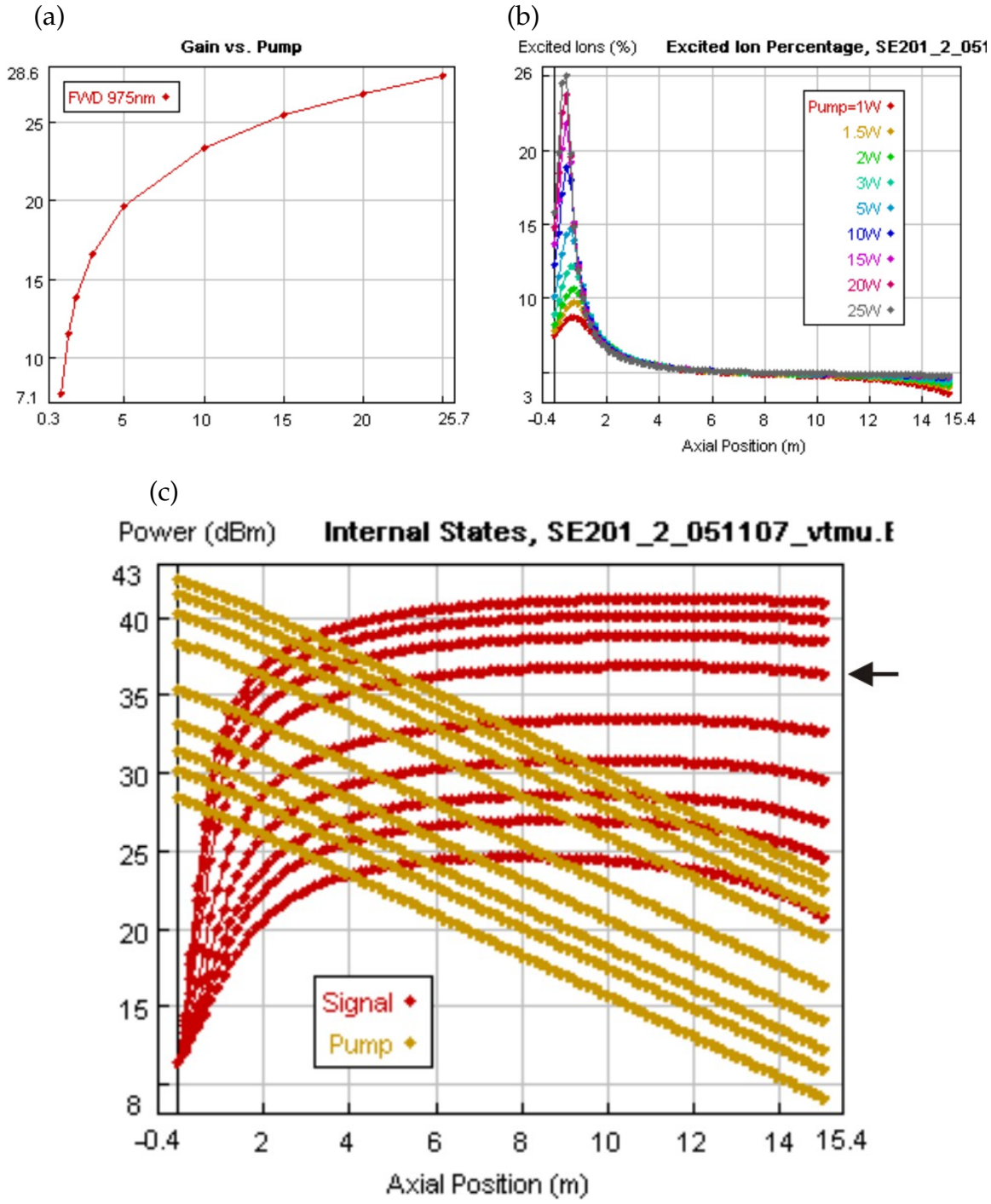

Figure 6.2: Modelling results for a 20 mW seed propagating in the same direction as a 975 nm pump: (a) gain in dBm for various incident pump powers, (b) fibre inversion percentage, (c) amplified signal strength (1040 nm) and residual pump as a function of fibre length; result with 10 W pump is indicated by an arrow. Data shows a higher total gain and that the peak signal power is reached after a shorter length of fibre than when pumped by a 920 nm source. Some reabsorption still occurs in the last 3 m of fibre when pumped below 5 W.

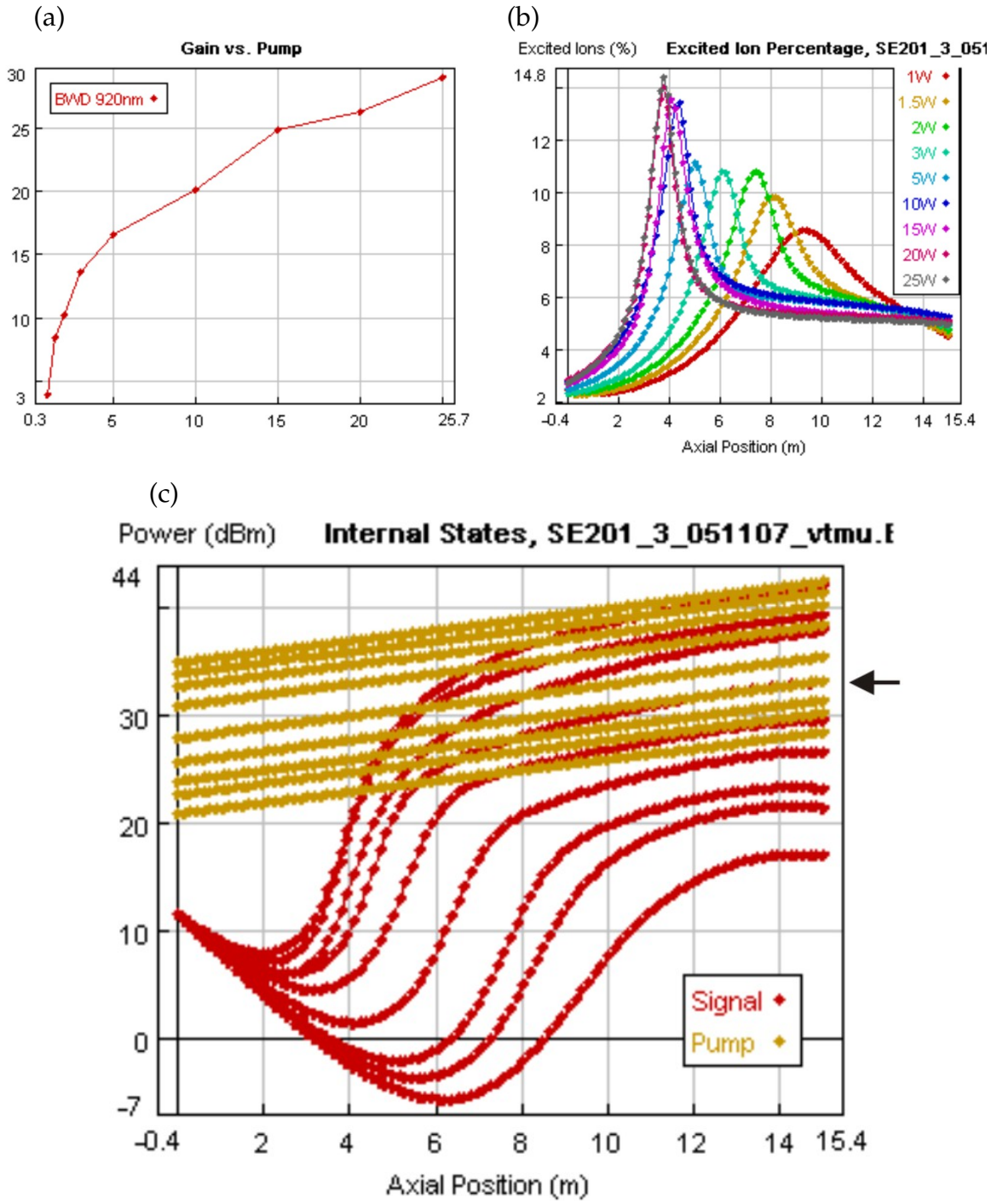

Figure 6.3: Modelling results for Liekki fibre with a 20 mW seed propagating counter to a 920 nm pump: (a) gain in dBm for various incident pump powers, (b) fibre inversion percentage, (c) amplified signal strength (1040 nm) and residual pump as a function of fibre length with arrow indicating 10 W pumping. The accuracy of this modelling is reduced due to the increased complexity of modelling a counter propagating pump. The location of peak inversion and gain within the fibre is more dependent upon pump power with this scheme. The signal experiences initial loss, taking longer to reach maximum power than in the equivalent forward pumping schemes, making this pump configuration less useful for parabolic amplification.

Such a pumping scheme would result in a slower evolution towards the parabolic regime and less spectral broadening than the forward pumping equivalents, for this reason a forward pumping scheme was chosen for the parabolic amplifier. It was decided to pump the amplifier with a 10 W, 920 nm source because of the availability of pump diodes at this wavelength. The modelling shows that slightly more output power could be achieved with a 975 nm pump source, however the power obtained by pumping with 10 W at 920 nm should be sufficient for reaching the parabolic regime.

The linear gain model has been used to show the signal intensity and location of peak gain within a 15 m length of ytterbium fibre under different pump conditions, from this information it is also possible to extract an analytical expression for gain as a function of fibre length. To obtain an expression of gain as a function of fibre length for the chosen pump configuration a 5th order polynomial fit is applied to the 6th curve in figure 6.1; this gives an expression for the signal power vs length of the form

$$P_{sig}(L) = a + bL - cL^2 + dL^3 - eL^4 + fL^5. \tag{6.4}$$

Here L is the propagation length of the signal, P_{sig} is measured in dBm and the lower case letters a - f are all constants. The gain expression is obtained by noting that the incremental gain between two points in the fibre should relate to the change in power between the two points,

$$g(L) = \left[bL - cL^2 ...\right] - \left[b\left(L - dZ\right) - c\left(L - dZ\right)^2 ...\right]. \tag{6.5}$$

This gain equation will be used in the next section where the nonlinear Schrödinger equation is solved, enabling the nonlinear propagation of a pulse within the amplifier to be modelled.The gain $g(L)$ is measured in dB while dZ is the incremental length (step size) used by the nonlinear propagation model below.

6.1.2 Solving the Nonlinear Schrödinger Equation

For modelling the nonlinear propagation of a pulse it is necessary to solve the nonlinear Schrödinger equation with gain, equation 4.34, numerically. An algorithm written by R. Paschotta [5] was used to calculate the temporal and spectral profile of a 1 GHz VECSEL pulse train after propagating through 15 m of Yb-doped fibre with either a linear gain profile figure 6.4 a) or a gain profile of the form given by equation 6.5;

in both cases a 500 fs 20 mW seed was assumed and a 10 W, 920 nm pump giving a total gain of 21.99 dB. The algorithm uses a standard split step Fourier technique as has been used in other work relating to parabolic amplification of pulses [6]. The principal behind the split step Fourier technique is to split the nonlinear Schrodinger equation into two segments

$$\frac{\partial A}{\partial z} = (\hat{D} + \hat{N})A, \tag{6.6}$$

where $\hat{N}$ is a nonlinear operator and $\hat{D}$ is a linear differential operator accounting for dispersion and gain in a linear medium. To model pulse propagation along a length of fibre, the fibre is divided into a number of segments of length h. For each segment the operators $\hat{D}$ and $\hat{N}$ will be applied in turn, acting independently upon the pulse. After each segment a new pulse $A(z+h, T)$ is obtained that is the result of both the nonlinear and dispersive effects of the fibre. The advantage of this technique is that the dispersive effects can be treated in the frequency domain and then Fourier transformed back into the time domain, making the calculation faster. The overall accuracy of the calculation increases if the size of the step h is made smaller.

Results of the nonlinear pulse propagation are shown in figure 6.4 for each of the longitudinal gain profiles. The pulse profile is presented, after amplification, in both the time and the frequency domain showing both the degree of spectral broadening and the resultant pulse duration. A linear gain of 1.23 m^{-1} has been assumed in figure 6.4 a) while a length dependent gain g(L) was used with in figure 6.4 b); g(L) is given by equation 6.5 using the following parameters: a = 10.152, b = 1/864, c = 0.165, d = 0.0067 and e = 9.623×10^{-5}. Both the linear gain and the length dependent gain are chosen so that the average power of the 20 mW seed after amplification is near 35 dBm, matching the output power given in figure 6.1; with both gain profiles the nonlinear model shows a linearly chirped pulse with a parabolic temporal profile.

Amplification with a linear gain will result in less spectral broadening than in the real fibre, since the peak power builds up more slowly along the fibre length; modelling with a linear profile was carried out to provide an estimate of the minimum amount of spectral broadening expected from the amplifier. With the linear gain model results in a parabolic pulse with a FWHM temporal duration of 8.23 ps and a 22.9 nm FWHM bandwidth. Assuming a linear chirp across the entire pulse, compression of the amplified pulse would result in a 70 fs pulse (assuming a Gaussian profile).

(a)

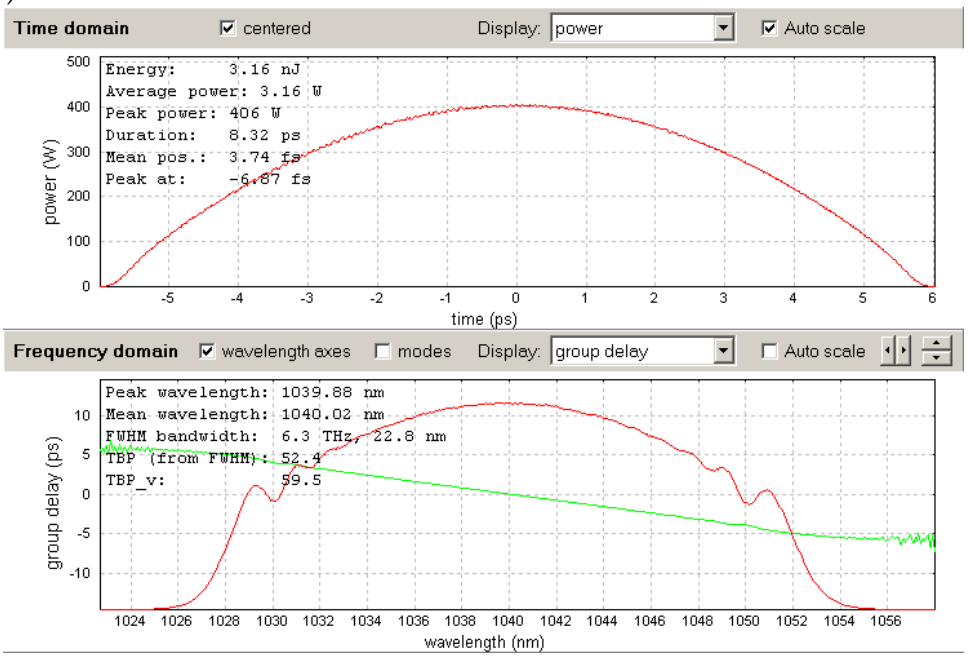

(b)

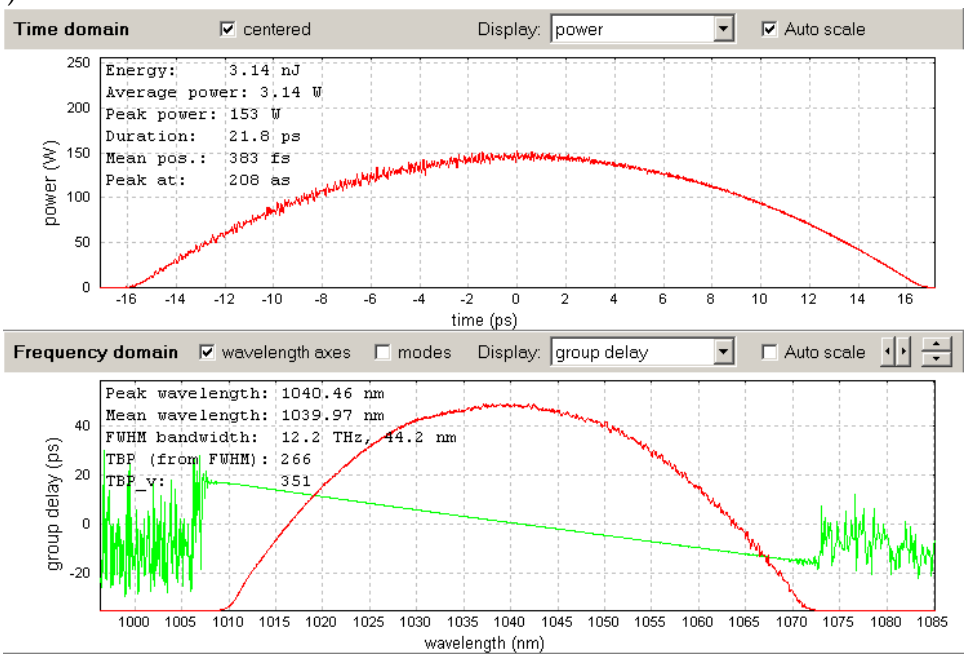

Figure 6.4: Nonlinear propagation in the time and frequency domains of a 500 fs Gaussian seed pulse with repetition rate 1 GHz and average power of 20 mW. (a) Assumes a linear gain, (b) assumes a fit to the modelled output power as a function of length in figure 6.1 (c); with a 10 W 920 nm pump.

In figure 6.4 b) the more realistic gain profile has produced a greater temporal and spectral broadening of the pulse; the resultant pulse has a 21.8 ps duration and a 44.2 nm bandwidth. If this pulse could be compressed with 100 % efficiency then it would be 36 fs in duration.

It should be noted that for ease and speed of modelling the two gain profiles were not wavelength dependent. In a real fibre the bandwidth of the gain is limited. As a pulse propagates within the fibre the finite gain bandwidth will eventually limit the efficiency of compression and the bandwidth of the amplified pulse.

6.2 Amplifier Configuration and Conclusions

An experimental implementation of a VECSEL seeded parabolic amplifier was attempted, with the configuration depicted in figure 6.5. The amplifier employed a

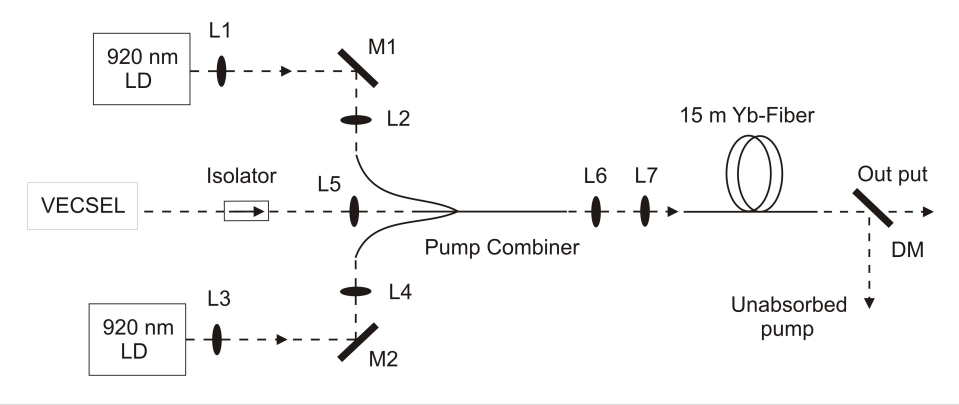

Figure 6.5: Colinear pump set up for the parabolic amplifier: a fiberised pump combiner is used to couple the seed/pump into the core/cladding of a 6 μm core Yb-doped fibre (Liekki1200-6Yb/125DC): DM is a dichroic mirror, L is a lens.

15 m length of Yb-doped fibre (Liekki-Yb1200-6/125DC). The fibre had a 6 μm core and a 125 μm octagonal cladding and was pumped by a 920 nm pump source. To enable the seed to propagate in the same direction as the pump along the amplifier a fibre pump combiner was used. The combiner takes the signals from six large core fibres (125 μm) and one small core fibre (6 μm) and combines them into a single undoped double clad fibre with a core of 6 μm and cladding of 125 μm; the light from the VECSEL propagates in the undoped core. The combiner was used to combine the power from two pump diodes with the signal from a VECSEL; a further four pump

diodes could be combined if more pump power were needed.

The output from the pump combiner was free space launched into one end of the Yb-doped fibre, providing an incident pump power of 10 W. An optical isolator is used to prevent light from the amplifier feeding back in to the VECSEL, while a dichroic mirror was used at the output end to separate the residual pump light from the amplified signal. The fibre was angle cleaved at both ends to increase the laser threshold of the fibre. The seed laser had the same specifications as the 1 GHz VECSEL used for the previous fibre amplifier experiment, described in section 5. The VECSEL incorporated the same angle polished gain chip and SESAM as was used in the 6 GHz amplified result and emitted a train of 500 fs pulses with average power of 20 mW and centre wavelength of 1045 nm.

When the seed was introduced into the fibre it was found that the fibre would not amplify significantly at the seed wavelength. In figure 6.6 three spectra of the output from the end of the fibre are displayed corresponding to three different pump powers. Figure 6.6 shows a laser peak near 1084 nm indicating that without an incident seed pulse (near 1045 nm) the inversion within the fibre produces peak gain around 1084 nm. The peak at 1084 nm was observed even when both ends of the fibre had been angle cleaved, increasing the threshold for lasing. When the 20 mW seed was introduced into the fibre a small peak at the seed wavelength could be observed in the spectrum (not seen in figure 6.6 due to spectrometer cut off), however most of the energy remained within the laser peak at 1084 nm.

The linear modelling of the fibre gain presented earlier in this chapter, showed that with a 20 mW incident seed the fibre should exhibit gain near 1040 nm, this was assuming a 50 % coupling efficiency into the fibre core. Experimentally, even with an incident seed power of 20 mW coupled into the amplifier, the inversion within the fibre produced gain close to 1084 nm, thus preventing the amplification of the VECSEL seed. The VECSEL seed was temperature tuned over the range 1037 - 1049 nm and the fibre ends were angle cleaved a number of times, but the amplifier output was always dominated by lasing near 1084 nm. This suggests that an insufficient amount of seed power was coupled into the fibre core.

In conclusion, the gain of a 15 m length of Liekki(Yb1200_6_125DC) has been modelled along with the nonlinear propagation of a 20 mW VECSEL seed pulse within the fibre. The modelling shows that when pumped with 10 W at 920 nm, the fibre

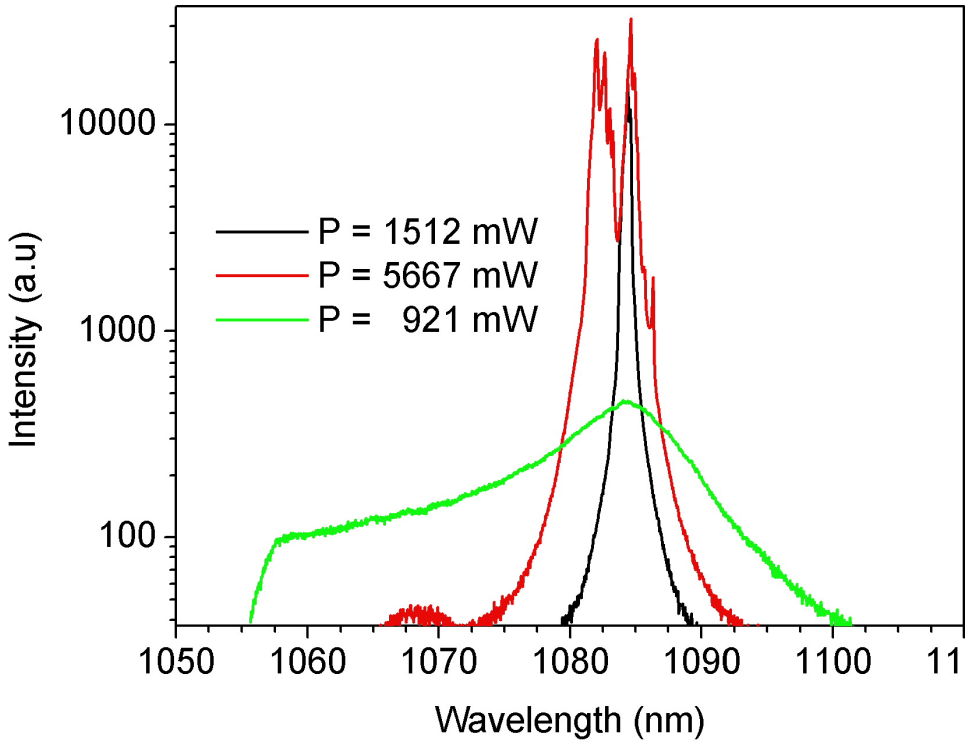

Figure 6.6: Spectra taken from the output end of the amplifier configuration of figure 6.5. The spectra were recorded with three different pump powers as indicated in the figure; in each case there was a 20 mW seed incident upon the amplifier. Lasing close to 1084 nm dominates the fibre output despite the pressence of seed pulses near 1040 nm.

amplified VECSEL pulse train should exhibit a parabolic temporal profile with a linear frequency chirp and average power of over 3 W. The amplified spectrum should be sufficiently broadened to enable compression of the pulse train to below 100 fs FWHM duration. Experimentally, insufficient signal light was coupled into the fibre to produce the predicted gain and nonlinear evolution at the signal wavelength. An improved design upon this amplifier would include a seed source with a greater average power; once enough power near 1040 nm is coupled into the amplifier core, the inversion shown in figure 6.1 will be achieved and the amplifier should behave as predicted in the modelling. Practically the average power of the seed could be increased by using an amplifier such as the one demonstrated in chapter 5 to preamplify the VECSEL seed. Alternatively the VECSEL gain chip could be regrown to give slightly higher average power. The regrowth could probably be achieved with the same design as QT1544 which gave average powers near 100 mW when first

grown [2]. Alternatively a regrowth could involve shifting the gain wavelength towards longer wavelengths, 1060 nm has been demonstrated with the same material system as QT1544 [7]. The longer wavelength seed would be closer to the peak laser gain of the fibre and should therefore experience more gain that a 1040 nm VECSEL.

6.3 References

[1] P. Dupriez, C. Finot, A. Malinowski, J. K. Sahu, J. Nilsson, D. J. Richardson, K. G. Wilcox, H. D. Foreman, and A. C. Tropper. "High-power, high repetition rate picosecond and femtosecond sources based on Yb-doped fiber amplification of VECSELs". *Optics Express*, 14(21), 2006.

[2] A. Garnache, S. Hoogland, A. C. Tropper, I. Sagnes, G. Saint-Girons, and J. S. Roberts. "Sub-500-fs soliton-like pulse in a passively mode-locked broadband surface-emitting laser with 100 mW average power". *Applied Physics Letters*, 80(21):3892–3894, 2002.

[3] P. Agrawal, G. *Nonlinear Fiber Optics*. Academic Press, 2001.

[4] F. He, J. H. Price, K. T. Vu, A. Malinowski, J. K. Sahu, and D. J. Richardson. "Optimisation of cascaded Yb fiber amplifier chains using numerical-modelling". *Opt. Express*, 14(26):12846–12858, 2006.

[5] R. Paschotta. *www.rp-photonics.com*.

[6] V. I. Kruglov, A. C. Peacock, J. D. Harvey, and J. M. Dudley. "Self-similar propagation of parabolic pulses in normal-dispersion fiber amplifiers". *J. Opt. Soc. Am. B*, 19(3):461–469, 2002.

[7] K. S. Kim, J. R. Yoo, S. H. Cho, S. M. Lee, S. J. Lim, J. Y. Kim, J. H. Lee, T. Kim, and Y. J. Park. "1060 nm vertical-external-cavity surface-emitting lasers with an optical-to-optical efficiency of 44 percent at room temperature". *Applied Physics Letters*, 88(9):91107–1, 2006.

Chapter 7

Conclusions

The passively mode-locked VECSEL is a compact and robust source of ultra-short pulses, naturally suited for applications requiring gigahertz repetition rates. Where repetition rate is less important, applications exploiting the properties of ultra-short pulses require the optimization of one or more of the pulse properties: pulse length, pulse energy or peak power. The maximum pulse energy and thus the peak power obtained directly from a VECSEL is constrained by the need to operate the oscillator at gigahertz repetition rates and is unlikely to exceed the peak powers obtainable with fibre lasers and solid state lasers. The pulse energy of a VECSEL can be increased through power scaling and designing the gain chip for high power operation. However, the design features necessary for achieving high average powers, such as a resonant micro-cavity within the gain chip, reduce the bandwidth available for mode-locking, reducing the obtainable peak power by increasing the pulse length of the laser.

The research presented in this thesis has aimed to investigate techniques for increasing the peak power of the VECSEL pulse train without redesigning the VECSEL gain chip for high power operation. The techniques presented in this thesis have demonstrated that peak powers far exceeding those currently reported for passively mode-locked VECSELs can be achieved by integrating the VECSEL with existing fibre technology. This work has strongly focused upon the amplification of VECSEL pulses within Yb-doped fibre and as such is mostly applicable to VECSEL sources that fall within the gain bandwidth of ytterbium.

Fibre amplification of a passively mode-locked VECSEL has previously been demonstrated at a repetition rate near 1 GHz, where a multistage, master oscillator power

amplifier (MOPA) was used to achieve average powers in excess of 200 W [1]. The research presented in this thesis has focused upon extending the work of Dupriez et al. [1] towards higher repetition rates and shorter pulses. Single stage ytterbium doped fibre amplifiers (YDFAs) were chosen for this work because of their simplicity. The VECSEL-YDFAs presented in this work thus offer watt level average power at gigahertz repetition rates, suitable for applications such as coherent terahertz generation and detection [2] and optical sampling [3].

The properties of optical fibre can be tailored to manipulate the spectral and temporal profile of an ultra-short pulse propagating within the fibre. In the time domain the dispersive properties of the fibre will cause a transform limited pulse to stretch, introducing a chirp. This dispersive effect can alternatively be used to compress an initially chirped pulse in time, increasing the peak power of the pulse. Pulse compression within a fibre, or by alternative means is only practical when the initial pulse is linearly chirped, although compression of cubically chirped pulses has been demonstrated [4].

7.0.1 Frequency Resolved Optical Gating

It was observed that the VECSELs used in this thesis, capable of producing 500 fs transform limited pulses, would also produce chirped pulses which could be greater than 1.5 times transform limited and still be close to 500 fs in duration. The phase structure of these chirped pulses has been investigated, for the first time to my knowledge, using the technique of frequency resolved optical gating (FROG). A single VECSEL gain chip has been mode-locked at two different repetition rates using the same SESAM. Spectrograms were recorded of the VECSEL pulse train at repetition rates of 1 GHz and 6 GHz, from which the phase information of the pulses was retrieved using an algorithm written for second harmonic FROG. These measurements have shown that the sub-picosecond chirped pulses generated by a Stark-mode-locked VECSEL have non-linear phase structure, with significant contributions from third order (TOD) and second order dispersion (GDD).

Values for the GDD and TOD experienced by the pulse train have been extracted from the spectrograms of both the 1 GHz and 6 GHz VECSELs. Since the 1 GHz VECSEL operated in a multiple pulsing regime, producing pairs of equally spaced pulses, it was decided to compare the measured phase structure of this source with

that of a fundamentally mode-locked 6 GHz VECSEL. The two lasers contained the same gain chip and SESAM and both gave average powers close to 15 mW; the 6 GHz laser had approximately a third of the pulse energy and pulse peak power of the 1 GHz VECSEL. Plots of the group delay dispersion for each laser show qualitatively the same behavior, with an apparent reversal in the sign of dispersion between the two lasers; the 6 GHz VECSEL appears to have a negative frequency chirp. However, because of the ambiguities present in SHG-FROG it is impossible to know the exact sign of the dispersion from these measurements alone. It is possible to obtain the sign of the chirp by breaking the symmetry of the measured spectrogram, this can be achieved by inserting a glass slide into the beam path [5]. The partial reflections from a glass slide will appear at a later time, with decreased intensity within the measured spectrogram; this will remove the temporal ambiguity of the FROG trace enabling for the sign of the chirp to be retrieved. This was not attempted with either of the VECSELs since the pulse energy was so low the partial reflections would not have been detected by the FROG setup.

If we assume that the sign of the chirp is the same for both repetition rates, the 6 GHz VECSEL has experienced nearly six times as much GDD and two times as much TOD as the 1 GHz VECSEL. This is surprising since the two lasers operated at slightly different wavelengths, so that the 1 GHz laser experienced more positive GDD and TOD from the etalon and material effects within the cavity. The 1 GHz VECSEL also had three times the pulse energy of the 6 GHz VECSEL, and was expected to be more strongly chirped by intensity dependent effects, such as changing carrier concentration and self phase modulation.

7.0.2 Fibre Amplification

A single stage Yb-doped fibre amplifier has been constructed, enabling the amplification of VECSEL pulses in a regime of low linear dispersion with negligible nonlinear effects. The amplifier has been tested with two different VECSEL seeds; up to 1.9 dB of gain has been achieved at a repetition rate of 1 GHz and 1.88 dB at 6 GHz, the slight difference arising because of a slightly lower coupling efficiency of the 6 GHz seed into the fibre core. This technique should be scalable to higher repetition rates since the gain of the fibre depends upon the average power of the VECSEL seed. In the frequency domain the nonlinear properties of the fibre can be used to alter

the pulse spectrum. The interaction of self phase modulation (SPM) with the linear dispersion of the fibre can be used to spectrally broaden an ultra-short pulse, if the correct fibre/pulse parameters are chosen then the resulting spectrally broadened pulse will have a linear chirp, and can be compressed in time to increase the peak power of the pulse; this effect causes the pulse to have a parabolic temporal profile. Parabolic amplification of a VECSEL pulse train, where fibre gain was also present, has been attempted at 1 GHz using the amplifier configuration described in chapter 6. Experimental realization of a working single-stage parabolic amplifier was not achieved due to a mismatch between the optimum gain wavelength of the fibre with that of the VECSEL. The changes to the amplifier and seed source necessary to achieve parabolic amplification have been described, but were not implemented due to the need to grow a new gain sample and SESAM.

The gain of the amplifier and nonlinear evolution of the pulse train inside the fibre with gain, have been modelled using two different software packages. From this modelling it is predicted that an amplifier could be realized with 35 dBm of gain at a wavelength near 1040 nm. The resulting spectrally broadened pulse train will be linearly chirped, with sufficient bandwidth to be compressed in the time domain to give sub 100 fs pulses. It should be noted that the nonlinear propagation model assumes a flat gain profile in the frequency domain, in reality the gain profile of the fibre will result in a narrower, compressible, spectrum than what has been predicted. At a repetition rate of 1 GHz a 100 fs pulse with an average power of 3.1 W as should be obtainable with parabolic amplification will have a peak pulse power of 29 kW, this should be compared with a peak power of 112 W obtained by the highest reported average power mode-locked VECSEL [6], and 84.6 W obtained with 260 fs pulse reported by this group [7].

7.0.3 Future Work

VECSEL pulses could be amplified to the parabolic regime by incorporating a preamplifier into the amplifier configuration described in chapter 6. This preamplifier should be of the same type as the scheme demonstrated in chapter 5 of this thesis. By doing so, it should be possible to measure the average power required to reach the parabolic regime at wavelengths near 1040 nm. A VECSEL gain chip could then be designed to operate at this average power.

Wavelength conversion using an optical parametric oscillator (OPO) is a widely used technique with solid state lasers, for example to convert the 1064 nm output from a fibre amplified Nd:YVO_4 to a wavelength near 1550 nm, suitable for telecoms applications [8]. The integration of an OPO with the fibre amplified VECSELs described in this thesis would enable sub-picosecond operation at wavelengths where the semiconductor growth technology is not yet mature enough to match the performance of the GaAs based material used in this thesis.

The speed of phase characterisation of the VECSEL output can also be improved. A single spectrogram, such that presented in chapter 3, took several minutes to acquire due to the mechanical translation of the delay line. There are now commercially available systems, such as video FROG, that can record a spectrogram, and retrieve the phase of the pulse in a matter of seconds.

The VECSELs characterised in this thesis were operating in the femtosecond regime, with a stable pulse shape and temporal duration. There are, however, a number of other regimes, where the pulse spectrum and temporal duration evolve slowly over a number of minutes. Using a video FROG it would be interesting to observe the phase evolution of these transitory pulse regimes.

7.1 References

[1] P. Dupriez, C. Finot, A. Malinowski, J. K. Sahu, J. Nilsson, D. J. Richardson, K. G. Wilcox, H. D. Foreman, and A. C. Tropper. "High-power, high repetition rate picosecond and femtosecond sources based on Yb-doped fiber amplification of VECSELs". *Optics Express*, 14(21), 2006.

[2] Z. Mihoubi, K. G. Wilcox, S. Elsmere, A. Quarterman, R. Rungsawang, I. Farrer, H. E. Beere, D. A. Ritchie, A. Tropper, and V. Apostolopoulos. "All-semiconductor room-temperature terahertz time domain spectrometer". *Optics Letters*, 33(18):2125–7, 2008.

[3] A. Bartels, F. Hudert, C. Janke, T. Dekorsy, and K. Kohler. "Femtosecond time-resolved optical pump-probe spectroscopy at kilohertz-scan-rates over nanosecond-time-delays without mechanical delay line", 2006.

[4] Lawrence Shah, Zhenlin Liu, Ingmar Hartl, Gennady Imeshev, Gyu Cho, and Martin Fermann. "High energy femtosecond Yb cubicon fiber amplifier". *Opt. Express*, 13(12):4717–4722, 2005.

[5] E. Zeek, A. P. Shreenath, P. O'Shea, M. Kimmel, and R. Trebino. "Simultaneous automatic calibration and direction-of-time removal in frequency-resolved optical gating". *Applied Physics B: Lasers and Optics*, 74(0):s265–s271, 2002.

[6] A. Aschwanden, D. Lorenser, H. J. Unold, R. Paschotta, E. Gini, and U. Keller. "2.1-W picosecond passively mode-locked external-cavity semiconductorlaser". *Opt. Lett.*, 30(3):272–274, 2005.

[7] K. G. Wilcox, Z. Mihoubi, G. J. Daniell, S. Elsmere, A. Quarterman, I. Farrer, D. A. Ritchie, and A. Tropper. "Ultrafast optical Stark mode-locked semiconductor laser". *Optics Letters*, 33(23):2797–9, 2008.

[8] S. Lecomte, R. Paschotta, S. Pawlik, B. Schmidt, K. Furusawa, A. Malinowski, D. J. Richardson, and U. Keller. "Synchronously pumped optical parametric oscillator with a repetition rate of 81.8 GHz". *IEEE Photonics Technology Letters*, 17(2):483–5, 2005.

Appendix A

Publications

S. P. Elsmere, Z. Mihoubi, A. Quarterman, A. C. Tropper, P. Dupriez, J. Nilsson, and J. S. Roberts. High repetition-rate sub-picosecond source of fibre-amplified vertical-externalcavity surface-emitting semiconductor laser pulses. *CLEO/Europe - IQEC*,page 493, Piscataway, NJ, USA, 2007. IEEE.

S. P. Elsmere, Z. Mihoubi, A. H. Quarterman, P. Dupriez, J. Nilsson, J. S. Roberts, and A. C. Tropper. High-repetition-rate subpicosecond source of fiber-amplified vertical-externalcavity surface-emitting semiconductor laser pulses. *IEEE Photonics Technology Letters*,20(8):6235, 2008.

S. Hoogland, A. Garnache, K. G. Wilcox, Z. Mihoubi, S. Elsmere, A. Quarterman, and A. Tropper. Spectrotemporal gain bandwidth measurement in an InGaAs/GaAsP quantum well vertical-external-cavity surface-emitting semiconductor laser. 2008 Conference on Lasers and Electro-Optics (CLEO), page 2 pp., Piscataway, NJ, USA, 2008. IEEE.

Z. Mihoubi, K. G.Wilcox, S. Elsmere, A. Quarterman, R. Rungsawang, I. Farrer, H. E. Beere, D. A. Ritchie, A. Tropper, and V. Apostolopoulos. All-semiconductor room-temperature terahertz time domain spectrometer. *Optics Letters*, 33(18):21257, 2008.

A. H. Quarterman, K. G.Wilcox, S. P. Elsmere, Z. Mihoubi, and A. C. Tropper. Active stabilisation and timing jitter characterisation of sub-500 fs pulse passively mode-locked VECSEL. *Electronics Letters*, 44(19):11357, 2008.

A. H. Quarterman, K. G. Wilcox, Z. Mihoubi, S. P. Elsmere, and A. C. Tropper. Characterization of pulse timing jitter of actively stabilised 1-GHz vertical-external-cavity surfaceemitting semiconductor laser producing 500-fs pulses. *Conference on Lasers and Electro-Optics (CLEO)*, page 2 pp., Piscataway, NJ, USA, 2008. IEEE.

K. G. Wilcox, Z. Mihoubi, G. J. Daniell, S. Elsmere, A. Quarterman, I. Farrer, D. A. Ritchie, and A. Tropper. Ultrafast optical Stark mode-locked semiconductor laser. *Optics Letters*, 33(23):27979, 2008.

K. G.Wilcox, Z. Mihoubi, S. Elsmere, A. Quarterman, H. D. Foreman, S. Hashimoto, T. Sudmeyer, U. Keller, and A. Tropper. Passively modelocked 832 nm vertical-external-cavity surface-emitting semiconductor laser producing 15.3 ps pulses at 1.9 GHz repetition rate. *Electronics Letters*, 44(25):14691470, 2008.

K. G. Wilcox, Z. Mihoubi, S. P. Elsmere, A. H. Quarterman, H. D. Foreman, and A. Tropper. Passively mode-locked 832- nm vertical-external-cavity surface-emitting semiconductor laser producing 15.3-ps pulses at 1.9-GHz repetition rate. *Conference on Lasers and Electro-Optics (CLEO)*, page 2 pp., Piscataway, NJ, USA, 2008. IEEE.